New Developments in Inherent Strain Method for Predicting and Mitigating Residual Stress and Distortion in Metal Additive Manufacturing

by

Wen Dong

B.S., Huazhong University of Science and Technology, 2015

M.S., Huazhong University of Science and Technology, 2018

Submitted to the Graduate Faculty of the

Swanson School of Engineering in partial fulfillment

of the requirements for the degree of

Doctor of Philosophy

University of Pittsburgh

2024

UNIVERSITY OF PITTSBURGH

SWANSON SCHOOL OF ENGINEERING

This dissertation was presented

by

Wen Dong

It was defended on

January 16, 2024

and approved by

Qihan Liu, Ph.D., Assistant Professor, Department of Mechanical Engineering and Materials Science

Xiayun Zhao, Ph.D., Assistant Professor, Department of Mechanical Engineering and Materials Science

Kevin P. Chen, Ph.D., Paul E. Lego Professor, Department of Electrical and Computer Engineering

Dissertation Director: Albert C. To, Ph.D., William Kepler Whiteford Professor, Department of Mechanical Engineering and Materials Science

New Developments in Inherent Strain Method for Predicting and Mitigating Residual Stress and Distortion in Metal Additive Manufacturing

Wen Dong, PhD

University of Pittsburgh, 2024

As an additive manufacturing process for fabricating metal components, laser powder bed fusion (L-PBF) and wire-arc directed energy deposition (wire-arc DED) have drawn increasing attention in the past few decades due to their advantages such as fast production, high customization, and waste reduction. During fabrication, the rapid, intense, and repeated heat input (laser beam or wire arc) leads to a complex thermal history in parts, resulting in significant residual stress and distortion. These residual stress and distortion can adversely affect product quality by increasing surface roughness, reducing dimensional accuracy, and introducing defects into the parts.

This dissertation is focused on improving the inherent strain (IS) method for predicting residual stress and deformation in parts manufactured by L-PBF and wire-arc DED processes. In addition, two frameworks based on the IS method for recoater interference prediction and distortion compensation in L-PBF are proposed. Chapter 2 introduces a new procedure for implementing the modified inherent strain (MIS) method. This procedure incorporates an additional solution step that uses mechanical properties at elevated temperatures, markedly improving the accuracy of the MIS method on residual stress prediction. Chapter 3 extends the MIS method to include the heat accumulation effect in the wire-arc DED process. This enhancement involves introducing a flashing heating simulation to calculate interpass temperature and applying temperature-dependent ISs in the MIS-based simulation. In Chapter 4, an integrated

simulation and experimental framework for predicting potential recoater interference in the L-PBF process is proposed. This framework addresses the previously undefined criterion for recoater interference and incorporates the edge effects when calculating the part deformation. In Chapter 5, a data-driven distortion compensation framework for the L-PBF process is presented. The framework employs a Gaussian process regression (GPR) model and reduced-order modeling to learn from experimentally-validated IS simulation data and generate the compensated shape.

Table of Contents

List of Tables

List of Figures

Preface

Reflecting on my five-year journey at the University of Pittsburgh, I am deeply thankful for the wealth of experiences and knowledge I have gained. I extend my gratitude to many who have provided invaluable guidance and support throughout my Ph.D., culminating in the completion of this dissertation.

I owe immense thanks to my Ph.D. advisor, Dr. Albert C. To, for guiding me through several challenging research problems and for granting me the freedom to explore my research interests. Despite their tight schedules, my sincere appreciation goes to my committee members, Dr. Qihan Liu, Dr. Xiayun Zhao, and Dr. Kevin P. Chen, for their invaluable input and suggestions on my proposal and dissertation. I am grateful to my colleagues in our group for their collaboration and assistance. My thanks to Dr. Xuan Liang, Dr. Qian Chen, Dr. Hao Deng, Dr. Hai Tran, Dr. Santanu Paul, Dr. Florian Dugast, Dr. Dinh Son Nguyen, Shawn Hinnebusch, Praveen Vulimiri, Basil Paudel, Xavier Jimenez, Seth Strayer, David Anderson, and others for their generous support and advice. I also extend thanks to Qirui Wang and Jieru Zhao in Dr. Kevin P. Chen's group for their valuable collaboration. Additionally, I am grateful to Brandon Blasko and Andrew Holmes at the University of Pittsburgh for their assistance with experiments.

Finally, my deepest and most heartfelt gratitude goes to my wife, Dr. Xing Wang, and my parents for their unwavering and unconditional support. Without their love and encouragement, this journey would not have been possible.

1.0 Introduction

1.1 Overview of Laser Powder Bed Fusion (L-PBF) and Wire-arc Directed Energy Deposition (wire-arc DED)

The ISO/ASTM 52900:2021 on "Additive Manufacturing — General Principles — Fundamentals and Vocabulary" categorizes AM processes into seven groups, as listed in Table 1.1. Among these AM processes, powder bed fusion and directed energy deposition for metal components are the primary focus of this study. More specifically, our attention is centered on the laser powder bed fusion (L-PBF) and wire-arc directed energy deposition (wire-arc DED) processes. Both of them involve intense and continuous thermal energy input, leading to the melting and solidification of materials.

Table 1.1 General categories for AM processes [1]

Process category	Abbreviation	Description
Binder jetting	BJT	A liquid bonding agent is selectively deposited to join powder materials
Directed energy deposition	DED	Focused thermal energy is used to fuse materials by melting as they are being deposited
Material extrusion	MEX	Material is selectively dispensed through a nozzle or orifice
Material jetting	MJT	Droplets of feedstock material are selectively deposited
Powder bed fusion	PBF	Thermal energy selectively fuses regions of a powder bed
Sheet lamination	SHL	Sheets of material are bonded to form a part
Vat photopolymerization	VPP	Liquid photopolymer in a vat is selectively cured by light-activated polymerization

The L-PBF process is one of the most popular metal AM processes [2, 3]. Its products have been widely used in aerospace, automotive, medical, and other industries due to their advantages of low cost, light weight, and high degrees of customization. A typical L-PBF system, as shown in Figure 1.1, involves a powder delivery system to prepare the powder bed and a scanner system to provide the energy for melting the material. The general procedure of producing one layer is that: (1) at the beginning of each layer, the powder delivery piston rises a layer thickness; (2) after that, the spreader or recoater blade moves parallel to the printing plane until a layer of powder (pre-placed power bed) covers the part that is being fabricated; (3) then, a laser beam generated by the scanner system follows a specific path to melt the powder; (4) the fabrication piston moves downwards by a layer thickness after re-solidification of the melted layer. This procedure repeats until the entire part is finished.

Building upon mature metal welding technology, wire-arc DED has been widely employed to fabricate medium to large-scale metal parts due to its low cost, high efficiency, and wide material range [4, 5]. In this process, metal wire serves as the feedstock and a welding arc is used as the heat source to deposit weld beads in a layer-by-layer fashion, building the net-shape components [6]. The common heat sources used in the wire-arc DED include gas metal arc welding (GMAW), gas tungsten arc welding (GTAW), and plasma arc welding (PAW) [5, 7, 8]. A schematic overview of the GMAW-based wire-arc DED system is shown in Figure 1.2. The heat source involved in the present study is a variant of GMAW, known as cold metal transfer (CMT) [9, 10]. The primary difference between CMT and the conventional GMAW process lies in CMT's ability to control the motion of wire feeding precisely.

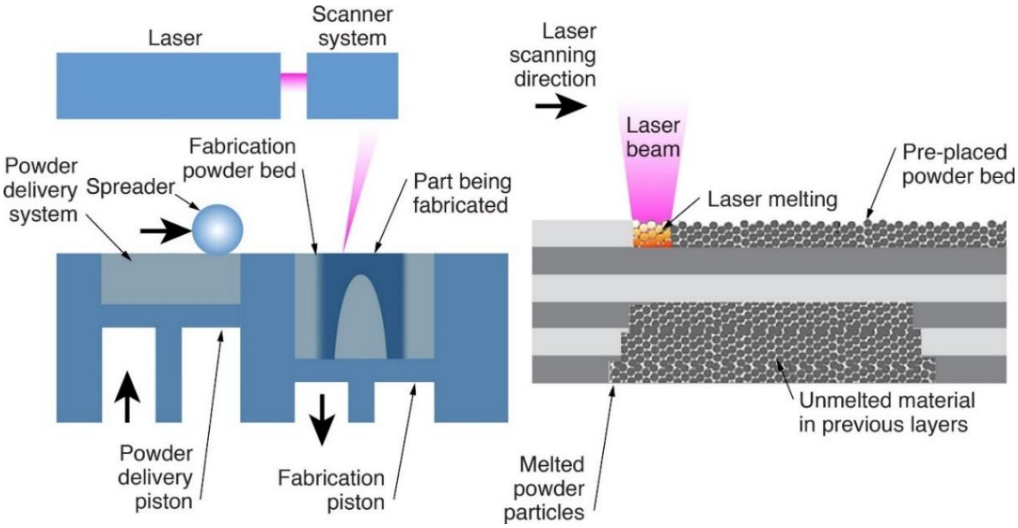

Figure 1.1 Schematic overview of the L-PBF system [11]

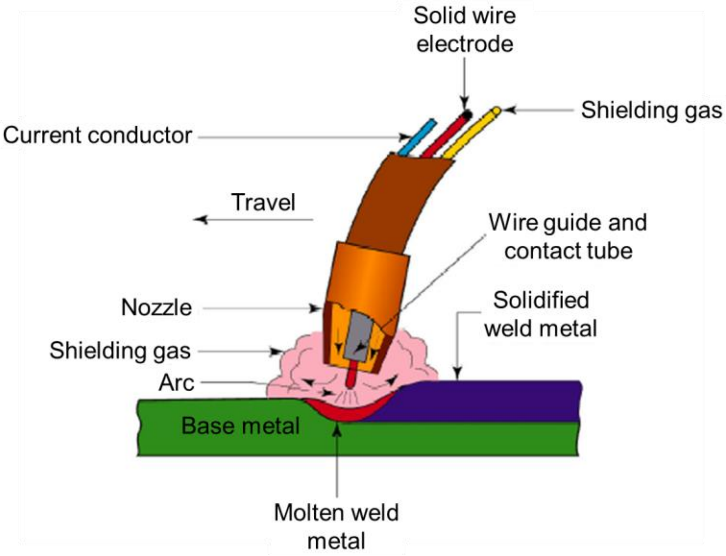

Figure 1.2 Schematic overview of the GMAW-based wire-arc DED system [12]

Compared with the traditional approaches such as subtractive and formative manufacturing, the L-PBF and wire-arc DED processes offer advantages including the production of customized designs, simplification of the supply chain, improved product performance, reduced production costs and so forth [13, 14]. Despite these benefits, both processes still face drawbacks that hinder their application. One of the most challenging drawbacks is the presence of residual stress and distortion in as-built parts, primarily caused by the large thermal gradients arising from repeated melting and solidification during the deposition [15, 16]. The residual stress and the associated component deformation are the bottlenecks of L-PBF and wire-arc DED processes, as they may inversely affect product quality [17]. These effects include compromising geometrical accuracy, affecting material properties (such as hardness and fatigue strength), reducing the feasibility of post-machining, and even causing build failure during the deposition [2, 3, 5, 9, 18, 19].

1.2 Multiscale Modeling on Residual Stress and Deformation Prediction in L-PBF and wire-arc DED

Considering the substantial influence of residual stress and distortion on product quality, numerous methods have been proposed to assess them in parts produced by L-PBF and wire-arc DED. The most direct method is experimental measurement; however, this approach is expensive and time-consuming. Particularly during the design stage, the part geometry and process parameters may undergo multiple modifications to meet customer requirements and standards. Conducting experiments after each modification is nearly infeasible. Numerical simulations have been extensively employed to evaluate residual stress and deformation at the design stage rapidly. Generally, there are three types of simulation models for L-PBF and wire-arc DED in terms of their fidelity, which limits the model size to the microscale, mesoscale, and macroscale (also called part-scale).

At a size of tens of microns, the microscale model has the ability to consider the fluid dynamics of melt pools as well as microstructure evolution. For example, Han et al. [20] quantitatively investigated the effect of interfacial forces, including thermocapillary forces, surface tension, and recoil vapor pressure, on the melt pool shape and fluid flow in the laser material interaction process by solving the thermal-fluidic problem via the finite difference method. Bauereiß et al. [21] used a numerical model based on the lattice Boltzmann method to study the defects formed during the L-PBF process by considering hydrodynamics, including capillary and wetting effects, in their work. Qian et al. [22] developed a multiphysics model involving thermal-fluid dynamics to investigate the influence of preheating temperature on molten pool morphology in the L-PBF process. This model employs the volume of fluid technique to track the free surface of a melt pool and is able to consider the buoyant flow, Marangoni convection, vapor recoil pressure, and heat radiation. Although the microscale model has a high resolution, it is only able to reflect the structural characteristics in a tiny area.

At the mesoscale level, the size of the model is tens of millimeters. Several simplifications are introduced to save computational expense because the solution domain is significantly expanded compared to the microscale models. An essential simplification is to replace the complex melt pool dynamics with a moving heat source, such as the Goldak double ellipsoidal [23] and Gaussian [24] models. The mesoscale model usually loses some field quantity prediction accuracy compared to the microscale one but still exhibits the influence of macroscopic parameters on the printing process, e.g., layer thickness, laser power, and laser scanning path. Li et al. [25] developed a 3D thermomechanical model to predict the melt pool geometry of the L-PBF process and investigate the influence of the scanning strategies and process parameters on the residual stress of the part. The model includes the temperature-dependent material properties of metal at powder, solid, and liquid states, and considers the layer shrinkage due to material solidification and evaporation. When modeling the L-PBF process for Ti6Al4V products, Tan et al. [26] considered the powder-liquid-solid transition and the metallurgical effects, i.e., solid-state phase transformation. Ding et al. [27] proposed a steady-state thermal model to predict the thermal field and a simplified mechanical model to evaluate the stress and deformation in large-scale parts. Lindgren et al. [28] developed a thermomechanical modeling approach for wire-arc DED processes, where a microstructure model for phase transformation of Ti6Al4V and a physics-based flow stress model for hardening are included.

The macroscale model is used to assess the stress and strain profile over the entire part. In most cases, it adopts a layer-by-layer or even one-shot deposition pattern, significantly decreasing the computational time [29, 30]. A number of great efforts have been made to improve the reliability of this class of models [31-34]. Among the macroscale modeling approaches, the finite element (FE)-based inherent strain (IS) method has gained significant attention recently. The IS method typically involves only static mechanical analysis in a layer-by-layer fashion and is computationally efficient.

1.3 Inherent Strain (IS) Method

The IS method was originally proposed by Ueda et al. to predict residual stress in welded structures, and it assumes that applying so-called inherent strains (ISs) to the welded area can reconstruct the strain/stress distribution formed by the complex welding process [35-37]. Due to the similarities between AM and welding processes, many researchers have started implementing the IS method for AM metal parts [38-42]. Based on how the ISs are calculated, the IS method can be divided into three categories: analytical, empirical, and numerical [43].

Analytical-based approaches utilize the material's thermal and mechanical properties. Yaghi et al. [32] defined the IS magnitude of a material as the ratio between its yield strength and

Young’s modulus, with both properties being estimated at room temperature. Alvarez et al. [44] calculated the IS values by multiplying the material’s equivalent coefficient of thermal expansion (CTE) by the temperature difference between the melting point and the initial value of each layer. The equivalent CTE depends on the actual CTE and is also influenced by the laser scanning strategy. Empirical-based approaches typically involve first experimentally measuring the distortion of several printed benchmark geometries, and then numerically calibrating or optimizing the ISs to minimize the discrepancy between the measured and simulated distortions. Bugatti and Semeraro [30] introduced a regression-based optimization algorithm, which utilizes distortion measurements from twin-cantilever beams produced via L-PBF processes to calibrate the ISs. Setien et al. [45] proposed a method that employs the Hooke-Jeeves direct penalty technique to solve the optimization problem and investigated the impact of scanning strategy on ISs. Siewert et al. [46] reported that, although the ISs are calibrated based on distortion, the predicted residual stress also exhibits a good agreement with measurements obtained via X-ray diffraction. Numerical-based approaches usually have hierarchical simulations where the ISs are computed. Keller and Ploshikhin [38] proposed a multiscale simulation framework to achieve the fast prediction of distortion for metal AM parts, including a micro-scale model for heat source calibration, a meso-scale hatching model to calculate the ISs, and a macro-scale layer model to predict the part distortion.

In this work, we primarily focus on a numerical-based approach, namely the modified inherent strain (MIS) method developed by Liang et al. [29, 47, 48] and Chen et al. [49] for powder DED and L-PBF processes.

1.4 Research Objectives

1.4.1 A New Procedure for Implementing the Modified Inherent Strain (MIS) Method with Improved Accuracy in Predicting Both Residual Stress and Deformation for L-PBF

The MIS method has been proved to accurately and rapidly predict deformation in metal parts produced by L-PBF processes, with diverse applications including topology optimization, path planning, crack prevention, and buckling analysis [42, 50-54]. However, the accuracy of MIS-based simulations in predicting residual stress has not been thoroughly investigated. In this work, it is shown that the current procedure of implementing the ISs in the MIS-based part-scale simulation is not proper for residual stress prediction. A new procedure is then proposed to improve the prediction accuracy. In the current procedure, the ISs are applied to each layer whose material properties are at ambient temperature. In contrast, the new procedure first applies ISs to a layer with material properties at elevated temperatures, then reverts the material properties to those at ambient temperature. This new procedure is more consistent with the physics underlying the MIS method.

1.4.2 Temperature-dependent MIS Method for Predicting Residual Stress and Deformation for wire-arc DED

In wire-arc DED processes, the interpass temperature — top surface temperature on the as-deposited material before the next layer — increases significantly with part height due to heat accumulation. This temperature variation critically influences the stress, strain, and microstructure evolution in the deposit. A major challenge in applying the MIS method to wire-arc DED is its inability to account for heat accumulation, as it applies constant ISs across the entire part. To address this issue, our work extends the MIS method to incorporate heat accumulation effects, making it suitable for large parts fabricated via wire-arc DED. In the extended method, the detailed process simulation is repeated under varying interpass temperatures to derive temperature-dependent ISs. To ascertain the interpass temperature for a given part, a flash heating simulation, incorporating part-scale transient thermal analysis, is employed. Instead of applying constant ISs layer by layer, our extended method divides each layer into segments following the deposition path, and then sequentially loads temperature-dependent ISs based on the interpass temperature of these segments. To enhance the applicability of the approach, solid-state phase transformation modeling is also integrated so that it can be applied to materials like Ti6Al4V.

1.4.3 Predicting Recoater Interference for L-PBF by Considering Both Global Thermal Deformation and Local Edge Deformation Using the MIS Method

Preventing recoater interference and crash is crucial in L-PBF processes for printing parts with overhanging features. The interference and crash may compromise product quality by increasing surface roughness, reducing dimensional accuracy, and introducing defects into the parts. While in-situ monitoring is helpful in detecting or predicting recoater interference or crash a few layers in advance, having an efficient and accurate tool for predicting these abnormalities during the part’s design phase is essential. The existing simulation works have two limitations: (1) the criterion for interference is not clearly defined, and (2) they primarily consider thermal-gradient-induced deformation in the part but do not account for the edge effect — the formation of elevated edges caused by melt pool dynamics — due to limitations in model fidelity at the part scale. This work proposes an integrated simulation and experimental framework to predict potential recoater interference for a given part designed for L-PBF fabrication. In the framework, the criterion for recoater interference is defined based on part deformation. Specifically, interference occurs when the deformation of the part in the build direction exceeds the thickness of a newly spread powder layer after recoating. The largest deformation in the build direction is assumed to occur at the edge of a part and is the sum of two contributions: global thermal deformation and local edge deformation. The global thermal deformation is computed using the MIS method with location-dependent ISs, and the local edge deformation is estimated by reconciling the MIS simulated and experimentally measured deformation on several overhang wedges.

1.4.4 Data-driven Distortion Compensation for L-PBF Process Using the Gaussian Process Regression (GPR) and IS Method

The repeated melting and solidification in the L-PBF process lead to significant thermal gradients, resulting in notable distortion of the as-built part compared to the design shape. Distortion compensation has been widely used to address this issue, involving pre-deforming the part design so that the as-built shape aligns with the target shape. Generally, implementing distortion compensation includes two main tasks: determining the deformation caused by the deposition process and calculating the pre-deformation to be applied to the design shape. Commercial software packages such as ANSYS and Autodesk Fusion 360 Netfabb typically employ thermomechanical simulations to calculate part deformation and utilize an iterative process to determine the pre-deformation. Although this approach is straightforward to implement, it is computationally intensive. In this work, we introduce a data-driven distortion compensation framework for the L-PBF process. The framework employs an experimentally calibrated IS method to calculate the deposition-induced deformation and uses Gaussian process regression (GPR) to compute the pre-deformation and create the compensated geometry. In the GPR model, we include not only the design shape and its corresponding deformation but also several trial geometries similar to the design, along with their respective deformations. This approach incorporates a broader range of deformation data and expands the training dataset, thereby enhancing the accuracy of the GPR model.

2.0 A New Procedure for Implementing the Modified Inherent Strain (MIS) Method with Improved Accuracy in Predicting Both Residual Stress and Deformation for L-PBF

2.1 Modified Inherent Strain Method

2.1.1 Origin of the Residual Stress

We use a single-track welding example, as shown in Figure 2.1(a), to illustrate the origin of the residual stress in welding processes, which also applies to L-PBF and wire-arc DED. In this example, several assumptions and simplifications are made: (1) the welding process is represented as a one-dimensional isotropic ideally-plastic bar undergoing heating and cooling; (2) the bar is assumed to be fixed at both ends, maintaining zero total strain at all times; (3) the total strain (ε^{total}) of the bar comprises only thermal ($\varepsilon^{thermal}$), elastic ($\varepsilon^{elastic}$), and plastic ($\varepsilon^{plastic}$) strains, ignoring other strain terms. The justification for the second simplification is that the dimension of the weld is typically much smaller than the parent metals it joins (such as sheets and I-beams). As a result, these parent metals act as a strong constraint on the weld.

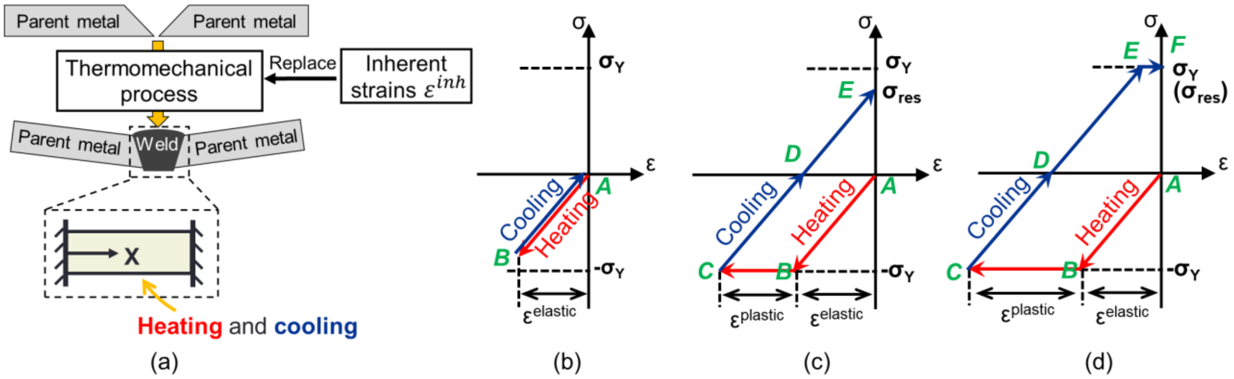

(a) (b) (c) (d)

Figure 2.1 Illustration of the origin of the residual stress.

Figure 2.1(b) through (d) illustrate the stress-strain curve of the bar under three different thermal cycles. In Figure 2.1(b), the bar undergoes elevated temperatures at the heating stage, leading to positive thermal strain and a tendency to expand. Since both ends are firmly constrained, compressive elastic strain and corresponding stress develop, as Arrow *AB* shows. The cooling phase begins next, marked by Arrow *BA*. As the bar returns to its initial temperature, the thermal strain vanishes, and the bar fully recovers without any residual stress. For Figure 2.1(c) and (d), the compressive stress induced during the heating phase eventually reaches the yield strength of the bar, causing plastic deformation, indicated by Arrow *BC*. As the cooling begins, both the compressive elastic strain and stress within the bar decrease, as depicted by Arrow *CD*. At Point *D*, the stress in the bar disappears, and the elastic strain returns to zero. The remaining thermal strain is counterbalanced by the plastic strain developed during the heating stage. As the temperature continues to drop, a positive elastic strain emerges, compensating for the diminishing thermal strain and keeping the total strain at zero, as shown by Arrow *DE*. As a result, the stress in the bar becomes tensile. In Figure 2.1(c), the stress-strain curve arrives at point E as the temperature returns to its initial state. In Figure 2.1(d), the tensile stress attains the yield strength of the bar, and the curve finally reaches point F. The remaining tensile stress in the case of Figure 2.1(c) and (d) is referred to as the residual stress.

From the above description, it can be deduced that, as thermal strain diminishes, the plastic strain generated during the heating phase is the cause of the residual stress in the bar. A more general statement is that residual stress arises to accommodate inelastic deformation.

2.1.2 Intermediate and Steady Thermal States

Initially, Ueda et al. [35-37] proposed the inherent strain (IS) method to predict residual stress and deformation in welded structures. The basic idea is that the strain/stress distribution within the weld can be reconstructed by applying the inherent strains. In the IS method, the thermomechanical process in the welded structure is considered a black box, and the exact happenings inside this box are not important.

Ueda et al. [35-37] defined the IS as the inelastic strain that remains in the welded structure as it returns to its initial temperature, since this inelastic strain is responsible for the residual stress. For convenience, we define a steady thermal state to be when the welding process has finished and the welded structure has returned to its initial ambient temperature. Then, the inherent strain ε^{inh} can be expressed as:

$$\varepsilon^{inh} = \varepsilon^{inelastic} = \varepsilon_s^{total} - \varepsilon_s^{elastic} \tag{2.1}$$

where $\varepsilon^{inelastic}$ denotes the inelastic strain. ε_s^{total} and $\varepsilon_s^{elastic}$ denote the total strain and elastic strain calculated at the steady thermal state.

A fundamental assumption of the original IS method for the welding process is that the 1-D bar in Figure 2.1(a) can be considered fixed at two ends due to the relatively small dimension of the weld. Based on this assumption, all the strain is constrained within a small region around the weld during the welding process and can be easily measured or computed. However, in metal AM processes like L-PBF and wire-arc DED, this assumption may not hold since the deposit is comprised of multiple tracks and layers, meaning that no stable and consistent “parent metal” can provide the fixed boundary conditions for each track or layer.

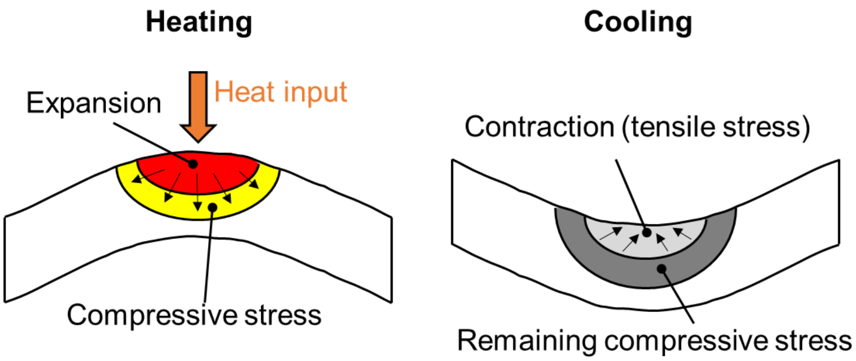

Figure 2.2 Illustration of the stress evolution in the L-PBF process. (Adapted from Ref. [55])

Figure 2.2 illustrates the stress evolution at a small area in the L-PBF process. At the heating stage, laser irradiation creates a melt pool and makes the temperature of the surrounding area rise sharply, leading to significant thermal expansion. The expansion of this region is constrained by the surrounding cooler areas, which leads to the development of compressive stress and may also produce a considerable amount of elastic and plastic strain in the heated area. Once the laser moves to a different location, the heated area starts to cool down, leading to thermal contraction. This contraction, still restricted by the adjacent material, results in tensile stress. Meanwhile, as heat flows into neighboring areas, they experience thermal expansion, which is constrained by their more distant surroundings, thereby producing compressive stress. As a result, the strain initially generated during the heating stage can also "migrate" into surrounding areas along with the heat flow. When the deposit returns to ambient temperature and the thermal strain diminishes, the ε_s^{total} in Equation (2.1) represents only the total strain remaining in that area at the steady state, not including the strain that has migrated during the cooling stage. The complexity of this problem further increases in a general case with multiple tracks and layers because the strain may "migrate" continuously between adjacent tracks and layers.

To address this problem, Liang et al. [29, 47, 48] and Chen et al. [49] introduced another thermal state called the intermediate state and developed a modified inherent strain (MIS) method for the L-PBF process. For a concerned material point, the intermediate state is defined as the thermal state when the heat source moves closely and stimulates its extreme (compressive or tensile) strains. In the MIS method, the ε^{inh} is calculated as the difference of strain terms at the intermediate and steady thermal states:

$$\varepsilon^{inh} = \varepsilon_i^{mechanical} - \varepsilon_s^{elastic} \tag{2.2}$$

In the formulation above, the mechanical strain at the intermediate state $\varepsilon_i^{mechanical}$ is written as follows:

$$\varepsilon_i^{mechanical} = \varepsilon_i^{elastic} + \varepsilon_i^{plastic} = \varepsilon_i^{total} - \varepsilon_i^{thermal} \tag{2.3}$$

where ε_i^{total}, $\varepsilon_i^{thermal}$, $\varepsilon_i^{elastic}$, $\varepsilon_i^{plastic}$, denote the total, thermal, elastic and plastic strain of the material at the intermediate state, respectively.

In Equations (2.1) and (2.2), the term $\varepsilon_s^{elastic}$ is consistent, representing the elastic strain at a material point at the steady thermal state, that is, when the part returns to ambient temperature. In the MIS method, the total strain at the steady state ε_s^{total} is substituted with the mechanical strain at the intermediate state $\varepsilon_i^{mechanical}$. This mechanical strain is also equivalent to the total strain at the intermediate state minus the corresponding thermal strain ($\varepsilon_i^{total} - \varepsilon_i^{thermal}$).

For a material point at the intermediate thermal state, we can assume that it is strongly constrained by the surrounding cooler material since, by definition, the heat source is heating this point. At this moment, the $\varepsilon_i^{mechanical}$ includes all the elastic and plastic strain generated in this area, without any strain "migration". Therefore, substituting ε_s^{total} with $\varepsilon_i^{mechanical}$ is considered a practical approach to mitigate the effects of multiple tracks and layers on the calculation of IS for L-PBF processes.

2.1.3 General Procedure of the MIS Method

The numerical implementation of the MIS method is based on finite element analysis (FEA) and includes two steps: extraction and loading of the ISs, as shown in Figure 2.3. In the detailed process simulation, the meso-scale finite element (FE) model of a representative volume is used to extract ISs through a sequentially coupled thermomechanical analysis. The detailed simulation involves specific process parameters including laser power, layer thickness, scanning velocity and scanning path. The obtained ISs are then loaded onto a part-scale FE model to compute residual stress and deformation through a static mechanical analysis, which constitutes the MIS-based part-scale simulation. The element birth and death technique [56, 57] is employed in both the detailed process and part-scale simulation. In the former, the elements of the deposited materials are activated step by step as the heat source travels; while in the latter, elements are activated in a layer-by-layer fashion.

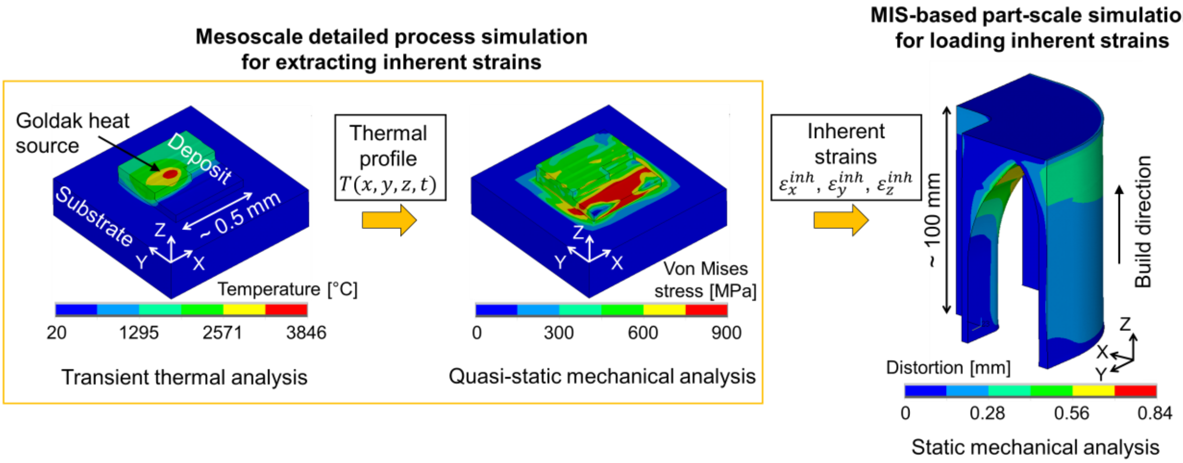

Figure 2.3 General procedures of the MIS method. (Adapted from Ref. [58, 59])

In the detailed process simulation, the mesh size is set smaller than the diameter of the laser beam spot to ensure the accuracy of the FE model. The thermal field for the entire deposition process is simulated first and then the temperature history profiles from the thermal analysis are fed into the mechanical analysis. For the L-PBF process, such a small FE model is sufficient to provide accurate ISs because (1) the part is printed under almost the same process parameters, laser scanning strategies, and boundary conditions except for edges and surfaces; (2) although laser in the following layer may remelt the previous layer and change its strain and stress field, this inter-layer effect is assumed to exist only in a few layers (typically two or three) following the layer of interest [60, 61]. Note that the shear strain components of the IS are neglected since their influence is limited [29, 61].

In the MIS-based simulation, a part-scale FE model that represents a real part geometry is used in static mechanical analysis to predict residual stress and deformation. In the previous MIS-based study, the part-scale model only employs material properties at the ambient temperature [30]. IS values are assigned as CTEs of the deposition. Residual stress and deformation are induced by increasing the temperature of the layer by a unit degree. The entire simulation is performed in a layer-by-layer fashion to incorporate the inter-layer effect naturally, as shown in Figure 2.4. However, in layer-wise modeling, the part-scale FE model cannot have as many thin layers as the practical metal depositions; otherwise, the computational cost of simulating too many layers would be prohibitive. Hence, a lumping-layer technique is adopted [62] to accelerate the layer-wise simulation. Tens or even hundreds of consecutive physical layers in the actual part are lumped together as one equivalent numerical layer in the simulation. This technique has proven effective when simulating the L-PBF process [61].

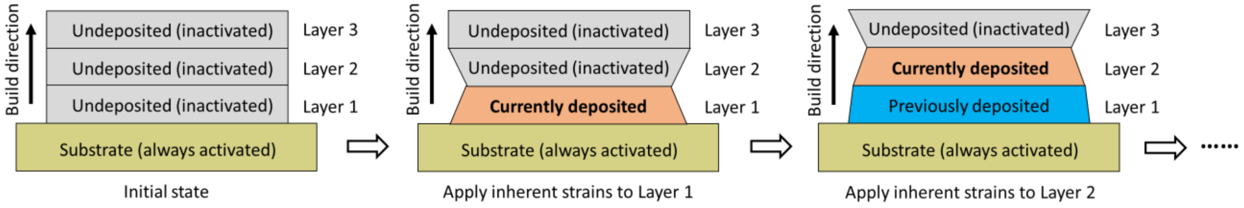

Figure 2.4 Analysis workflow of the MIS-based part-scale simulation.

2.2 Example of Implementing the MIS Method

2.2.1 Model Geometry and Process Parameters

Figure 2.5(a) shows the FE model of a three-layer single-walled structure. The substrate is 150 mm in length, 60 mm in width, and 4 mm in thickness. The deposit has a dimension of 100×6.4×3 mm^3, consisting of uniform 8-node hexahedral elements (2×3.2×1 mm^3). Both the substrate and deposition are made of 17-4PH. In the thermal process simulation, the Goldak double ellipsoidal heat source model is adopted [23], as shown in Figure 2.5(b), where q is the heat energy density and Q is the effective power. In addition, a_f and a_r are respectively the front and rear half-length, b the half-width, and c the depth of the heat source, which moves along the X-direction in each layer of the deposition. It is assumed that $a_f = a_f$ in the L-PBF process for simplicity [29, 49]. Thermal boundary conditions are shown in Figure 2.5(c) [63]. Natural convection ($h_{natural}$) and radiation ($\varepsilon_{radiation}$) are applied to upper surface of the substrate and deposition. Forced convection (h_{forced}) is applied to bottom surface of the substrate. In the mechanical analysis, one end of the substrate (plane X = 0) is fixed while the other end is free to move. After printing, when the whole system recovers to ambient temperature, the substrate bends like a cantilever beam due to the residual stress, as shown in Figure 2.5(c). Table 2.1 lists the process-modeling parameters. Here, the FE model geometry, heat source, and process parameters are quite different from those of a typical L-PBF process. We intentionally choose this simple geometry and these parameters so that it is computationally acceptable to use the same FE model for both detailed process and MIS-based part-scale simulation. As a benefit, the residual stress and deformation obtained by these two simulations can be directly compared.

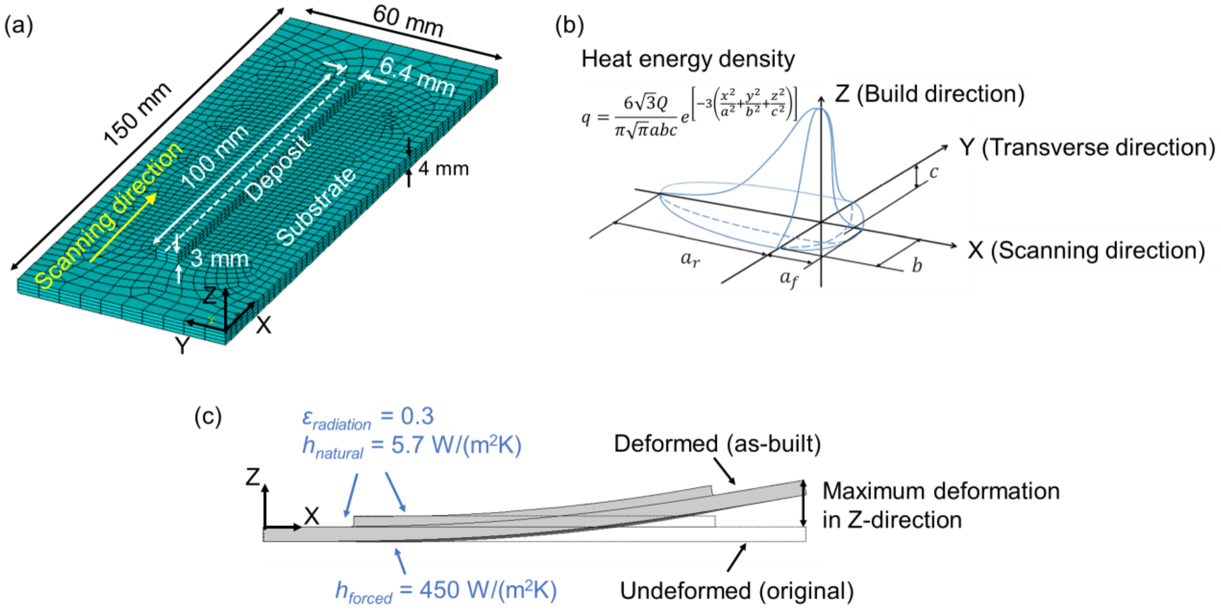

Figure 2.5 (a) FE model of the single-walled deposition and substrate; (b) Goldak double ellipsoidal heat source model [64]; (c) thermal boundary conditions and residual deformation pattern.

Table 2.1 Process-modeling parameters for the single-walled deposit

Parameter	Value
Heat source half-length $a = a_f = a_r$	3.2 mm
Heat source half-width b	3.2 mm
Heat source depth c	1.0 mm
Effective power Q	937 W
Laser scanning velocity v	4.0 mm/s
Layer thickness h	1.0 mm
Dwell time between two layers t_{dwell}	175 s

2.2.2 Governing Equations and Material Modeling

In the detailed process simulation, the temperature field in the transient thermal analysis is determined by solving the governing equation [49, 65],

$$\rho C_p \frac{dT}{dt} = \frac{\partial}{\partial x}\left(k\frac{\partial T}{\partial x}\right) + \frac{\partial}{\partial y}\left(k\frac{\partial T}{\partial y}\right) + \frac{\partial}{\partial z}\left(k\frac{\partial T}{\partial z}\right) + Q_{in} \tag{2.4}$$

where ρ is the material density, C_p is the specific heat, T is the temperature, t is the time, k is the thermal conductivity, Q_{in} is the internal heat source. x, y, and z denote the global coordinates of the material point.

The governing equation of the mechanical analysis in the detailed process and part-scale simulation is [49],

$$\nabla \cdot \boldsymbol{\sigma} + \boldsymbol{b} = 0 \tag{2.5}$$

where $\boldsymbol{\sigma}$ is the stress tensor and $\boldsymbol{b}$ denotes the body force vector.

The mechanical behavior of the material is considered to be ideal plastic with von Mises yield criterion [49, 66]:

$$\boldsymbol{\sigma} = \boldsymbol{C}\colon \boldsymbol{\varepsilon}^{elastic} \tag{2.6}$$

$$\boldsymbol{\varepsilon}^{elastic} = \boldsymbol{\varepsilon}^{total} - \boldsymbol{\varepsilon}^{plastic} - \boldsymbol{\varepsilon}^{thermal} \tag{2.7}$$

$$\boldsymbol{\varepsilon}^{thermal} = \boldsymbol{\alpha}\left(T - T_{ref}\right) \tag{2.8}$$

$$\sigma_v = \sqrt{\frac{3}{2}\sigma_{ij}\sigma_{ij} - \frac{1}{2}(\sigma_{kk})^2} \tag{2.9}$$

where $\boldsymbol{C}$ is the fourth-order tensor of elastic moduli. $\boldsymbol{\varepsilon}^{total}$, $\boldsymbol{\varepsilon}^{elastic}$, $\boldsymbol{\varepsilon}^{plastic}$, and $\boldsymbol{\varepsilon}^{thermal}$ are tensors denoting the total, elastic, plastic, and thermal strain, respectively. α is the coefficient of thermal expansion (CTE), T and T_{ref} respectively denote the material temperature and the reference temperature (20 °C in the present work). σ_v represents the von Mises stress and σ_{ij} denotes the Cartesian stress component.

Temperature-dependent material properties used in the detailed process simulation are given in the Appendix. Theoretically, the material properties should be able to cover the full range of temperature that the material may experience during the heating and cooling cycles, from ambient temperature to melting point and even higher temperature. However, this is impractical in the current simulation for three reasons. First, it is difficult to obtain material properties at temperatures close to or above the melting point through experiments directly. Second, the current detailed process simulation only considers the deposit as solid state, and no thermal and mechanical interactions involving liquids and gases within the melt pool are modeled. It is not necessary to employ material properties at very high temperatures. Third, as the temperature increases, the metal material becomes softer, oftentimes making the mechanical analysis difficult to converge. Therefore, based on the recommendation by Lindgren [67], we introduce a cut-off temperature T_{cut}, above which the material properties are kept constant. The selection of T_{cut} depends on available experimental data and also the required simulation accuracy. Setting the melting point of the material T_m as a reference, the *Computational Welding Mechanics* textbook by Lindgren [67] proposed three levels of the cut-off temperature corresponding to different simulation accuracy: (1) $T_{cut} \geq 0.5T_m$ for “basic” simulations; (2) $T_{cut} \geq 0.7T_m$ for “accurate” simulations, and (3) $T_{cut} \geq T_m$ for “very accurate” simulations where the fluid flow should be taken into account. In this study, most of the material properties listed in the Appendix have $T_{cut} \geq 0.7T_m$, indicating that the detailed process simulation is “accurate”. The latent heat of fusion is included to consider the solid-liquid phase transition. In ANSYS, it is done by defining the enthalpy. As a function of material temperature T, enthalpy is the integral of the product of the specific heat and density over temperature [68, 69]:

$$H(T) = \int_{T_0}^{T} \rho(T) C_p(T) dT + \rho_* \beta L \tag{2.10}$$

$$\beta = \begin{cases} 0 & , \quad T \leq T_S \\ (T - T_S)/(T_L - T_S) & , \quad T_S < T \leq T_L \\ 1 & , \quad T > T_L \end{cases} \tag{2.11}$$

where H is the enthalpy, ρ is the material density, C_p is the specific heat, $T_0 = 20$ ℃ is set as the reference temperature at which the enthalpy is zero, and L is the latent heat. T_S and T_L are the solidus and liquidus points of the material, respectively. For simplicity, during the phase transition, the material density ρ_* is considered as a constant and evaluated at $(T_L + T_S)/2$.

Regarding AM modeling, some researchers have reported that, in thermal analyses where only the solid phase is considered, the peak temperature of the metal material can be far higher than its real melting point [49, 70, 71]. There are several reasons that may explain this problem, such as inaccurate material properties used for high temperatures, lack of fluid dynamics of the molten pool, and errors introduced by numerical algorithms. At the present stage, the aforementioned problem cannot be fully eliminated. In mechanical analyses, since thermal strains are related to the temperature difference, the abnormally high peak temperature in the simulation may lead to extremely large thermal strains, resulting in unreasonable residual stress and strain fields. To reduce this error as much as possible, we also introduce a cut-off temperature for thermal strain and set it to the solidus point T_S of the material, as shown in Figure 2.6. The thermal strain $\varepsilon^{thermal}$ is calculated by Equation (2.8) for temperatures lower than T_{cut}, and kept constant for temperatures higher than T_{cut}.

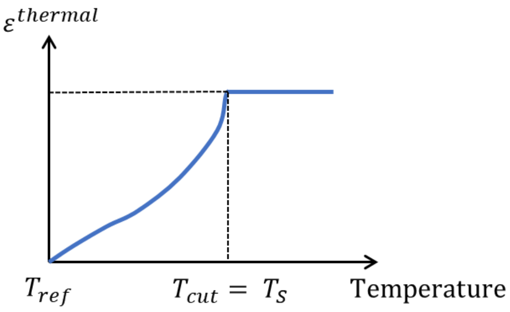

Figure 2.6 Schematic illustration of the cut-off temperature for thermal strains.

The mechanical behavior of the non-melting powder bed has little effect on thermomechanical simulations for the L-PBF process. Usually, there are two ways to deal with the mechanical properties of fresh powder. One is to scale down the yield strength and Young's modulus of the bulk material (for example, multiplying a coefficient of 0.1) and assign these values to powder [72]. The other is to use the element birth and death technique that has been widely adopted in commercial simulation codes [26]. This technique can deactivate the powder by multiplying the element stiffness by a reduction factor of around 10^{-6}. In this study, the second method is employed. As the heat source moves, its surrounding inactive elements will be activated and recover to their original stiffness.

2.2.3 Extraction of Inherent Strains

After the detailed process simulation, ISs are determined based on the temperature and strain history of each element in the deposit. Here, we use the temperature and mechanical strain (in the X- and Z-direction) history of a typical element (Figure 2.7) to illustrate how to calculate the ISs through Equation (2.2) and (2.3). The mechanical strain history in the Y-direction is not given because it is found to be similar to that in the X-direction.

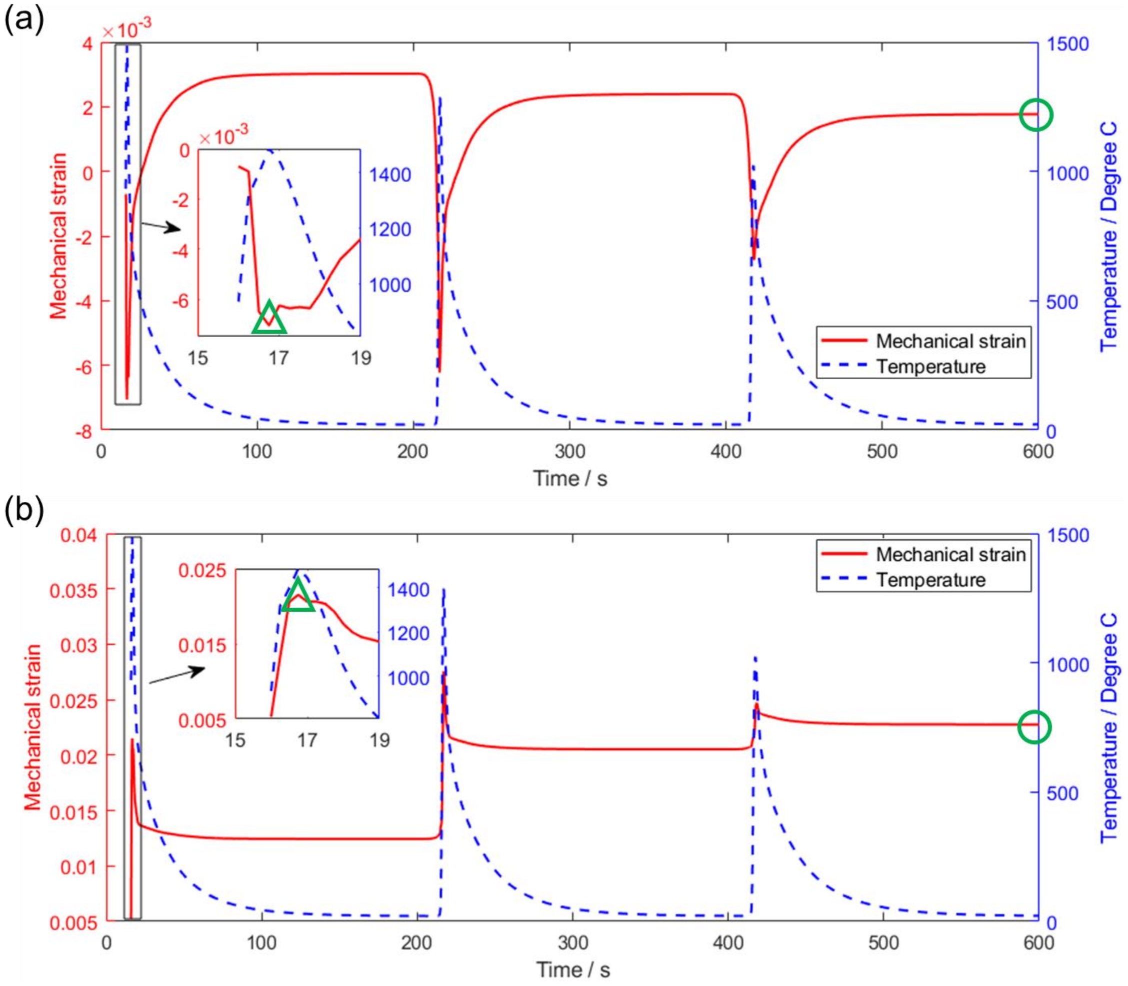

Figure 2.7 History plot of the temperature and mechanical strain in the (a) X-direction and (b) Z-direction for a typical element in the single-walled deposit. Hollow circles denote the steady thermal state, and hollow triangles denote the intermediate thermal state.

The three temperature peaks in Figure 2.7 indicate that this element is located in the first layer of the deposit (three layers in total). It is easy to find the steady term $\varepsilon_s^{elastic}$ in Equation (2.2), that is, the elastic strain when the deposit decreases to ambient temperature. In this example, the elastic strain at t = 600 s can be considered as the steady term (marked by hollow circles in the figure). The intermediate term $\varepsilon_i^{mechanical}$ can be identified more clearly in the zoomed views in Figure 2.7(a) and (b). It corresponds to the minimum in the X- and Y-directional mechanical strain history and the peak in the Z-directional (see hollow triangle markers in the zoomed view).

At the intermediate state, the moving heat source controls the strain evolution in a small area around the concerned material point because it causes a very large but localized thermal gradient. The intermediate term $\varepsilon_i^{mechanical}$ represents the effects of this transient thermal gradient. At this instant, the effect of the global thermal gradient induced by far-field boundary conditions can be ignored; for example, the free heat convection on the outer surface of the part and heat conduction between the substrate and fixtures. After the heat source moves away, the material point of interest continually undergoes several thermal cycles due to the subsequent melting, solidification, and cooling processes. At this stage, since the material point's temperature is relatively lower than that in the intermediate state, the strain evolution of the material point mostly depends on the temperature variation of the surrounding deposition and the far-field boundary conditions. This explains why the second term, a steady source $\varepsilon_s^{elastic}$, should be taken into consideration. Though it is called "steady", the second term actually reflects the continuous and accumulative effect of the global thermal gradient from the intermediate state to the steady state. In addition, only three normal components of the ISs are extracted.

The variation in mechanical strain at the intermediate state can be attributed to the changing thermal gradient near the melt pool [73]. Within the melt pool itself, the material, being in a liquid state, is stress-free. In contrast, the surrounding heat-affected zone (HAZ) is solid and maintains higher temperatures than its adjacent regions. This causes the HAZ to expand but be constrained by the cooler neighboring material, leading to the formation of compressive stress. As illustrated in Figure 2.8, when region P is at the center of the melt pool, it remains liquid and unstressed. As the melt pool moves forward, region P transitions into the heat-affected zone and starts to experience compressive stress. The compressive plastic strain may also develop if this stress reaches the material's yield strength. As the laser heat source moves further away over time, region

P begins to cool and tends to shrink. Due to the constraints from the surrounding material, tensile stresses develop in region P.

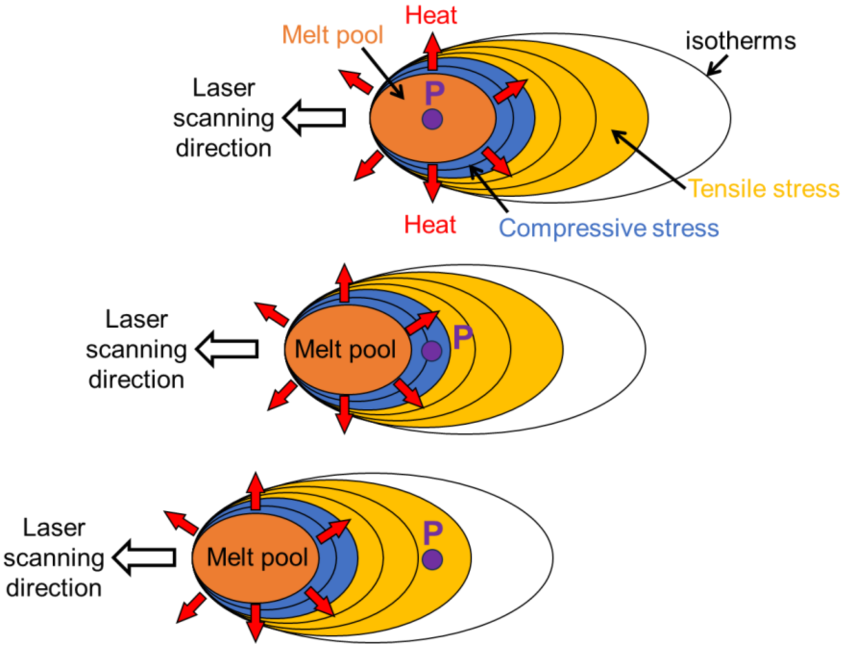

Figure 2.8 Schematic illustration of the thermal stress around the heat source.

In the zoomed view of Figure 2.7(a), upon element activation, the mechanical strain in the X-direction is compressive (negative) and reaches the minimum at the intermediate state. This is caused by constrained thermal expansion. After the intermediate state, the compressive mechanical strain decreases in magnitude and gradually becomes tensile due to constrained thermal shrinkage. The mechanical strain in the Y-direction has similar trends. In contrast, as shown in the zoomed view of Figure 2.7(b), the mechanical strain in the Z-direction is positive at the intermediate state, which can be explained by the Poisson effect. In particular, the constraint in the Z-direction (out-of-layer plane) is weak compared to those in the X- and Y-direction (in-layer plane) as there is no material on top of the deposit yet; therefore, the compressive mechanical strain in the X- and Y-direction leads to tensile strain in the Z-direction. After element-by-element extraction, the IS values are averaged into a vector for each layer, as listed in Table 2.2.

Table 2.2 Extracted ISs for each layer of the single-walled deposit

	X-direction	Y-direction	Z-direction
Layer 1	-0.0111	-0.0140	0.0222
Layer 2	-0.0071	-0.0106	0.0152
Layer 3	-0.0067	-0.0095	0.0137

2.2.4 Drawback of the Existing MIS Method

The extracted ISs are then applied to the same three-layer single-walled model following the procedure described in Section 2.1.3. For the detailed process and MIS-based simulation, the maximum residual deformation in the Z-direction is 6.477 mm and 6.660 mm, respectively, which shows the good accuracy of the existing MIS method in residual deformation prediction. However, Figure 2.9 shows that the overall residual von Mises stress of the deposition predicted by the MIS-based simulation is close to the yield strength of the material, which is much higher than the results obtained by the detailed process simulation. Therefore, it is noted that the existing MIS method is inaccurate in evaluating the residual stress and should be modified to improve its accuracy. More technical details are introduced in the following section.

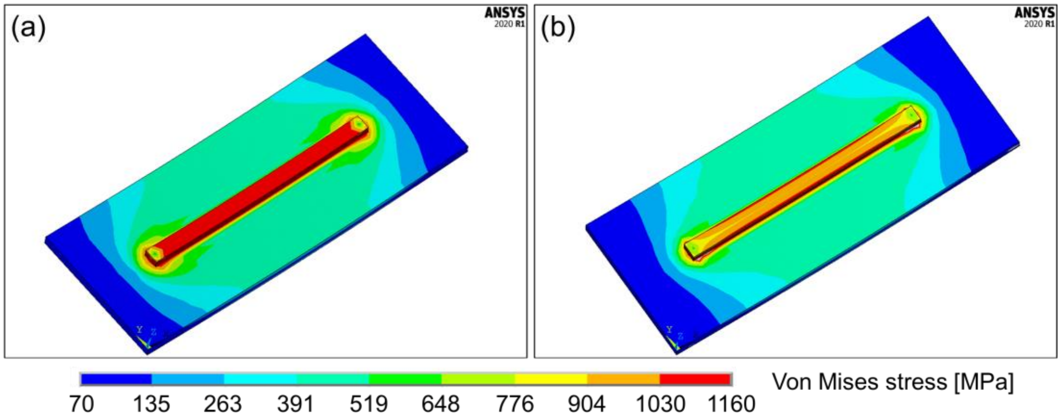

Figure 2.9 Profile of the residual von Mises stress obtained from (a) detailed process simulation and (b) MIS-based simulation.

2.3 New Implementation Procedure in Part-scale Simulation

To further improve the performance of the MIS method, we first analyze possible source of inaccuracy in residual stress prediction. The good agreement of overall residual deformation indicates that total strains induced in the MIS-based simulation are reasonable. Therefore, the IS values determined by the detailed process simulation are reliable. The overestimation in residual stress level (see Figure 2.9(b)) is found to be caused by incorrect mechanical response in the MIS-based simulation, that is, the relative proportion of elastic and plastic strains in the total strains are incorrect. After thoroughly examining the existing procedure, we have found the use of constant ambient temperature material properties in the MIS-based simulation can be a potential source of error. As described in Section 2.1, ISs are comprised of the intermediate term $\varepsilon_i^{mechanical}$ and the steady term $\varepsilon_s^{elastic}$. By definition, for a material point, $\varepsilon_i^{mechanical}$ is induced when the heat source is close by, suggesting that the material is experiencing an instant and relatively high temperature. As for $\varepsilon_s^{elastic}$, it is induced from the intermediate state to the steady state, reflecting the influence of the subsequent temperature variation caused by the global thermal gradient on the material point of interest. It has to be noted that although the term $\varepsilon_i^{mechanical}$ is induced instantly by the localized thermal gradient at the intermediate state, the subsequent global thermal gradient can also cause the induced strain to change until the steady state is reached. In other words, the evolution of the IS can be divided into two steps: 1) at the intermediate state, the localized thermal gradient induces $\varepsilon_i^{mechanical}$; 2) from the intermediate state to the steady state, the global thermal gradient induces $\varepsilon_s^{elastic}$ and also alters the previously generated $\varepsilon_i^{mechanical}$. Thus, in the MIS-based simulation, applying ISs using ambient temperature properties solely cannot fully reflect the effect of localized and global thermal gradients on the mechanical behavior, and thus fails to capture the correct relationship between elastic and plastic strains in the final cooled metal parts.

Based on the above discussion, the implementation procedure of the MIS-based simulation needs some modification. A new procedure involving the material change technique is proposed. The workflows of both the existing and new procedures are shown in Figure 2.10. For each layer of the deposition, the new procedure contains two sequential static equilibrium steps: (1) ISs are applied to the layer using material properties (Young's modulus, yield strength, etc.) at the intermediate state temperature T_i and the equilibrium is solved; (2) the material properties of the current layer are then changed to those at the steady state temperature T_s (ambient temperature) and the equilibrium is solved again, while the ISs are kept the same as in the previous step. This new procedure is repeated for each layer until the entire part is finished. In the first step, material properties at T_i are assigned to the layer because it is the temperature where the term $\varepsilon_i^{mechanical}$ is induced. Although the term $\varepsilon_s^{elastic}$ is measured at steady state in our model, it actually represents the conversion of thermal strain into elastic strain from temperature T_i to temperature T_s, and thus this term is also added in the first step of the new procedure. In the second step of the procedure, we use the material change technique to simulate the temperature change from T_i to T_s. By doing so, the effects of the global thermal gradient on the evolution of $\varepsilon_s^{elastic}$ and $\varepsilon_i^{mechanical}$ are both considered.

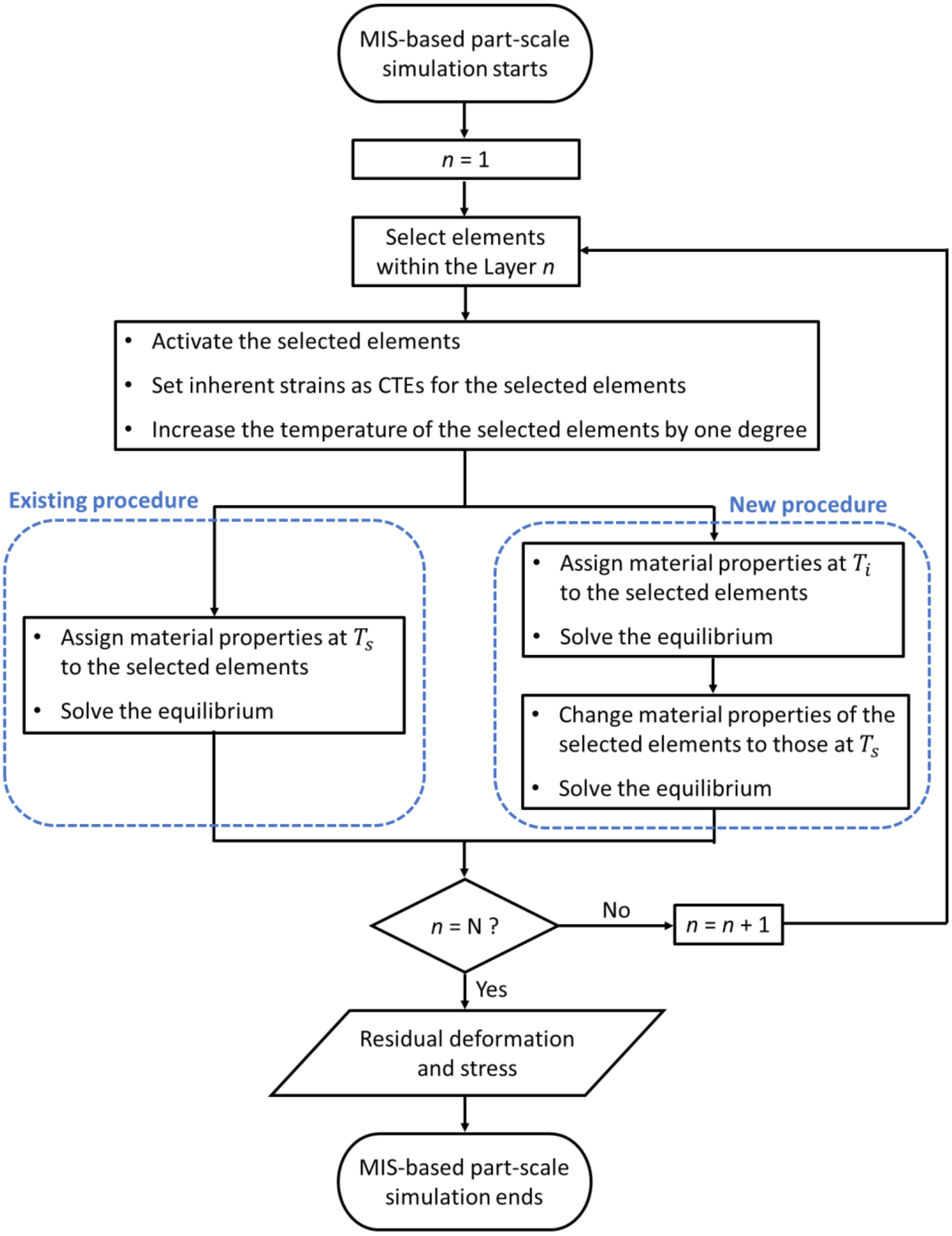

* *T_i and T_s are material temperatures at the intermediate and steady state, respectively*

* *N is the number of total lumped layers in the FE model*

Figure 2.10 Comparison of the existing and new procedures for MIS-based part-scale simulation.

As a proof of concept for the new procedure, the ISs extracted in Section 2.2.3 are applied to the three-layer single-walled FE model again but using the new procedure. The maximum deformation in the Z-direction regarding different types of simulations is listed in Table 2.3. Given that the error is only -3.6%, it is acceptable to claim that the new procedure can also accurately predict the distortion. The von Mises stress profile is shown in Figure 2.11(a). For quantitative comparison, von Mises stress along the top centerline of the single-walled deposit (see the dashed line in Figure 2.5(a)) is plotted in Figure 2.11(b). It can be seen that compared with the detailed process simulation, the MIS-based simulation with the new procedure yields better residual stress prediction than the existing one.

Table 2.3 Results of maximum deformation in the Z-direction

	Max. deformation in Z-dir.	Error
Detailed process simulation	6.477 mm	N/A
MIS-based simulation - existing	6.660 mm	2.8%
MIS-based simulation - new	6.244 mm	-3.6%

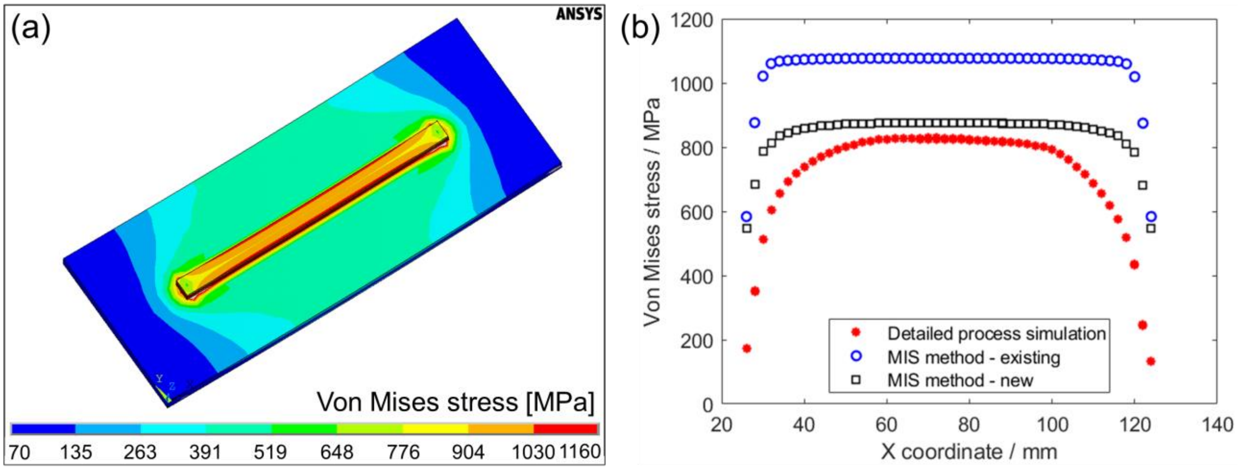

Figure 2.11 (a) Von Mises stress of the MIS-based simulation using the new procedure; (b) comparison of von Mises stress along the top centerline of the single-walled deposition in different simulations.

2.4 Experimental Validation

This section will experimentally validate the new procedure by evaluating the residual deformation and stress for two structures fabricated by L-PBF (EOS M290 DMLS in the present work). The first structure is a solid L-bracket printed in stainless steel 316L and 17-4PH. The second one is a canonical part printed in 316L. The distortion of the as-built specimen is measured by a Faro Arm scanning device, and the residual stress is measured by X-ray diffraction (XRD). Note that the distortion of the L-bracket is not investigated here because its superficial normal shrinkage is minimal, and the magnitude is close to the measurement resolution of the device (approximately 0.075-0.1 mm [52]). As a reference, the ANSYS AM package (AdditiveWizard) is also employed to predict the residual deformation and stress. This package uses a layer-wise thermomechanical analysis. The specific computational principles of this package are proprietary and thus are not accessible by common users including the authors.

2.4.1 Material Properties of 316L and 17-4PH

The temperature-dependent material properties of 316L and 17-4PH shown in the Appendix are obtained from the references [71, 74-76]. Before implementing the MIS method, we need to ensure these properties are consistent with those samples produced by the EOS M290. Therefore, some 316L and 17-4PH tensile bars are built using the default process parameters provided by the printer, and tested according to ASTM E8/E8M Standard [77]. Due to equipment limitation, only room-temperature mechanical properties are measured. The results of Young's modulus and yield strength are close to those from the literature [71, 75] (Table 2.4). Similar values are also reported by the EOS company [78]. It indicates that samples printed in the present work possess properties at room temperature similar to those found in the literature. Therefore, the full-range temperature-dependent material properties (see Appendix) found in the literature are considered acceptable and thus adopted in our simulations.

Table 2.4 Mechanical properties (at room temperature) of 316L and 17-4PH

		316L	17-4PH
Young’s modulus (GPa)	Tensile test	250 ± 6	235 ± 18
	Literature [71, 75]	196	205
Yield strength (MPa)	Tensile test	520 ± 11	1040 ± 82
	Literature [71, 75]	428	1158

For 316L and 17-4PH, the solid-state phase transformation, such as austenite-to-martensite transformation, is ignored based on two considerations. First, although some material models [79, 80] can include the solid-state phase transformation, their use is limited due to the lack of modeling parameters, which are usually material-dependent and need special experiments to determine. Second, in the research by Li et al. [71], for 316L parts fabricated by the L-PBF process, the residual stress predicted by the numerical simulation agrees well with the experimental measurement without considering the solid-state phase transformation. It means that for materials like 316L, the solid-state phase transformation has a limited effect on residual stress.

2.4.2 Heat Source Calibration

Default process parameters for 316L and 17-4PH powder in EOS M290 DMLS printer are given in Table 2.5. Among them, hatch spacing, stripe width, and stripe overlap are related to scanning strategies and illustrated in Figure 2.12. The direction of the scanning path is rotated layer-by-layer to minimize the material’s anisotropy.

Table 2.5 Default L-PBF process parameters for 316L and 17-4PH in EOS M290

	316L	17-4PH
Laser power	195 W	195 W
Scanning velocity	1083 mm/s	900 mm/s
Layer thickness	20 μm	20 μm
Hatch spacing	90 μm	90 μm
Stripe width	5 mm	4 mm
Stripe overlap	0.12 mm	0.7 mm
Laser rotation angle	66.7°	66.7°

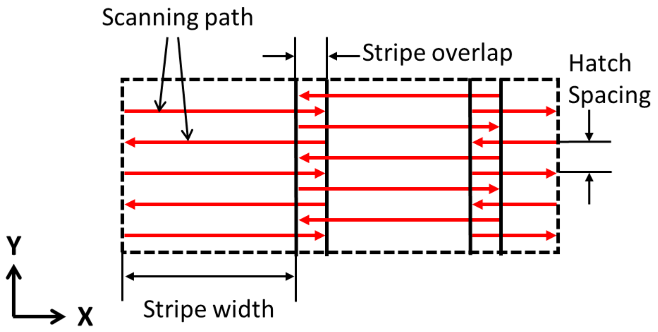

Figure 2.12 Process parameters related to laser scanning strategy (X-Y plane is the in-layer plane, build direction is along the Z-axis which is in the out-of-layer plane).

The heat source model employed in the detailed process simulation is similar to the one shown in Figure 2.5(b) using different parameter values. Geometrical (a, b, c) and energy-related (Q) parameters are calibrated experimentally by single-layer deposition on a substrate made of the same material (see Figure 2.13). The thickness of the deposition is close to the layer thickness of the L-PBF process. Four corners of the substrate are fixed to the native build platform. A thermocouple (Omega SA1XL-K-72) is attached to the bottom of the substrate beneath the deposition to collect temperature data. According to our experience, a single-layer deposition can hardly cause remarkable temperature change at the bottom of a substrate nearly 10 mm thick. Therefore, three grooves (35 mm in length, 10 mm in width, and 6.35 mm in depth) are created by milling the back of the substrate to attach the thermocouples closer to the laser scanning surface. This kind of far-field temperature measurement has been widely used in metal welding and AM fields to validate the process model [33, 56, 63, 81]. After printing, a small piece of the single-layer deposition and substrate is cut off by electrical discharging machining (EDM) and chemically etched for molten pool measurement using an optical microscope. The width and depth of the heat source are straightforwardly determined based on the measured melt pool cross-section. The half-length of the heat source is assumed to be equal to its half-width, that is, $a = b$ [49]. The calibration procedures are detailed in Ref. [49] and are not described here. Through calibration, the temperature history of the measured location from the simulation is in good agreement with the experimental data, as shown in Figure 2.14. Table 2.6 summarizes the calibrated heat source parameters.

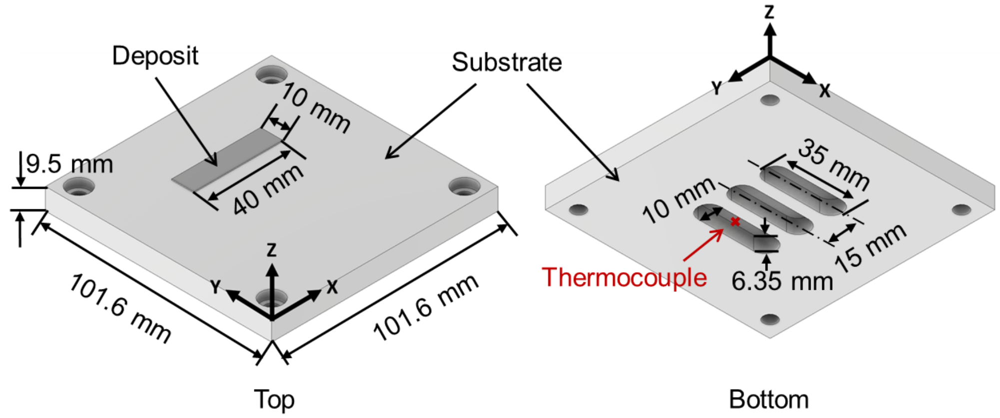

Figure 2.13 Geometrical dimension of the single-layer deposit and the substrate with grooves.

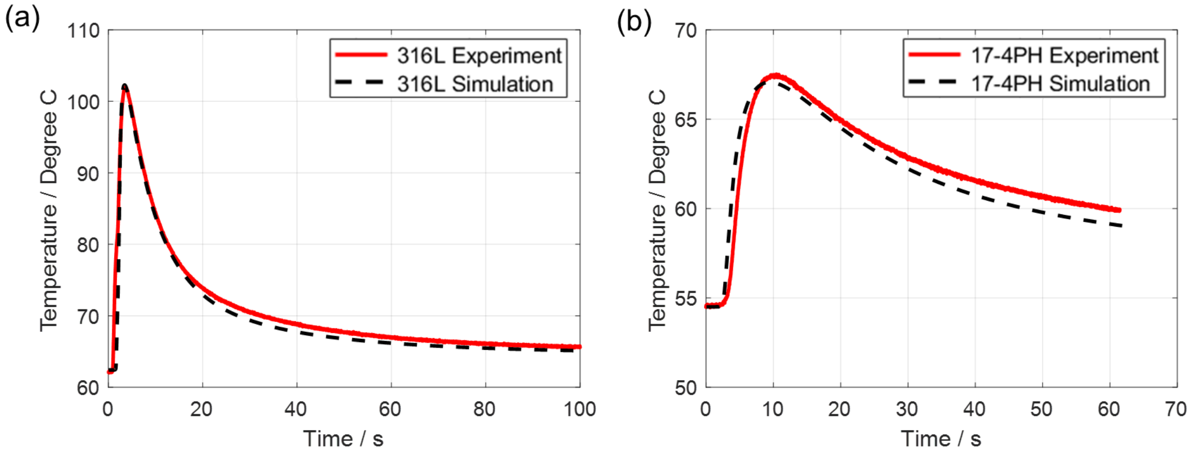

Figure 2.14 Comparison of the simulation and experimental results for the single-layer deposition made of (a) 316L and (b) 17-4PH.

Table 2.6 Calibrated parameters of the Goldak heat source model

	316L	17-4PH
Half-length $a = a_f = a_r$	60.5 μm	30.9 μm
Half-width b	60.5 μm	30.9 μm
Depth c	50.4 μm	32.1 μm
Effective power Q	87.75 W	58.50 W

2.4.3 Extraction of Inherent Strains

The calibrated heat source model is then employed in the detailed process simulation, which consists of a five-layer deposit on a previously deposited block, as shown in Figure 2.15. The FE mesh comprises two different shapes. The deposit and the surrounding pre-deposited block are meshed with 8-node hexahedral elements. The remaining section of the model is filled with elements of mixed types by free meshing in order to reduce computational time. The elements in the deposit have a uniform size of 12 μm × 12 μm × 6.7 μm. Considering the laser beam spot radius is around 50 μm, this element size is able to provide enough simulation accuracy. The rotational angle of laser scanning paths is set to 90° between two consecutive layers. Specifically, the 1st, 3rd, and 5th layers are scanned along the X-direction, while the 2nd and 4th layers are scanned along the Y-direction (coordinate directions are denoted in Figure 2.15). Here, we choose a rotational angle of 90° instead of the default 66.7° because the former requires fewer layers to let the scanning direction rotate back. The influence of the rotational angle will be discussed in the next section. There is a dwell time of 20 seconds between two consecutive layers, accounting for operations like build plate descend and powder spreading [49].

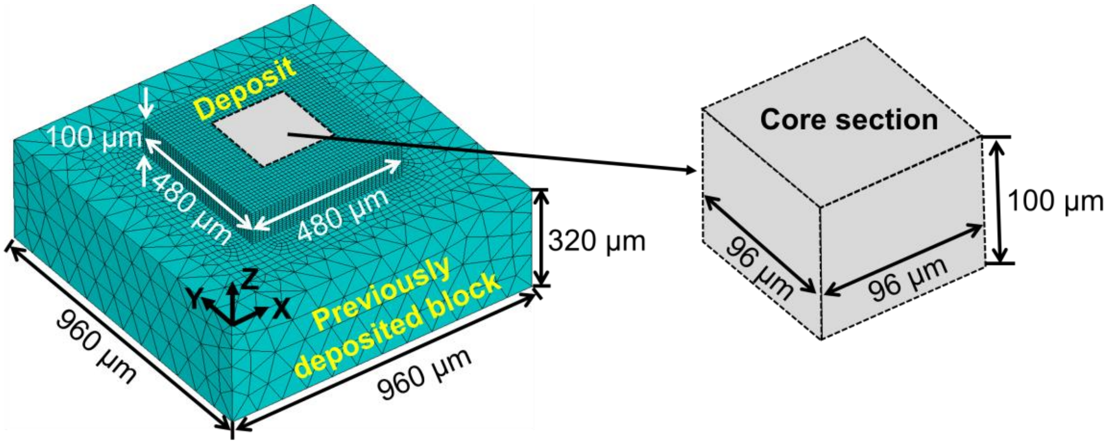

Figure 2.15 Geometry of the model for detailed process simulation.

The detailed simulation and the extraction of ISs on this mesoscale FE model follow the general procedures described in Section 2.1.3. Heat convection and radiation are applied to the outer surface of the model. The convection coefficient and emissivity are constant for most of the outer surface. However, these parameters should be considered temperature-dependent for areas near the heat source due to the extremely high temperature to ensure accuracy [82, 83]. An empirical relationship [84] is employed to determine the convection coefficient on the top surface of the layer that is being deposited:

$$h_a = 2.4 \times 10^{-3} \varepsilon T^{1.61} \tag{2.12}$$

where h_a denotes the artificial convection coefficient ($\mathrm{W \cdot m^{-2} K^{-1}}$), ε is the emissivity coefficient, and T is the material temperature in Kelvin (K). This artificial coefficient combines the influence of both temperature-dependent convection coefficient and emissivity.

During the printing, the stress and strain evolution of the deposited material is affected by its transient temperature field from two aspects: (1) thermal strain and (2) temperature-dependent material properties. To illustrate, we select a measuring path at the bottom of the 316L deposition (see the dashed line in Figure 2.16) and compare the stress and temperature values along this path when each layer is complete ($t_1 \sim t_5$) and when the steady state is reached (t_s), as shown in Figure 2.17. Here, the term "complete" means the laser finishes scanning the entire layer, not including the interlayer cooling process. Note that the laser scanning paths are parallel to the X-direction in Layer 1, 3, and 5, and are parallel to the Y-direction in Layer 2 and 4.

In Figure 2.17(a), the average temperatures along the measuring path at t_1 and t_3 are higher than t_5, indicating that the effect of thermal expansion at t_1 and t_3 is supposed to be larger than t_5. However, this effect is limited since the material properties like yield strength and Young's modulus at high temperatures are quite small. This explains why (1) the X-directional stress is tensile at t_1 and t_3 and compressive at t_5; (2) the stress magnitude at t_1 and t_3 is significantly smaller than that at t_5. A similar trend is also observed in Figure 2.17(b), where the magnitude of stress at t_4 is larger than that at t_2 even though the latter has a higher temperature profile. When the deposition cools down to ambient temperature (steady state t_s), the residual stress in the X-direction along the measuring path becomes highly tensile due to thermal contraction, which is consistent with the results in Ref. [85]. The two ends of the path have larger stress values than the center, which is caused by the constraint of the previously deposited block. Note that the temperature profile is almost symmetrical at t_1, t_3, and t_5, while asymmetrical at t_2 and t_4. This is caused by the rotation of laser scanning paths.

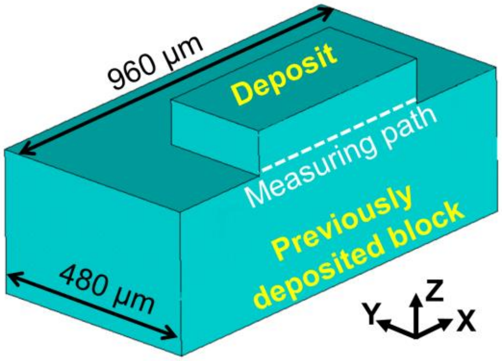

Figure 2.16 Measuring path along which temperature and stress are extracted.

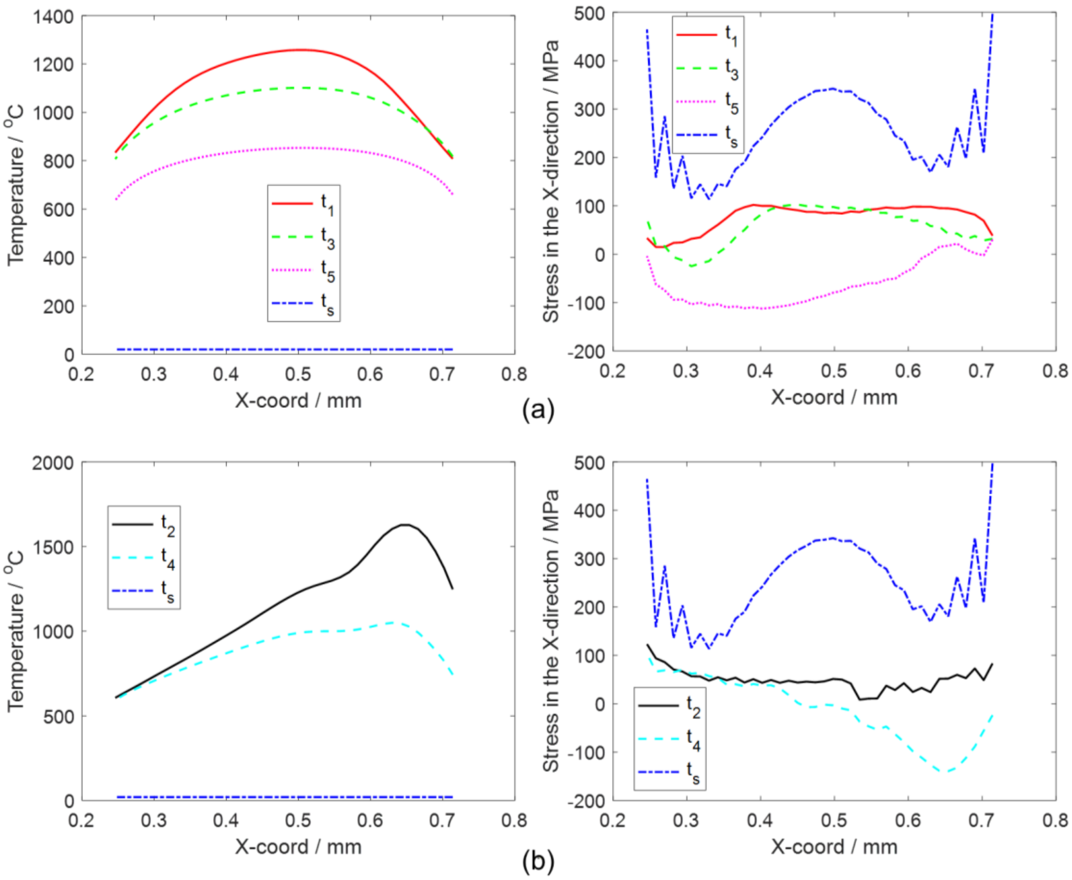

Figure 2.17 Variation in temperature (left) and X-directional stress (right) along the measuring path at (a) t_1, t_3, and t_5, and t_s; (b) t_2, t_4, and t_s. "t_N" represents the time when Layer N is complete. "t_s" represents the steady state.

When the detailed process simulation is done, ISs in three normal directions (X, Y, and Z) are extracted. We only consider those elements located in a core section (96×96×100 μm^3) of the deposit, as shown in Figure 2.15, to minimize the influence of boundary constraints. The averaged ISs for each layer are plotted in Figure 2.18. As can be seen, the in-layer-plane ISs (along the X- and Y-direction) are compressive, while the out-of-layer-plane components (along the Z-direction) are tensile. The IS in the X- and Y-direction fluctuate slightly for different layers. That is caused by the 90° rotation of the scanning paths in the detailed process simulation. The fluctuation indicates that the magnitude of IS in the laser scanning direction is slightly smaller than in the transverse (to the scanning path) direction. It also suggests that the obtained ISs can capture the influence of the scanning direction. Setien et al. [45] have shown that when the laser scanning path rotates periodically, the in-layer ISs tend to be uniform no matter what the specific rotation angle is. Therefore, in this study, according to research conducted by Xuan et al. [51], we average ISs in the X- and Y-direction to obtain a uniform value for the in-layer plane. This value is also applicable for parts printed with other rotation angles. Note that in cases where the laser path does not rotate cyclically, such as using a fixed direction, the IS components along the scanning and transverse directions are set differently and cannot be averaged [52]. To consider the inter-layer effect, ISs in different layers are further averaged. The final IS vectors adopted in the following MIS-based simulations are listed in Table 2.7.

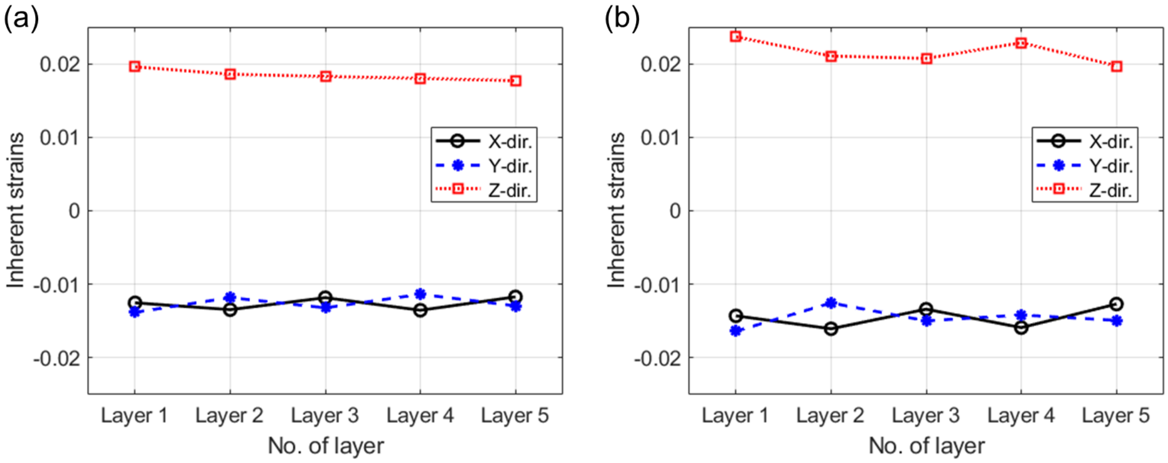

Figure 2.18 Average ISs for each layer of the five-layer deposition for (a) 316L and (b) 17-4PH.

Table 2.7 ISs for 316L and 17-4PH in L-PBF process

	In-layer plane (X-direction)	In-layer plane (Y-direction)	Out-of-layer plane (Z-direction)
316L	-0.0126	-0.0126	0.0183
17-4PH	-0.0145	-0.0145	0.0216

2.4.4 MIS-based Simulation on L-bracket

The ISs in Table 2.7 are applied to the L-bracket deposition using both the existing and new procedures for comparison. When implementing the MIS-based simulation, the L-bracket with nearly 1,400 physical thin layers is divided into 40 equivalent layers in the build direction. The number of equivalent layers is determined based on the research conducted by Xuan et al. [48] and Qian et al. [49]. They employed the MIS method to predict the residual distortion of a DMLS-processed canonical part in which one equivalent layer represents 36 physical layers. Here, the L-bracket has 40 equivalent layers, each containing 35 physical layers. Interested readers are referred to Ref. [48] for more details about how the number of equivalent layers would affect the accuracy of the MIS method. The predicted residual stress on top of the deposit is compared with XRD measurements. The geometry of the L-bracket and residual stress sampling points (P1 to P15) are given in Figure 2.19(a). Two specimens are printed for each material using different laser scanning strategies, as shown in Figure 2.19(b). One strategy has a layer-wise rotation angle of 90° (denoted by ALT), while the other is 66.7° (denoted by ROT). Figure 2.19(c) shows an as-built L-bracket printed with 316L. The XRD measurement is done by American Stress Technologies Inc. with the Stresstech Xstress 3000 Xrobot (Figure 2.19(d)). The deviation of the measured residual stress (error bars in Figure 2.21) represents the quality of the elliptical curvature fitting of d and $\sin^2\psi$, where d is the interplanar spacing, and ψ is the title angle that defines the orientation of the sample surface [53, 86]. The residual stress is calculated based on a series of interplanar spacing measurements at different title angles. Besides, as reported in Ref. [87], the oxidation on the sample surface may also cause the deviation. But this is difficult to quantify. For interested readers, more information regarding the residual stress measurement by the XRD technique can be found in Ref. [53].

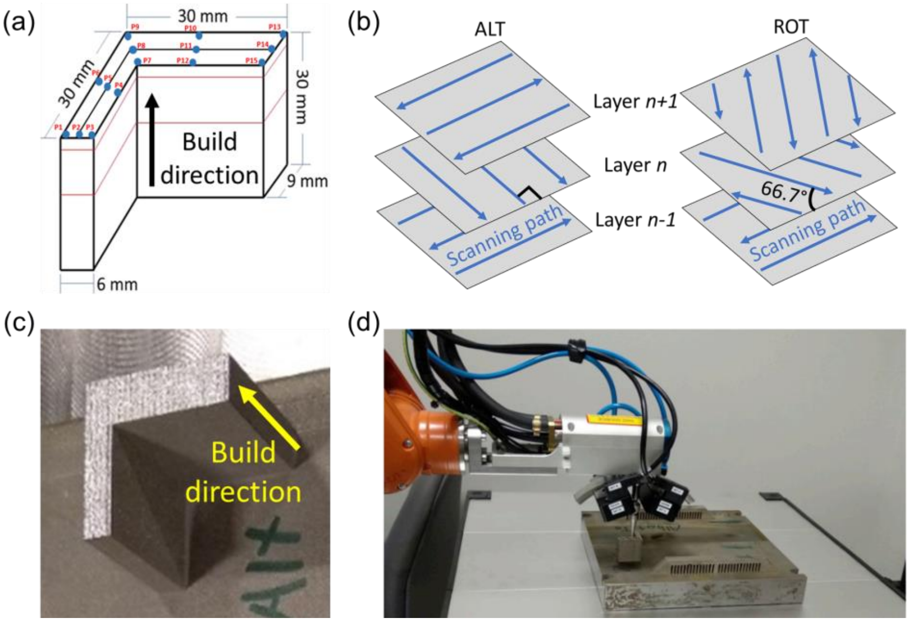

Figure 2.19 (a) Geometry of the L-bracket; (b) two laser scanning strategies; (c) as-built L-bracket; (d) residual stress measurement setup [53].

Theoretically, the top surface of the L-bracket has no stress in the Z-direction (build direction) because it is a free surface. Therefore, the XRD measurement on the top surface is acceptable, even though it can only acquire in-plane residual stress, that is, the stress in the X- and Y-directions. However, due to numerical errors caused by the Gaussian integration and the extrapolation of results, the Z-directional stress on the top surface is not exactly zero in the simulation. Figure 2.20(a) and (b) show the von Mises and Z-directional stress of the 316L L-bracket using the new procedure. On the top surface, the average von Mises stress is around 170 MPa, and the average Z-directional stress is about 6 MPa. Given that the stress in the Z-direction only accounts for insignificant influence on the von Mises stress, in the following section, we directly compare the von Mises stress obtained from the XRD measurement, MIS-based and ANSYS AM simulations.

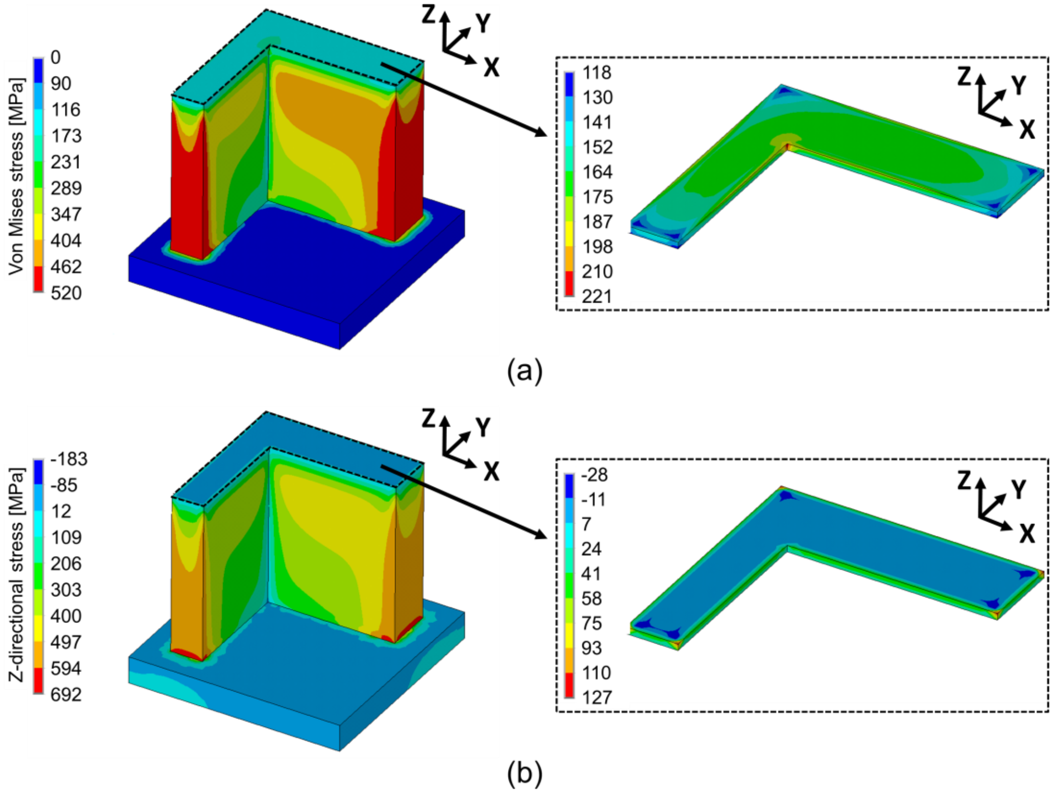

Figure 2.20 (a) Von Mises stress and (b) Z-directional stress of the L-bracket deposit.

Figure 2.21 shows the residual stress at different measurement locations. The exact stress values can be found in the Appendix. The legend is explained as follows. “ANSYS AM” represents results obtained by the ANSYS AM package. “MIS-EXT” and “MIS-NEW” denote simulation results obtained using the existing and new procedures of the MIS method, respectively. “EXP-ALT” and “EXP-ROT” denote experimental results for the ALT and ROT specimens, respectively.

As mentioned before, it has been proved that the cyclical rotation scanning strategies tend to cause homogeneous ISs in the printing plane and thereby resulting in similar residual stress and deformation fields under different rotation angles. In Figure 2.21, for both materials, the experimental measurements of ALT and ROT specimens show a fair agreement considering the experimental uncertainties, meaning that the effect of different rotation strategies on the residual stress is small. However, at sharp corners such as P1 for 316L and P9 for 17-4PH, the ALT has extremely low residual stress than ROT, indicating that drastic changes in geometry or boundary conditions may enhance the effect of rotation strategies on the residual stress. The influence of geometric changes on the residual stress can also be observed in the results of numerical simulations (ANSYS AM, MIS-EXT, and MIS-NEW). For example, for both ends of the top surface (P1-P2-P3 and P13-P14-P15), the predicted residual stress computed at the midpoints (P2 and P14) is larger than those at the corner. This is because the midpoints have less freedom to deform.

It can be seen from Figure 2.21 that for most of the inspection points, the existing procedure significantly overestimates the residual stress values (close to the yield strength of the material) compared to XRD measurements. In contrast, the proposed new procedure can provide residual stress much closer to the experimental results for both materials. Further, even for the corner points where the measured stress in the ALT specimen largely differs from the ROT, such as P1 for 316L and P9 for 17-4PH, the residual stress predicted by the new procedure is reasonable as it is between EXP-ROT and EXP-ALT values. In general, the residual stress predicted by ANSYS AM is close to the results of the new procedure and experiment, further validating the new procedure. The performance of ANSYS AM is not evaluated here as it is beyond the scope of this research. This package does not seem to consider the effect of laser scanning strategies because the related parameters, such as rotational angle, are not needed when setting up the model.

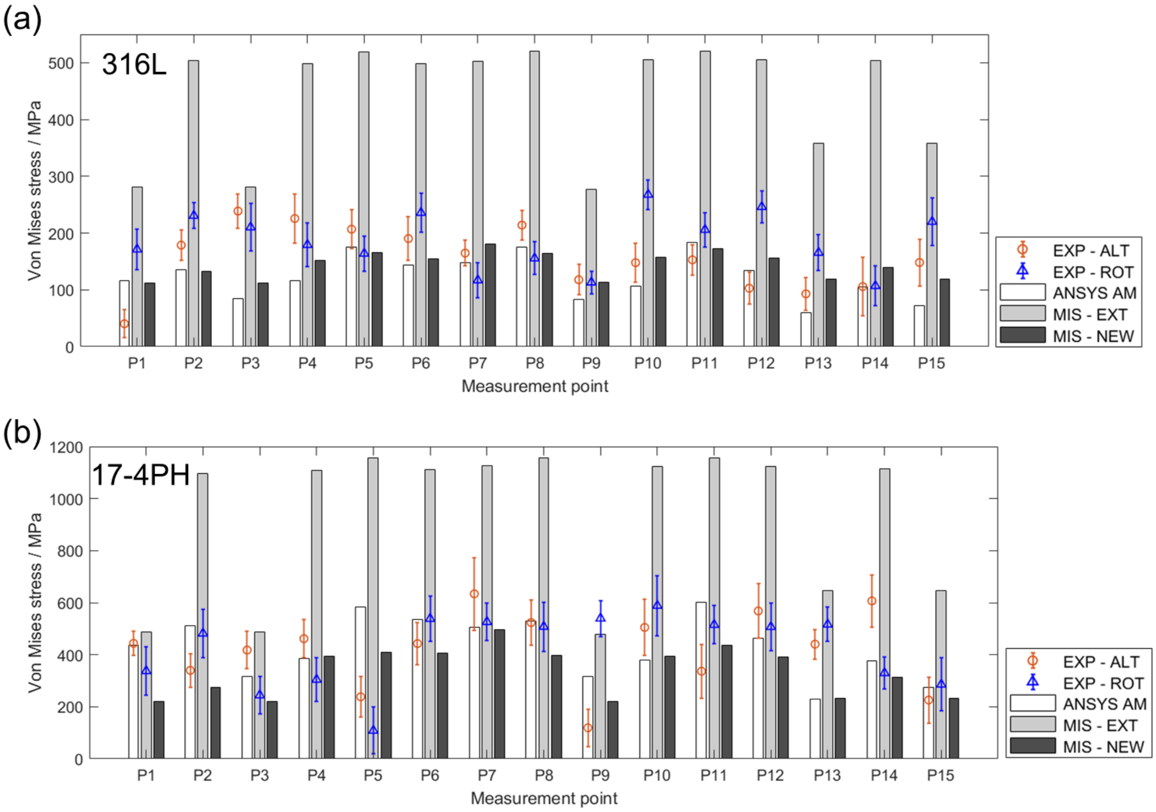

Figure 2.21 Von Mises stress obtained by simulations and measurement at different locations on the top surface of the L-bracket with (a) 316L; (b) 17-4PH.

In addition to the residual stress on the top surface, we also investigate the normal stress distribution along the build direction. As shown in Figure 2.22(a), two measuring paths on a section plane are selected. Path A is on the sidewall of the L-bracket, while Path B is located inside. Figure 2.22(c) and (d) show the normal stress (σ_y and σ_z) along these two paths and compare the results from MIS-NEW and ANSYS AM. Note that the stress profiles (1) have similar trends for 316L and 17-4PH only with different magnitudes, and (2) have a good agreement between MIS-NEW and ANSYS AM in general. Therefore, for convenience, the following discussion regarding the stress profiles focuses on the results obtained by MIS-NEW with 316L. Along Path A, the tensile stress σ_y in the top and bottom area of the L-bracket is higher than in the center area. This is because, along the build direction, the in-layer-plane thermal contraction at two ends is larger than in the middle of the part [48]. The Z-component normal stress σ_z is also tensile along Path A. It first increases with the part height because the thermal contraction in the Z-direction accumulates and then vanishes rapidly due to the free surface on top of the part. These stress variations on the sidewall of the L-bracket are consistent with the XRD results in Ref. [87]. Along Path B, σ_y has a similar pattern to that along Path A though the stress values are smaller. σ_z varies from highly compressive on the substrate (Z = 0) all the way up to nearly zero on the top surface (Z = 30 mm). Li et al. [71] also reported this compressive σ_z in the center of the L-bracket and stated that it is balanced by the tensile σ_z on the sidewall.

It has to be noted that the results predicted by MIS-NEW and ANSYS AM show a relatively large discrepancy at the bottom of the part, especially on Path A. This may be caused by the FE mesh associated with the contact algorithm that ANSYS AM uses between the part and substrate. As shown in Figure 2.22(b), although a uniform mesh size is intentionally chosen for the entire structure in ANSYS AM, the auto-generated meshes in the deposit and the substrate still have a mismatch. The contact algorithm that ANSYS AM employs aims to allow users to use fewer elements in the substrate and save computational time but may also lead to inaccurate results at the interface of mismatched meshes.

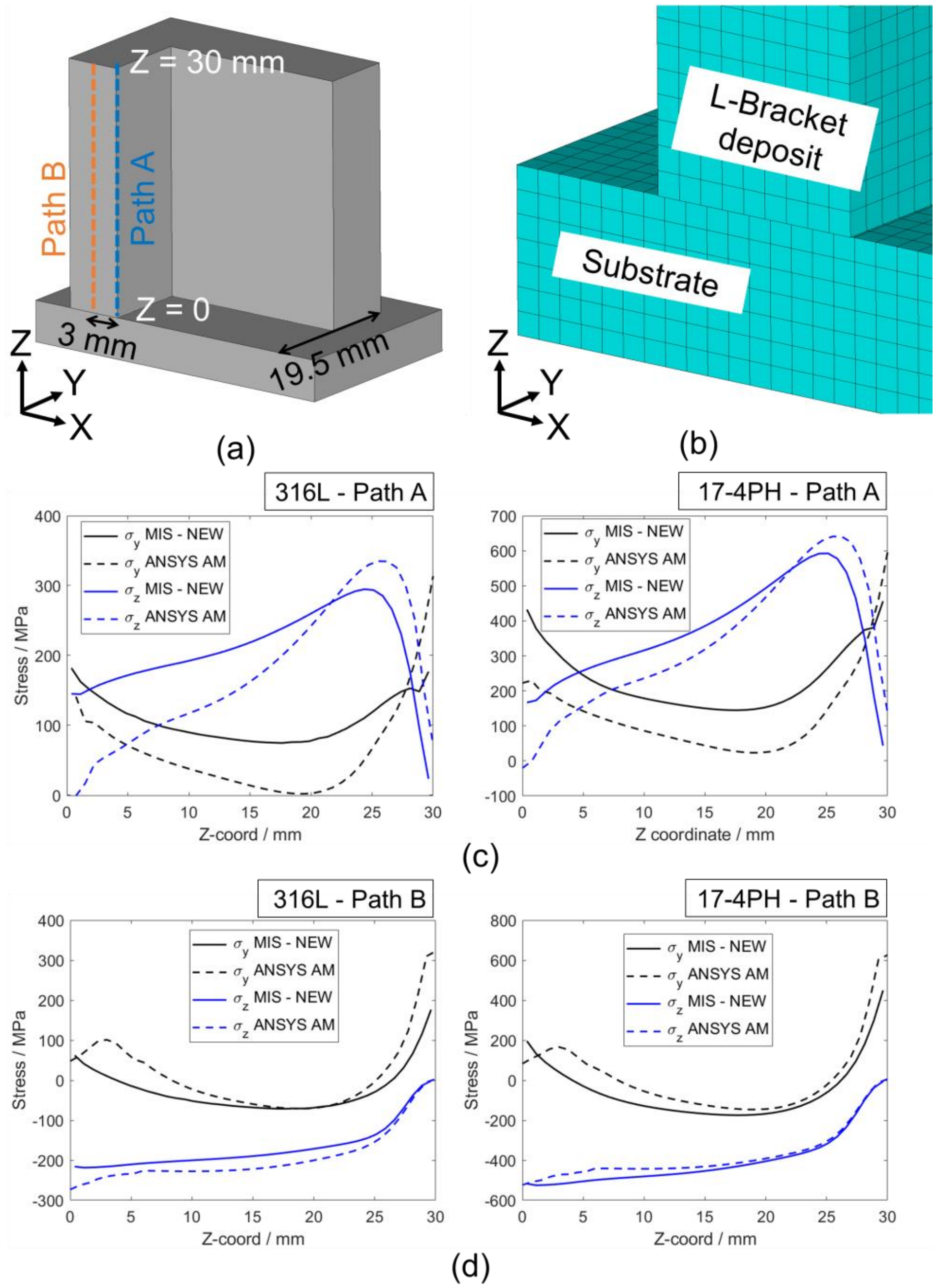

Figure 2.22 (a) Locations of measuring Path A and B; (b) FE mesh mismatch in ANSYS AM; (c) residual stress distribution along Path A for 316L (left) and 17-4PH (right); (d) residual stress distribution along Path B for 316L (left) and 17-4PH (right).

2.4.5 MIS-based Simulation on Canonical Part

In this section, the new MIS procedure is employed to evaluate both residual deformation and stress of a canonical part fabricated by EOS M290 DMLS in 316L by default parameters. As shown in Figure 2.23(a), two identical specimens are printed, each with an overall dimension of 81.6 × 81.6 × 64.5 mm^3. Due to the symmetry, the MIS-based simulations are implemented using a quarter FE model (see Figure 2.23(b)). Details regarding the modeling of this canonical part can be found in our previous works [48, 49], where the existing MIS procedure is implemented to the same part made of Inconel 718 and Ti-6Al-4V. After the simulation (ANSYS AM, MIS-EXT, MIS-NEW) and experiment (EXP), total distortion is measured on the outer surface of the part along the paths shown in Figure 2.23(a).

The results are plotted in Figure 2.24. The curve EXP-AVE is the experimental data averaged over eight measuring paths (each specimen has four), and the shaded area EXP-STD represents the standard deviation of the measurement. The negative distortion values indicate part shrinkage. It can be seen that the distortion along the build direction is not uniform, which is mainly caused by the irregular geometry of the canonical part. The measured distortion can be approximately divided into four regions along the build direction, as shown in Figure 2.24. In Region A, the substrate has strong constraints on the deposited material. As the part height increases, the constraints become weaker, leading to increased distortion. In Region B, the distortion is stable because the influence of the substrate is limited, and the part geometry is regular in that region. In Region C, the distortion significantly increases with part height and reaches a peak value due to the presence of the overhanging inner wall and its varying cross-sectional area with height. Note that the inner wall and outer wall of the part become connected in this region, forming a strong constraint on the deposit. In Region D, the distortion decreases as the measuring position approaches the top free surface. Overall, all the numerical methods are able to capture this trend.

Regarding the prediction by the MIS models, the distortion predicted in Region B by MIS-NEW and MIS-EXT are larger than the experimental measurement. A possible reason for this discrepancy is that the ISs we use are extracted from bulk deposits, which may not be accurate for thin-walled structures in Region B. The distortion comparison between the MIS-NEW and MIS-EXT indicates that although the new procedure aims only to adjust the ratio of elastic strain to plastic strain, it still affects the total strain and distortion. In addition, the prediction of MIS-NEW in Region B and C has a larger error than that of MIS-EXT. This is likely because, compared with the existing procedure, the material change process in the new procedure adds complexity to the strain evolution, making the new procedure more sensitive to extreme geometries (thin-wall in Region B) and drastic geometrical changes (in Region C). This topic is left for future study.

Although able to follow the distortion trend, the ANSYS AM overestimates the distortion along the entire measuring path compared with the measurement. However, the prediction errors are comparable with the experimental errors. The latter may be induced by the limited resolution of the device (approximately 0.075-0.1 mm [24]) and the alignment algorithm used to compare the CAD file and scanned point cloud. Note that the height (Z-coordinate) of the peak distortion in Region C predicted by the numerical methods is slightly different from the experiment. This is because the equivalent layer used in these numerical methods is thicker than the actual layer, making it challenging to capture the exact location of the peak distortion. In general, the MIS method with the new procedure can effectively predict the residual deformation of AM parts processed by L-PBF.

Similar to the L-bracket, residual stresses at several locations on top of the canonical part, as shown in Figure 2.25(a), are measured via XRD and compared with the predictions by numerical methods. P1, P5 and P9 are located at the very top of the structure (on the fence), while other points are on the top flat plane of the structure. From the top view, these points are distributed on three lines. Line P1-P4 and Line P5-P8 are perpendicular and form a 45° angle with Line P9-P12. The comparison of the residual stress is shown in Figure 2.25(b), where the legend is similar to that for the L-bracket. "EXP-1" and "EXP-2" represent the measured data from different specimens. The exact stress values can be found in the Appendix. In Figure 2.25(b), the existing procedure of the MIS method again severely overestimates the residual stress, while the new procedure and ANSYS AM yield results closer to the measurement.

In addition to the stress values, the numerical simulations exhibit some stress patterns confirmed by the experiment. The residual stress on the fence (P1, P5, and P9) is higher than on the flat plane. The stress distributions on Line P1-P4 and P5-P8 are similar, which is reasonable because the part is symmetric. In addition, it is found that, on the flat plane, the point closer to the part center tends to have higher residual stress. For instance, P4 > P3 > P2. This may be related to the irregular geometry of the canonical part.

To this end, the effectiveness of the new procedure has been fully validated. Employing both material properties corresponding to the intermediate and steady thermal state can improve the performance of MIS-based simulation for residual stress prediction while retaining accuracy in deformation prediction.

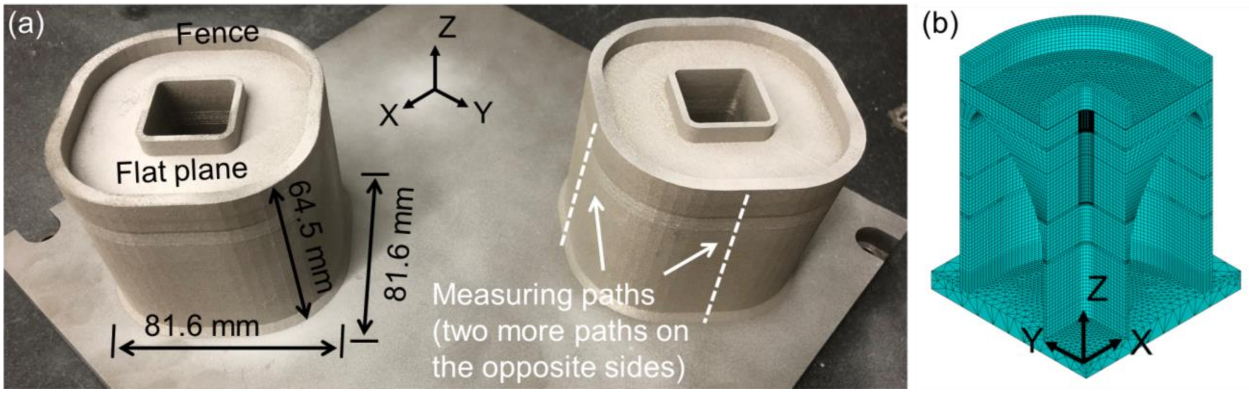

Figure 2.23 Canonical part: (a) printed specimens and (b) one-quarter FE mesh.

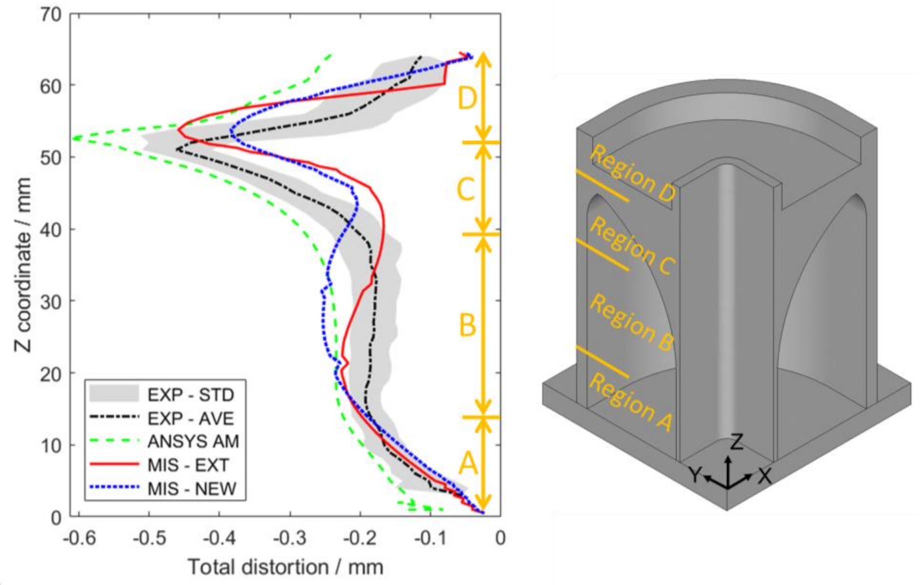

Figure 2.24 Total distortion along the measuring path.

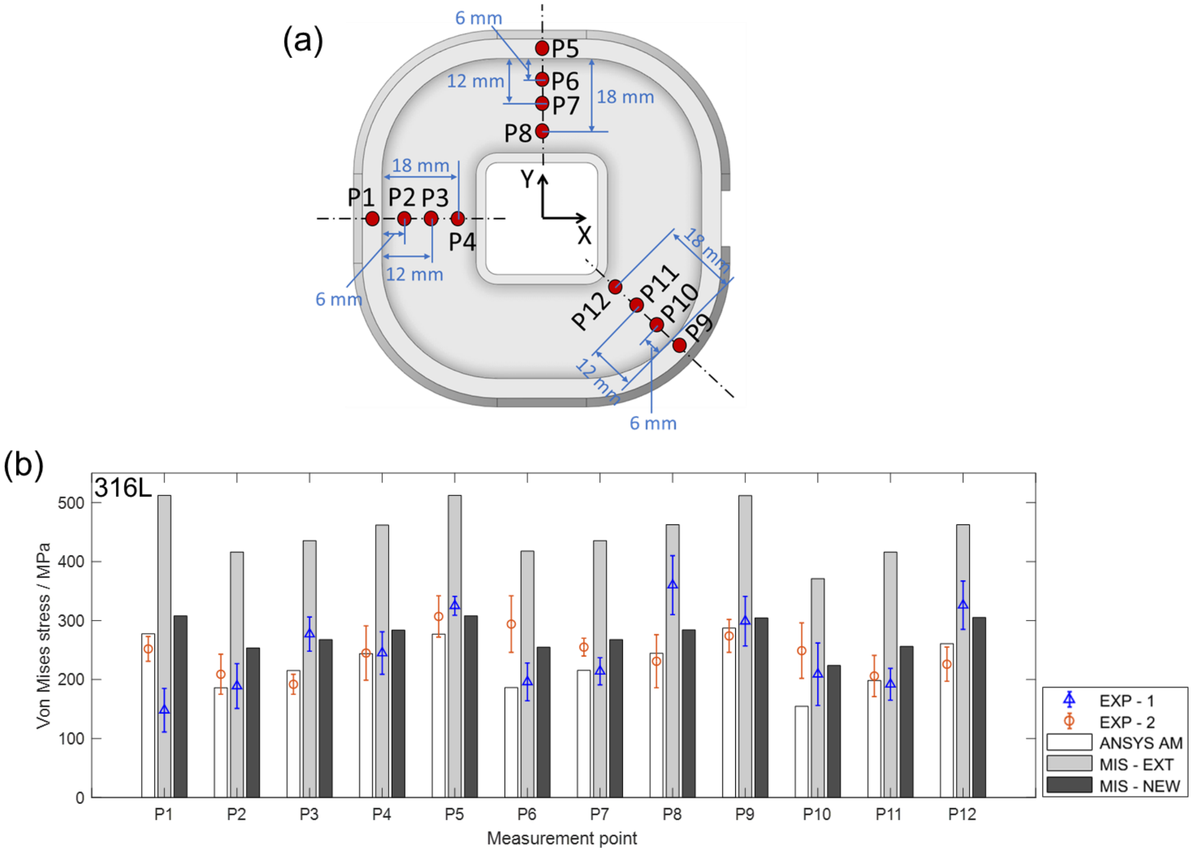

Figure 2.25 (a) Location of measurement points P1 - P12 and (b) von Mises stress comparison.

2.5 Conclusions

Though exhibiting good accuracy in predicting residual deformation, the MIS method has not been fully investigated for its performance in residual stress evaluation. In this chapter, we use a three-layer single-walled deposit to numerically demonstrate the existing implementation procedure of the MIS method is not able to predict the residual stress of metal builds accurately. In particular, the residual stress level is overestimated. After carefully inspecting the workflow of the MIS method, the way of extracting ISs through the detailed process simulation is considered reasonable, but the implementation procedure of the MIS-based part-scale simulation is found to be flawed. The existing procedure applies ISs to the deposit with only ambient temperature properties. However, accurate ISs are calculated based on two terms: one is generated at high temperature (intermediate term), while the other is induced when the high temperature changes to the ambient temperature (steady term). It suggests that the ISs depend on material properties not only at ambient temperature but also at the elevated temperature corresponding to the intermediate state. Therefore, only employing material properties at ambient temperature in the MIS-based simulation is inaccurate.

To improve the modeling fidelity, a new procedure for implementing the MIS-based simulation is developed in this chapter. Unlike the existing one, the newly proposed procedure considers material properties at temperatures corresponding to both intermediate and steady states. The effectiveness of the new procedure is then experimentally validated by L-brackets and canonical parts printed by EOS M290. For the L-bracket, the von Mises stress extracted from the MIS-based simulation is compared with the XRD and ANSYS AM results at several locations on top of the part. For the canonical part, in addition to the stress comparison, the distortion is also measured and compared with the scanning and ANSYS AM data. The results obtained by the new procedure match the experiment well. In particular, the new procedure significantly improves the accuracy of residual stress prediction compared to the existing procedure.

3.0 Temperature-dependent Modified Inherent Strain (MIS) Method for Predicting Residual Stress and Distortion for Wire-arc DED

3.1 Effect of Heat Accumulation in Wire-arc DED

Compared to L-PBF, the wire-arc DED is more prone to heat accumulation due to its high deposition rate combined with low heat dissipation during the deposition [7, 8, 88, 89]. Heat accumulation is commonly quantitatively evaluated by the interpass temperature, which refers to the temperature on top of the previous layer right before the deposition of new material. In other words, the more heat accumulates, the higher the interpass temperature. Literature has revealed that heat accumulation is crucial for the wire-arc DED process. Wu et al. [90] found that the interpass temperature is able to change the arc shape and deposit geometry in the wire-arc DED process with Ti6Al4V. They suggested that the interpass temperature should be precisely controlled during the deposition for better product quality. Vázquez et al. [91] investigated the influence of heat accumulation on the mechanical properties and microstructure of Ti6Al4V alloys manufactured by wire-arc DED and stated that reducing interpass temperature can avoid the coarsening of α_{GB} and increase the elongation at break. Jimenez et al. [92] and Silva et al. [88] reported that severe heat accumulation leads to significant residual stress and distortion. Xiong et al. [93] showed that a lower interpass temperature is beneficial to increasing the surface quality of thin-walled parts fabricated by wire-arc DED. Many measures have been proposed to reduce heat accumulation, such as implementing active cooling systems [8, 88, 91], combining with conventional manufacturing processes like forge [94], and adjusting process parameters and deposition strategies [93, 95]. Lee et al. [96] investigated the influence of interpass cooling time, constraint condition, and toolpath strategy on the deformation of Ti6Al4V walls.

Despite the application of the MIS method in the L-PBF process, to the best of our knowledge, its application to the wire-arc DED process has not yet been explored. A vital limitation of the current MIS method is its inability to account for the effects of heat accumulation. To overcome this, we extend the current MIS method to make it suitable for predicting residual stress and deformation in wire-arc DED processes.

3.2 Extension of the MIS Method

The MIS method has been proved effective for AM processes like L-PBF with relatively small parts [48, 49, 51, 52, 59]. However, when this method is used to predict the residual stress and distortion of large parts produced by wire-arc DED, the prediction error may increase due to the significant heat accumulation. The error mainly comes from two aspects: (1) the small representative FE model in the detailed process simulation is not able to reflect the heat transfer within the large part; (2) applying constant ISs in the MIS-based simulation ignores the fact that the interpass temperature is not constant due to heat accumulation.

To improve the prediction accuracy for wire-arc DED processes, we extend the current MIS method and introduce the concept of temperature-dependent ISs, that is, the ISs applied to a deposit volume depend on the interpass temperature of the deposit. The general procedures of the extended method are shown in Figure 3.1. The main differences between the constant and temperature-dependent MIS methods are:

(1) The detailed process simulation is implemented not once but several times with different temperatures applied to the previously deposited block (see Figure 3.1 top-left) as thermal boundary conditions to include the effect of interpass temperature. An IS versus interpass temperature relationship is established after simulations.

(2) After the detailed process simulation, a step of implementing the flash heating simulation is added, aiming to obtain the interpass temperatures for a given part. The newly added simulation uses the same part-scale FE model as the MIS-based simulation but involves transient thermal analysis with an equivalent heat source. Details regarding this type of simulation will be discussed later.

(3) For the MIS-based simulation, different ISs are applied according to the interpass temperatures obtained by the flash heating simulation. The two-equilibrium procedure is unchanged. Note that the dependence of material properties on the interpass temperature is not directly considered in the MIS-based simulation because it is accounted for in the detailed process simulation and implicitly included in the IS values.

(4) In the FE model for flash heating and MIS-based simulations, each layer is divided into several segments to apply the equivalent heat source and ISs. The actual scan pattern of the heat source is ignored in each segment.

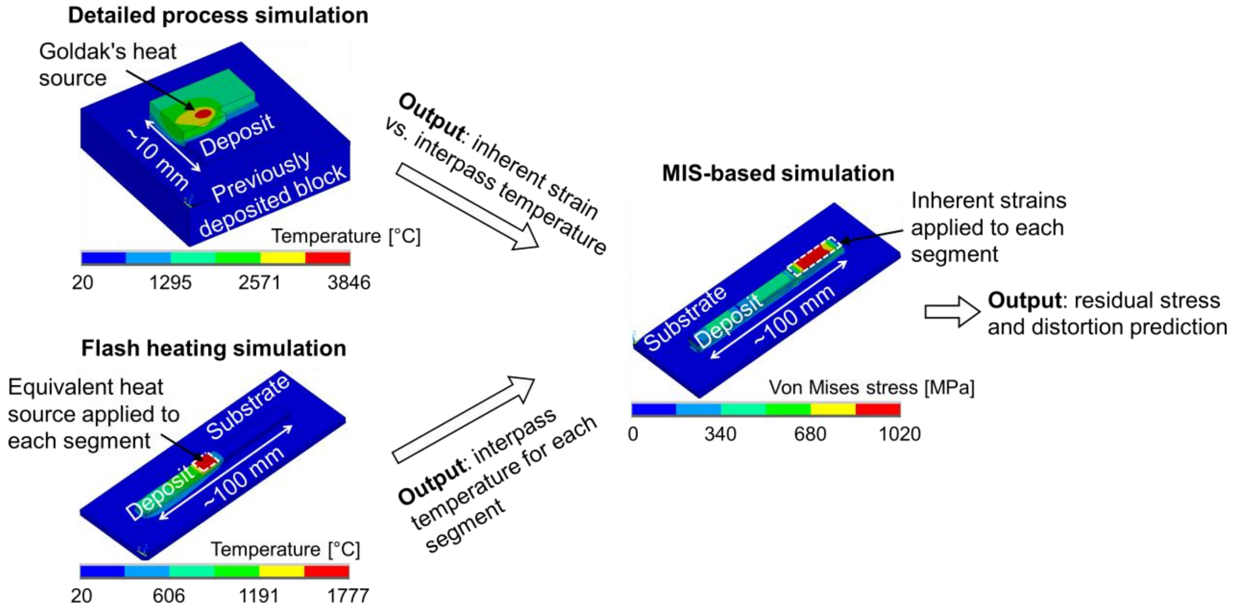

Figure 3.1 General procedures of the extended MIS method for wire-arc DED.

In the thermal analysis of the detailed process simulation, the Goldak volumetric heat source [23] follows a specific path along which the elements are activated incrementally, as shown in Figure 3.2. In contrast, for each layer, the flash heating simulation applies an equivalent power density q segment-by-segment (white-dash-lined domain in Figure 3.2). The power density is calculated by:

$$q = \frac{Q}{L \times W \times H} \tag{3.1}$$

where L, W, H are the length, width, and thickness of the deposited segment, respectively. Q is the effective power used in the Goldak heat source.

This equivalent heat source is held for the same duration as the Goldak heat source would need to finish that segment. Therefore, the total energy input between the two heat sources is conserved for each segment. The benefit of doing so is that once the Goldak heat source is calibrated, the equivalent heat source does not require further calibration. Similar energy-based heat sources have been used for part-scale AM modeling [97-99]. Though the equivalent heat source loses the local thermal gradient around the melt pool, it extensively saves computational time compared with the Goldak heat source. The number of segments in each layer of the deposit varies case by case since it depends on many factors such as the scale of the part, geometrical complexity, and deposition strategies. Specifically, for the thin walls presented in Section 3.4, we choose three segments per layer after sensitivity analysis. It will be seen that this number of segments is accurate enough for obtaining the interpass temperature and stress/strain prediction.

Table 3.1 compares different types of simulation involved in the extended MIS method. To this point, the extended MIS method is able to include the heat accumulation effect by considering it as the change in interpass temperature.

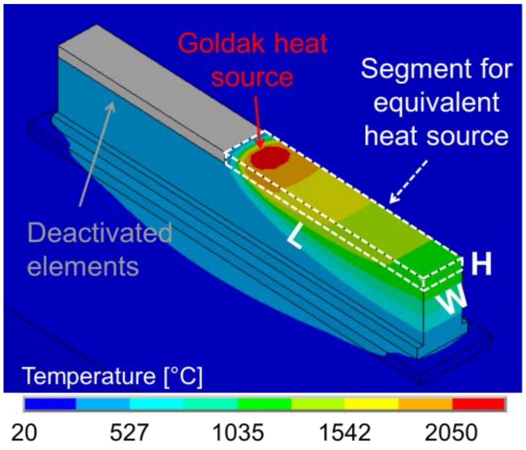

Figure 3.2 Schematic view of the Goldak and equivalent heat source.

Table 3.1 Multiscale simulations involved in the extended MIS method

	Detailed process simulation	Flash heating simulation	MIS-based simulation
FE model scale	Meso-scale	Part-scale	Part-scale
Analysis type	Decoupled thermomechanical (transient thermal & quasi-static elastoplastic mechanical)	Transient thermal	Static elastoplastic mechanical
External load	Goldak volumetric heat source in thermal analysis & thermal profile in mechanical analysis	Equivalent power density	ISs
Material properties	Temperature-dependent & thermomechanical	Temperature-dependent & thermal	Temperatures corresponding to intermediate and steady states & mechanical
Element activation mode	Step-by-step	Segment-by-segment	Segment-by-segment
Description	For each time step, the heat source moves a small distance, like the actual melt pool	For each deposited domain (segment), the action time of the equivalent power density equals the real printing time	For each deposited domain (segment), ISs are applied according to its interpass temperature

3.3 Solid-state Phase Transformation of Ti6Al4V

3.3.1 Calculation of Phase Fractions

In this chapter, the deposition material used in the wire-arc DED process is Ti6Al4V, a dual-phase ($\alpha + \beta$) alloy where the aluminum works as α stabilizer and the vanadium as β stabilizer [100]. The microstructure of the α phase is hexagonal close-packed (HCP), and the β phase is body-centered cubic (BCC) [101].

During the wire-arc DED process, repeated heating and cooling of deposited Ti6Al4V bring in complex heat transfer physics, leading to the solid-state phase transformation (SSPT). Since different microstructures result in changes in material properties like Young's modulus and yield strength [102], the SSPT affects the strain and stress evolution of the deposit. In the present study, the SSPT is encoded in the material's constitutive model and considered in the detailed process simulation, as shown in Figure 3.3. After the transient thermal analysis, the temperature histories of each element are extracted. These data have two functions: (1) they are imported to the subsequent mechanical analysis as thermal loads; (2) they are used to calculate the phase fractions in each element and further used to acquire the mechanical material properties based on the rule of mixtures.

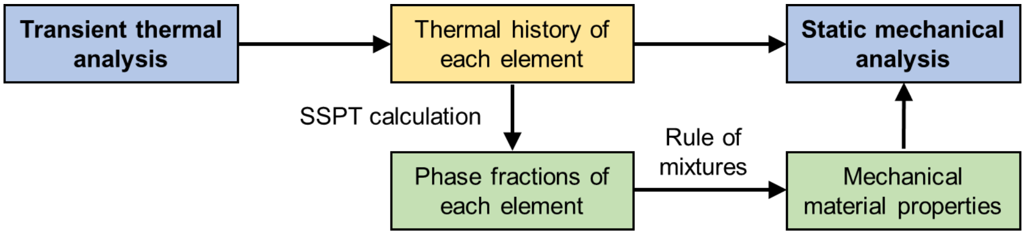

Figure 3.3 Workflow of detailed process simulation with the consideration of SSPT.

In the SSPT calculation, some assumptions and simplifications are made:

(1) There are only three phases involved, that is, α, β, and martensite α'. Literature has reported that there are different types of α phase, such as grain boundary α_{GB} and Widmanstätten α_W [103, 104]. Since their difference in mechanical properties are not clear, for simplification, we do not distinguish them [105]. It is further assumed that the equilibrium phase fractions of α and β at ambient temperature are 0.91 and 0.09, respectively [103].

(2) Although the SSPT among different phases coincides in reality, an order of occurrence is specified to simplify the calculation.

(3) The phase fractions of an element only depend on its own temperature history and, therefore, can be calculated individually.

(4) Only the mechanical properties have phase dependence and are applicable to the rule of mixtures. The thermal properties are considered phase-independent.

The SSPT calculation in the present study is adapted from Ref. [103, 106] and is shown schematically in Figure 3.4. It mainly contains two branches: the decomposition (D paths) and formation (F paths) of the β phase. The calculation is performed at the beginning of every time step in the mechanical analysis. For time step ${}^{n+1}t$, Table 3.2 lists the input arguments at the beginning and the updated arguments at the end.

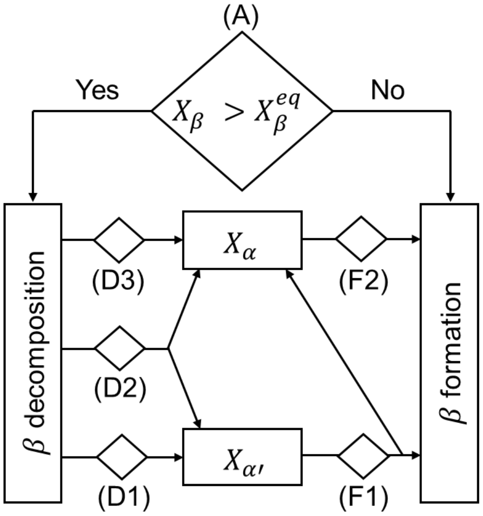

Figure 3.4 Workflow of SSPT calculation (D# and F# represent different transformation paths).

Table 3.2 Input and updated arguments for SSPT calculation at time step ^{n+1}t

Input at the beginning of time step ^{n+1}t	Updated at the end of time step ^{n+1}t
$^{n}X_\alpha$, α fraction at time step ^{n}t	$^{n+1}X_\alpha$, α fraction at time step ^{n+1}t
$^{n}X_\beta$, β fraction at time step ^{n}t	$^{n+1}X_\beta$, β fraction at time step ^{n+1}t
$^{n}X_{\alpha'}$, α′ fraction at time step ^{n}t	$^{n+1}X_{\alpha'}$, α′ fraction at time step ^{n+1}t
^{n}T, temperature at time step ^{n}t	
^{n+1}T, temperature at time step ^{n+1}t	
$^{n+1}\Delta t = {}^{n+1}t - {}^{n}t$, time increment	

The detailed SSPT calculations are described as follows:

(A) Calculate the equilibrium phase fractions at the current temperature ${}^{n+1}T$ [103, 106]:

$$ {}^{n+1}X_{\alpha}^{eq} = \begin{cases} 0.91(1 - 1/\exp\left(0.013(T_{\beta}^{trans} - {}^{n+1}T)\right)) & {}^{n+1}T < T_{\beta}^{trans} \\ 0 & {}^{n+1}T \geq T_{\beta}^{trans} \end{cases} \tag{3.2} $$

$$ {}^{n+1}X_{\beta}^{eq} = 1 - {}^{n+1}X_{\alpha}^{eq} \tag{3.3} $$

$$ {}^{n+1}X_{\alpha'}^{eq} = 0.5\left(1 + \tanh\left(\frac{T_A - {}^{n+1}T}{80}\right)\right) \tag{3.4} $$

where ${}^{n+1}X_{\alpha}^{eq}$, ${}^{n+1}X_{\beta}^{eq}$, and ${}^{n+1}X_{\alpha'}^{eq}$ are equilibrium fractions of α, β, and α' at ${}^{n+1}t$ respectively. $T_{\beta}^{trans} = 1000$ ℃ is the beta transus, above which only β exists [106]. $T_A = 450$ ℃ is a material-related constant [106].

(D) If ${}^{n}X_{\beta} > {}^{n+1}X_{\beta}^{eq}$, the excess β transforms into α or α' depending on the current temperature ${}^{n+1}T$ and cooling rate (CR):

$$ \mathrm{CR} = \left({}^{n+1}T - {}^{n}T\right)/{}^{n+1}\Delta t \tag{3.5} $$

(B1) If $\mathrm{CR} < -410$ ℃/s and ${}^{n+1}T < T_{MS}$, the transformation into α is suppressed and a 100% martensite microstructure is formed. $T_{MS} = 650$℃ is the martensite start temperature, above which the martensite transformation does not occur [105, 107]. The diffusionless Koistinen-Marburger (K-M) equation is adopted to calculate ${}^{n+1}X_{\alpha'}$ [104]:

$$ {}^{n+1}X_{\alpha'} = \left(1 - \exp\left(-b_{KM}\left(T_{MS} - {}^{n+1}T\right)\right)\right)\left({}^{n}X_{\beta} + {}^{n}X_{\alpha'}\right) \tag{3.6} $$

where b_{KM} is a material-dependent constant, which equals to 0.005 in this study [104].

(B2) If -410 ℃/s $< \mathrm{CR} < -20$ ℃/s and ${}^{n+1}T < T_{MS}$, both diffusion-controlled α and diffusionless-controlled α' are formed. For simplification, the modified K-M equation below is applied [104]:

$$ {}^{n+1}X_{\alpha'} = \left(1 - \exp\left(-b_{KM}\left(T_{MS} - {}^{n+1}T\right)\right)\right)\left({}^{n}X_{\beta} + {}^{n}X_{\alpha'} - {}^{n+1}X_{\beta}^{eq}\right) \tag{3.7} $$

(B3) If the conditions for Equations (3.6) and (3.7) are not satisfied, such as if the cooling rate is slower than $-20\ ℃/\mathrm{s}$ or the current temperature is above T_{MS}, the diffusional transformation into α takes place. The formation of α is computed by the discrete Johnson-Mehl-Avrami-Kolmogorov (JMAK) equations [100, 105]:

$$ {}^{n+1}X_{\alpha} = \left(1 - \exp\left(-k_{\beta\alpha}\left(t_c + {}^{n+1}\Delta t\right)^{N_{\beta\alpha}}\right)\right)\left({}^{n}X_{\beta} + {}^{n}X_{\alpha}\right){}^{n+1}X_{\alpha}^{eq} \tag{3.8} $$

$$ t_c = \left[-\ln\left(1 - \frac{{}^{n}X_{\alpha} / {}^{n+1}X_{\alpha}^{eq}}{{}^{n}X_{\beta} + {}^{n}X_{\alpha}}\right)\Big/ k_{\beta\alpha}\right]^{1/N_{\beta\alpha}} \tag{3.9} $$

where t_c is an artificial time parameter that accounts for the previously formed α phase. The parameters $k_{\beta\alpha}$ (see Figure 3.5) and $N_{\beta\alpha} = 2.5$ are taken from the TTT diagram of Ti6Al4V in Ref. [100, 105].

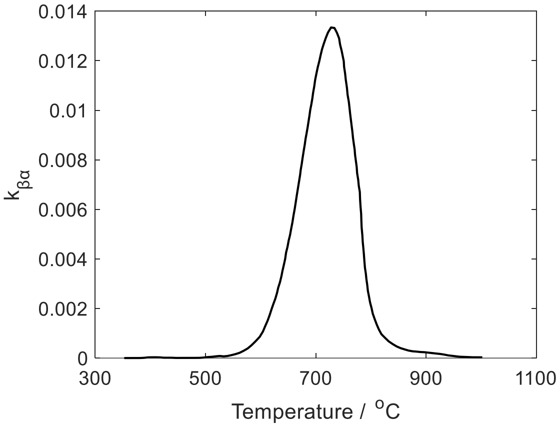

Figure 3.5 Kinetic parameters $k_{\beta\alpha}$ for JMAK equation [105].

(F) If ${}^{n}X_{\beta} < {}^{n+1}X_{\beta}^{eq}$, the β phase will be formed by consuming existing α and α' phases.

(F1) It is assumed that the martensite α' is consumed first if ${}^{n}X_{\alpha'} > {}^{n+1}X_{\alpha'}^{eq}$ [106]:

$$ {}^{n+1}X_{\alpha'} = {}^{n+1}X_{\alpha'}^{eq} + \left(\exp\left(-k_m\left(t_{cm} + {}^{n+1}\Delta t\right)^{N_m}\right)\right)\left({}^{n}X_{\alpha'} + {}^{n}X_{\beta} - {}^{n+1}X_{\alpha'}^{eq}\right) \tag{3.10} $$

$$t_{cm} = \left[-\ln \left(\frac{{}^{n}X_{\alpha'} - {}^{n+1}X_{\alpha'}^{eq}}{{}^{n}X_{\alpha'} + {}^{n}X_{\beta} - {}^{n+1}X_{\alpha'}^{eq}} \right) \Big/ k_m \right]^{1/N_m} \tag{3.11}$$

$$k_m = \begin{cases} (-4.58 \times 10^{-5})^{n+1}T + 1.04, & {}^{n+1}T < 500℃ \\ (5.40 \times 10^{-5})^{n+1}T + 0.99, & {}^{n+1}T \geq 500℃ \end{cases} \tag{3.12}$$

$$N_m = \begin{cases} (4.39 \times 10^{-3})^{n+1}T - 1.09, & {}^{n+1}T < 500℃ \\ (7.33 \times 10^{-4})^{n+1}T + 0.74, & {}^{n+1}T \geq 500℃ \end{cases} \tag{3.13}$$

Note that the consumed martensite α' is transformed into not only β but also α phase according to the ratio of their equilibrium fractions [106]:

$${}^{n+1}X_{\alpha} = {}^{n}X_{\alpha} + \left({}^{n}X_{\alpha'} - {}^{n+1}X_{\alpha'} \right) {}^{n+1}X_{\alpha}^{eq} \tag{3.14}$$

$${}^{n+1}X_{\beta} = {}^{n}X_{\beta} + \left({}^{n}X_{\alpha'} - {}^{n+1}X_{\alpha'} \right) {}^{n+1}X_{\beta}^{eq} \tag{3.15}$$

(F2) If ${}^{n}X_{\alpha'} < {}^{n+1}X_{\alpha'}^{eq}$, the martensite phase α' does not change, while the transformation of α into β takes place with a parabolic growth rate [100, 106]:

$${}^{n+1}X_{\alpha} = \begin{cases} 1 - {}^{n+1}X_{\beta}^{eq} f_{diss}\left({}^{n+1}T\right) \sqrt{{}^{n+1}\Delta t + t^*}, & 0 < {}^{n+1}\Delta t + t^* < t_{crit} \\ 1 - {}^{n+1}X_{\beta}^{eq} = {}^{n+1}X_{\alpha}^{eq}, & {}^{n+1}\Delta t + t^* > t_{crit} \end{cases} \tag{3.16}$$

$$t^* = \left(\frac{{}^{n}X_{\beta}}{{}^{n+1}X_{\beta}^{eq} f_{diss}\left({}^{n+1}T\right)} \right)^2 \tag{3.17}$$

$$t_{crit} = 1 \Big/ \left(f_{diss}\left({}^{n+1}T\right) \right)^2 \tag{3.18}$$

$$f_{diss}\left({}^{n+1}T\right) = 2.2 \times 10^{-31} \left({}^{n+1}T\right)^{9.89} \tag{3.19}$$

We implement the above SSPT calculations using the ANSYS 2020 R1 user subroutine (user-defined material, USERMAT) and validate the code by comparing the results with literature for a case where a single element undergoes a temperature profile shown in Figure 3.6(a). The change of total α fraction (sum of α and α', $X_{\alpha+\alpha'}$) is shown in Figure 3.6(b). It can be seen that the results calculated in the present work are in good agreement with those found in the literature by Sun et al. [104], Babu et al. [108], Baykasoglu et al. [106], and Murgau et al. [109]. The slight difference is attributed to these possible reasons: (1) the temperature history is grabbed from images in the literature instead of directly from data files; (2) parameters used in the calculation, such as T_A in Equation (3.4), $k_{\beta\alpha}$ and $N_{\beta\alpha}$ in Equation (3.8), may vary among different works. Overall, the SSPT calculation in the present study is consistent with the published data.

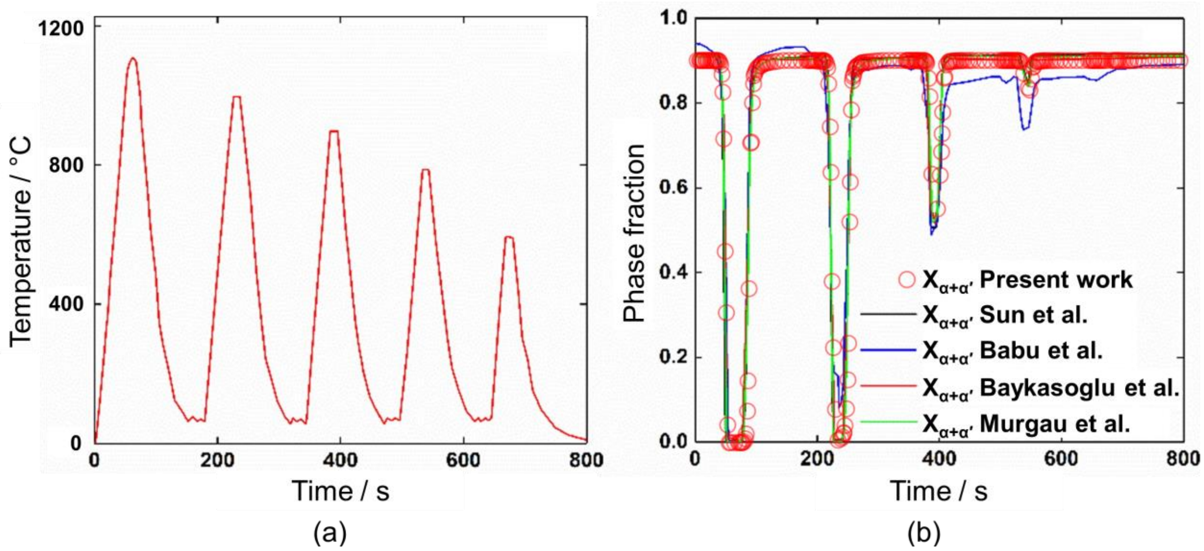

Figure 3.6 (a) Temperature history profile; (b) variation of phase fraction $X_{\alpha+\alpha'}$ reported in literature and present work. (Adapted from Ref. [104])

3.3.2 Calculation of Material Properties

Most studies on numerical modeling of metal AM processes involve temperature-dependent material properties. For Ti6Al4V, since the phase fractions can directly affect the thermal and mechanical behavior of the material, the phase-dependent properties should also be included in the modeling [100]. Baykasoglu et al. [103] have shown that ignoring the variation in thermal properties caused by the microstructure change is acceptable when predicting the microstructural evolution of Ti6Al4V for DED processes. Therefore, in the current study, the thermal properties of Ti6Al4V, such as density, thermal conductivity, and heat capacity, are only temperature-dependent and unrelated to the phase fractions for simplification. In contrast, the mechanical properties of Ti6Al4V are determined not only by temperature but also by microstructure, based on the rule of mixtures shown in Equation (3.20) [102]. Due to the lack of data, we assume only the yield strength and Young's modulus are phase-dependent, while other properties such as thermal expansion coefficient and Poisson's ratio are unaffected.

$$E(T) = E_{\alpha}(T)X_{\alpha} + E_{\beta}(T)X_{\beta} + E_{\alpha'}(T)X_{\alpha'} \tag{3.20}$$

where $E(T)$ is the material property at temperature T. $E_{\alpha}(T)$, $E_{\beta}(T)$, $E_{\alpha'}(T)$ are the material properties of α, β, and α' phases. X_{α}, X_{β}, $X_{\alpha'}$ are the volume fractions of α, β, and α' phases. The phase fractions are not written as a function of temperature T because they mainly depend on the deposition process and need to be calculated through the transient thermal analysis in the detailed process simulation.

3.4 Experimental Validation

3.4.1 Heat Source Calibration

Before we run the detailed process simulation to calculate the ISs for Ti6Al4V, we first calibrate the Goldak ellipsoidal heat source model. The heat source parameters, such as length, width, depth, and absorptivity, are determined by comparing the results of numerical simulation and experimental measurement.

A single-layer Ti6Al4V strip is deposited on a substrate made of the same material. The torch follows a zigzag path, as shown in Figure 3.7 top, where the toolpath width is 20 mm, and the track distance is 3 mm. Using such a zigzag path ensures the melt pool stability and product quality based on manufacturing experience. The track distance is usually a constant for all the tasks, while the toolpath width depends on the part geometry. The zigzag path is employed throughout this study in both numerical simulation and experiment. As shown in Figure 3.7 bottom, three transverse sections (Section A-A, B-B, and C-C) are selected for the melt pool measurement through an optical microscope. The primary process parameters of the wire-arc DED machine are current 18.5 A, voltage 187 V, and torch speed 30 mm/s. Note that the listed current and voltage are averages over time because the instantaneous values experience periodic cycles. Details regarding the wire-arc DED process and the variations in current and voltage can be found in Ref. [109, 110].

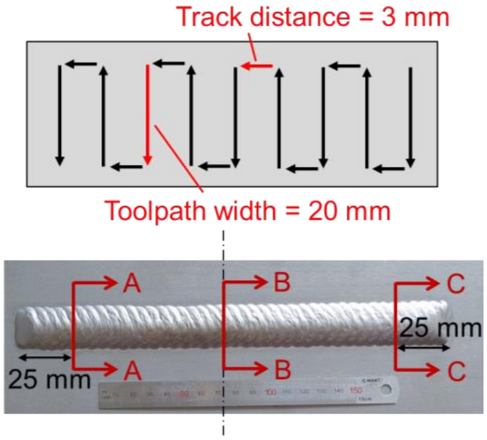

Figure 3.7 Zigzag path of the torch (top); deposited single-layer strip (bottom).

The calibration uses a meso-scale FE model shown in Figure 3.8. It includes a single-layer deposit of $18.4 \times 26.4 \times 2.55$ mm^3 and a substrate of $28 \times 40 \times 10.8$ mm^3. Although the actual cross-section of the deposit has a semi-ellipsoidal-like shape, we use a rectangle in the FE model for simplicity. The rectangle's width is the same as the deposit width, while its height is determined based on the constraint that the cross-sectional areas of the actual and simulated deposit are equal. The deposit and its immediately adjacent substrate are meshed with 8-node block elements to ensure accuracy, while the rest of the substrate is meshed with 4-node tetrahedral elements to save computational time. Like the actual torch, the Goldak heat source in the simulation moves along a zigzag path (marked by yellow arrows in Figure 3.8). The snapshots of temperature distribution over an observed cross-section (see Figure 3.8) at four instants are shown in Figure 3.9. The maximum value of the contour legend is set to the melting point of Ti6Al4V, $T_m = 1660\ ^{\mathrm{o}}\mathrm{C}$. Elements above T_m are displayed in grey, representing a melted area. The boundary between the melted and unmelted material is called the fusion line. At *t* = 0.827 s, the torch is located at the left end of the cross-section. It moves toward the negative X-axis and reaches the right end at *t* = 1.524 s. As can be seen, unlike the straight path, the zigzag path results in a constantly changing cross-sectional shape of the melt pool. In other words, the fusion line is not stable. For calibration, we extract the envelope of the fusion lines at different instants on the observed cross-section from the simulation and compare it with the microphotographs from the experiment. The results are shown in Figure 3.10, where the red dashed line is the envelope of fusion lines. It can be seen that (1) the calibrated process parameters yield a melt pool shape that matches the measurement; (2) the melt pool shapes in three measured cross-sections are similar, indicating a stable deposition under the current process parameters and also justifying that the ISs extracted from a small representative model are applicable to a part-scale model. The parameters of the calibrated heat source model are half-length $a = 3$ mm, half-width $b = 3$ mm, depth $c = 6.4$ mm, and absorptivity $\eta = 0.9$. Note that calibration of the heat source model has been performed on a base plate alone since the melt pool boundary is only visible in the base plate but not in the build itself for Ti6Al4V. The calibration may be more accurate if an in-situ melt pool monitoring camera is used to capture the melt pool dimensions in the deposit. This will be left as future work to examine the effectiveness of this calibration approach.

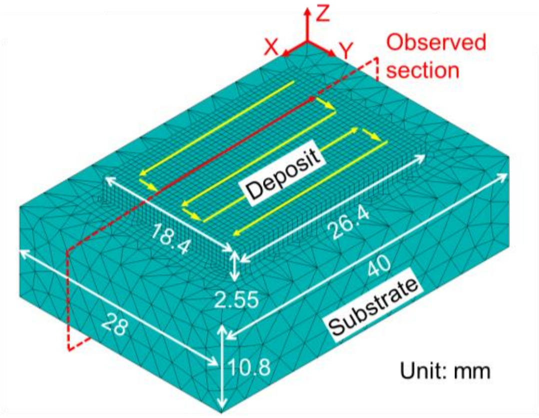

Figure 3.8 Meso-scale FE model for heat source calibration.

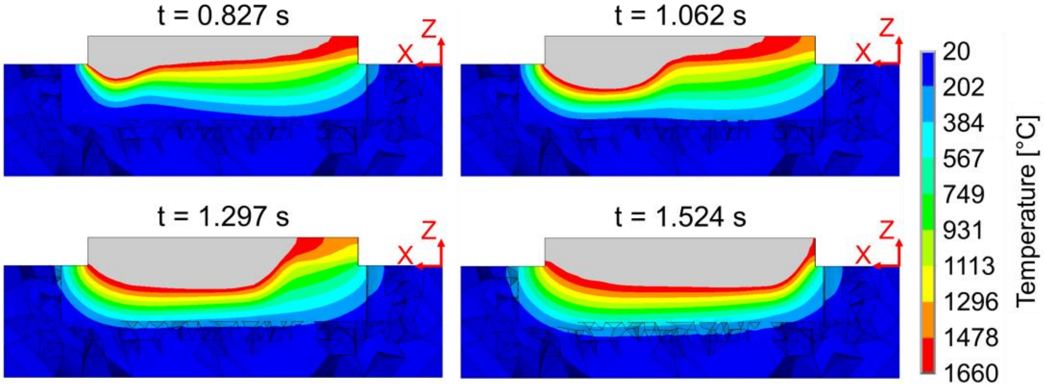

Figure 3.9 Snapshots of temperature profile on the observed section.

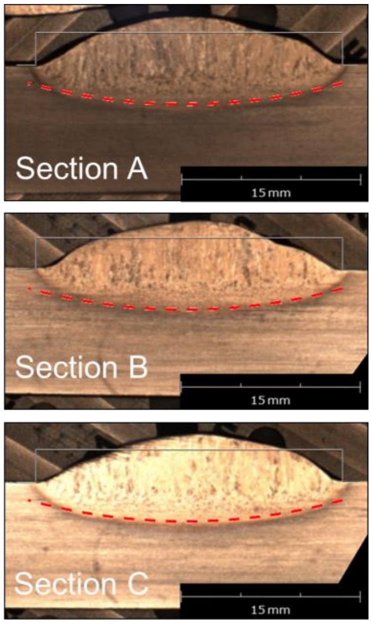

Figure 3.10 Comparison of the cross-section (red dashed lines are the envelope of the fusion lines).

3.4.2 Extraction of Inherent Strains

After heat source calibration, as shown in Figure 3.11, another meso-scale FE model is employed to implement the detailed process-microstructure simulation for extracting the ISs for different interpass temperatures. The reason for not using the same FE model as in Section 3.4.1 is that the heat source calibration is implemented based on a single-layer strip, which is not general. The FE model used in this section contains a three-layer deposit and a base that is considered as the previously deposited block. The build direction is along the positive Z-axis. The deposition is in the XY-plane for each layer, where the heat source follows a zigzag path with alternating start and end points. In other words, the endpoint of the current layer is the start-point of the next layer, except the height is raised by a layer thickness.

The boundary conditions in the thermal analysis are described as follows: (1) during the deposition, the base bottom is subjected to a fixed temperature $T_{interpass}$ that can be considered as the interpass temperature; (2) after deposition, the fixed temperature constraint is removed, and heat convection with a coefficient of H_{bot} is applied to the base bottom until the entire structure cools to ambient temperature (20 °C); (3) the outer surface of the deposit and base, excluding the base bottom, is subjected to heat convection with a coefficient of H_{out} all the time during the deposition and subsequent cooling. Similar boundary conditions are employed in Ref. [110] to investigate the influence of preheating and cooling rates on microstructures of Ti6Al4V in L-PBF processes. In this study, $T_{interpass}$ varies from 20 °C to 800 °C. The convection coefficients $H_{bot} = 130\ \mathrm{W/(m^2K)}$ and $H_{out} = 90\ \mathrm{W/(m^2K)}$ are experimentally calibrated based on the thermocouple data presented in Section 3.4.3. In the subsequent mechanical analysis, the base bottom is fixed in all directions because, in the wire-arc DED process, the base is commonly tightly fixed on a stiff platform to avoid possible distortion during the deposition.

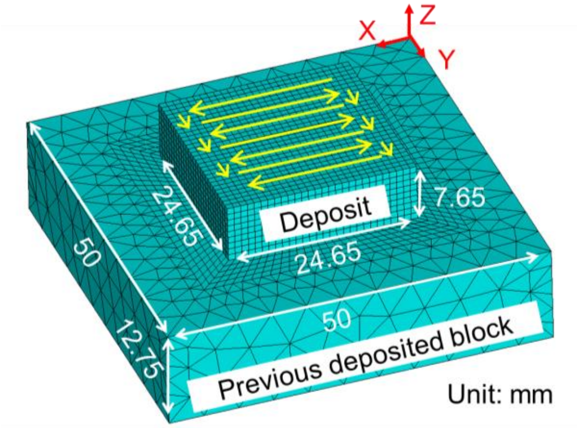

Figure 3.11 Meso-scale FE model for detailed process simulation.

After the detailed process simulation, ISs are extracted element by element within the deposit. Two edge-to-edge paths, AB and CD, are selected to present typical IS distributions in the top layer, as shown in Figure 3.12. The IS values along line AB fluctuate. It is because the material on line AB is not deposited through one scanning track but through multiple parallel tracks that are orthogonal to line AB. The moving heat source repeatedly and alternately traverses line AB along with positive and negative X-axis, resulting in different thermal profiles and ISs for each element within line AB. In contrast, the material on line CD is deposited through a single track and therefore exhibits more stable ISs. The dramatic changes of ISs at the ends of line CD are related to the boundary conditions and movement of the heat source.

In the detailed process simulation, fluctuations in the ISs are inevitable due to the complex thermomechanical evolutions and the high resolution of the detailed process model. Similar to our previous works [48, 49, 59], we calculate the average ISs over a region inside the deposit. As shown in Figure 3.12, the average region is in the center of the deposit. Its length (in X-direction) and width (in Y-direction) are set to 55% of the deposit size to exclude boundary effects. Its depth (in Z-direction) is the same as the deposit so that the interlayer effect can be included.

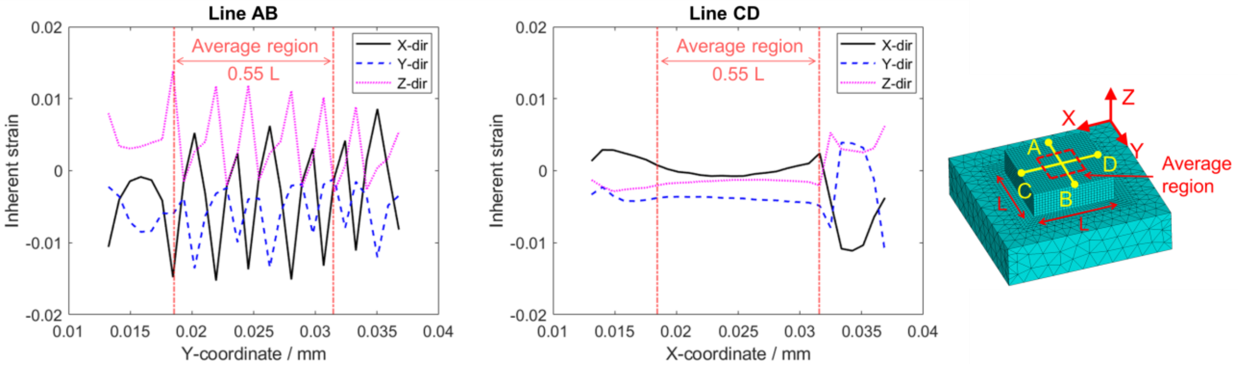

Figure 3.12 IS distributions in the top layer along line AB and line CD (detailed process simulation is implemented with $T_{interpass} = 20$ ℃ and w/ SSPT).

The average ISs for different interpass temperatures are calculated and visualized in Figure 3.13. The directions of strain components are consistent with the coordinate system in Figure 3.11. Overall, ISs are positive in the build direction (Z-direction) and negative in the printing plane (X- and Y-direction). The zigzag scanning path causes the differences in ISs in the X and Y directions. As the interpass temperature increases, the magnitude of ISs in all directions decreases. The reason for this trend is discussed as follows.

As shown in Equation (2.2) and (2.3), the IS in the MIS method is equal to the intermediate state term $\varepsilon_i^{elastic} + \varepsilon_i^{plastic}$ subtracted by the steady state term $\varepsilon_s^{elastic}$. The intermediate state term is usually negative along/transverse the scanning direction in the printing plane and positive in the build direction, and the steady state term is usually positive in all directions. Given that the material always returns to ambient temperature where thermal strains vanish, the interpass temperature is considered to have little effect on the steady state term. On the other hand, the elevated interpass temperature reduces the influence of local thermal gradients around the melt pool during the deposition, thus reducing the intermediate state term in magnitude. Therefore, as the interpass temperature increases, the intermediate state term decreases in magnitude while the steady term does not change too much, resulting in a decrease in the magnitude of ISs in all directions.

In Figure 3.13, the changes in ISs with increasing interpass temperature seem small compared with the fluctuations against locations shown in Figure 3.12. But these changes are indeed caused by the interpass temperature rather than the strain fluctuations within the deposit since the ISs in Figure 3.13 are obtained using the same average method and within the same region of the FE model.

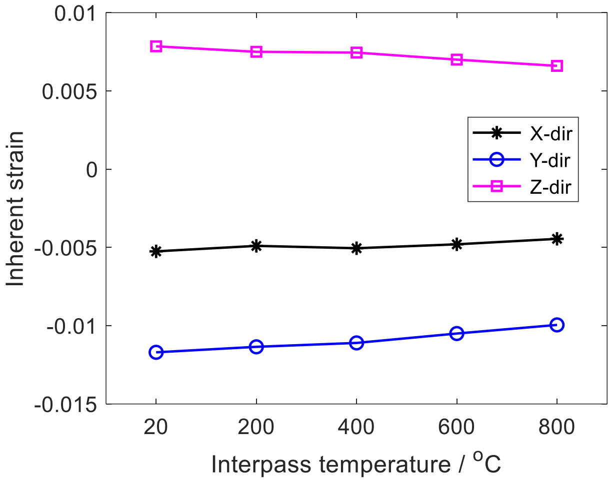

Figure 3.13 ISs extracted from detailed process simulations at various interpass temperatures.

To further investigate the influence of interpass temperature on stress evolution in the deposit, the von Mises stress histories at three observed points, P1, P2, and P3, are extracted and plotted in Figure 3.14. The observed points are located in the center of each layer. For P2 and P3, the higher the interpass temperature, the lower the von Mises stress in the as-built deposit. Similar results are reported in Ref. [111]. However, at P1 in the first layer, the von Mises stress in the as-built deposit converges. An explanation is that the deposition of the second and third layers repeatedly heats the first layer, weakening the impact of the interpass temperature.

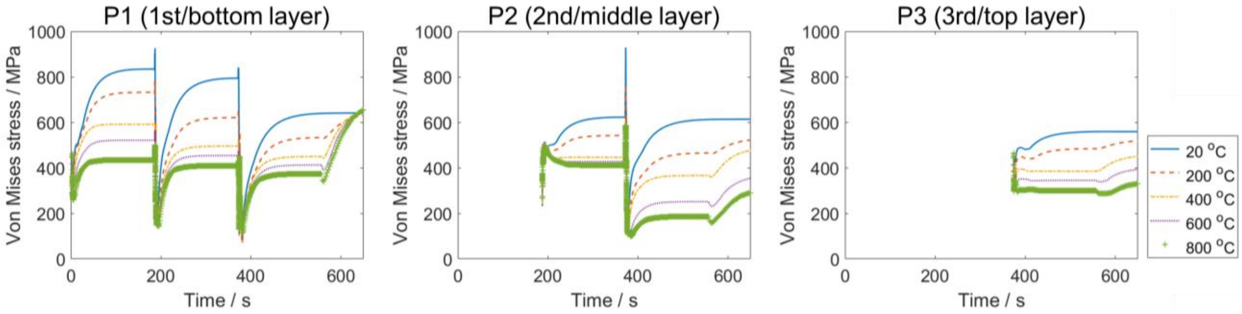

Figure 3.14 Von Mises stress histories at observed points.

As a quick verification, we apply the ISs for interpass temperature of 20 °C to the same FE model (see Figure 3.11) as in the detailed process simulation and compare the stress distributions along line AB and CD on top of the deposit, as shown in Figure 3.15. Overall, the detailed process and the MIS-based simulations are in good agreement. The heat source repeatedly crosses over line AB in the detailed process simulation, resulting in stress fluctuations in all directions (see Figure 3.15(a)). In contrast, since line CD is parallel to most scanning paths, the stresses along line CD are relatively smoother than those along line AB (see Figure 3.15(b)). Note that in this verification case: (1) the constant ISs work well because the base bottom is fixed at a specific interpass temperature (20 °C), that is, there is no heat accumulation; (2) the MIS method cannot reflect the stress variations along these two lines because averaged ISs are applied to the entire layer. To summarize, the MIS method can approximately reconstruct the stress distribution obtained by the detailed process simulation.

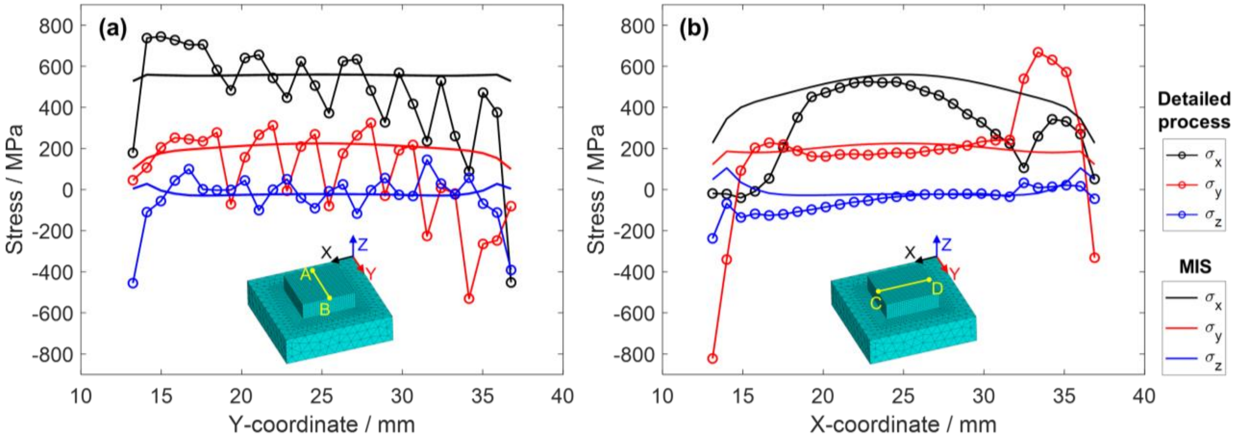

Figure 3.15 Stresses in X-, Y-, and Z-directions: (a) along line AB; (b) along line CD.

3.4.3 Flash Heating Simulation on Ti6Al4V Walls

Two Ti6Al4V thin-walled deposits are selected to validate the temperature-dependent MIS method. As shown in Figure 3.16, the small wall is 112 × 14 × 27 mm^3 and the large wall is 250 × 20 × 27 mm^3 in size. Both walls have ten layers. They are deposited using the same build strategy (i.e., zigzag path) with the same process parameters and are built on the substrate made of the same material. The interlayer dwell time is 60 s. Besides the difference in deposit dimensions, the substrates for these two walls are also different. The small wall has a substrate much larger than itself, making the distortion in the substrate barely unmeasurable. The large wall, on the other hand, has a comparable substrate that deforms significantly after the deposition. As mentioned in Section 3.2, each layer of both walls is divided into three segments for the flash heating and MIS-based simulations. It will be shown in this section that three segments are sufficient to obtain accurate predictions for interpass temperature, residual stress, and deformation.

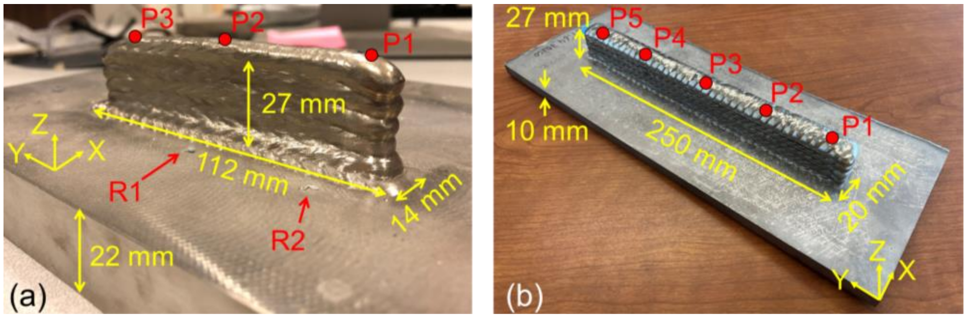

Figure 3.16 Validation samples: (a) small wall and (b) large wall.

Due to the small size of the wall shown in Figure 3.16(a), the detailed process simulation for the entire structure is feasible. Therefore, both detailed process and flash heating simulations are performed for the small wall. During the deposition, two thermocouples, R1 and R2, are attached to the top of the substrate to collect thermal data. The temperature comparison between the simulation and experiment is shown in Figure 3.17. It can be observed that both heat source models (Goldak and equivalent) yield temperature histories close to the thermocouple data. Note that there are some spikes in the experimental curves, possibly due to electrical noise induced by the arc when it is close to the thermocouple. Following a similar experimental procedure for the small wall, the temperature comparison of the large wall is shown in Figure 3.18. During the experiment, two thermocouples are attached to the substrate top (R1 and R2). In this case, using the Goldak heat source (detailed process simulation) is impractical due to the large deposit size, and thus only the flash heating simulation is performed. Similar to the small wall, there are some abnormal spikes in temperature measurement. Overall, the simulated thermal profile agrees with the experimental measurement. Although the flash heating simulation cannot capture the temperature distribution around the melt pool as well as the detailed process simulation, it can be used to obtain far-field temperature distributions like the interpass temperature in the temperature-dependent MIS method.

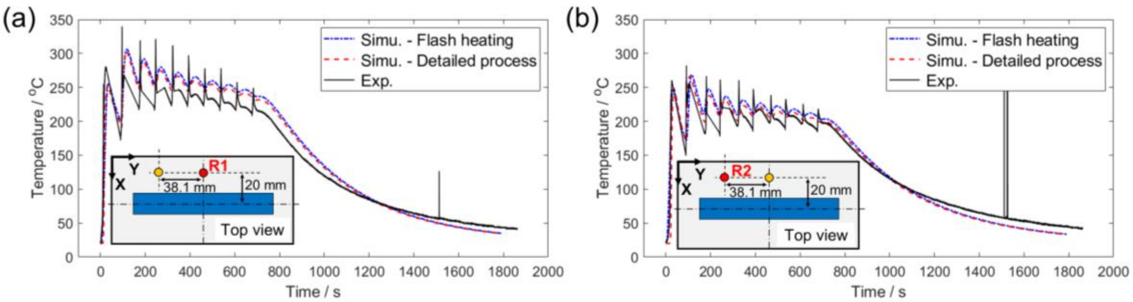

Figure 3.17 Temperature comparison for the small wall at (a) R1 and (b) R2.

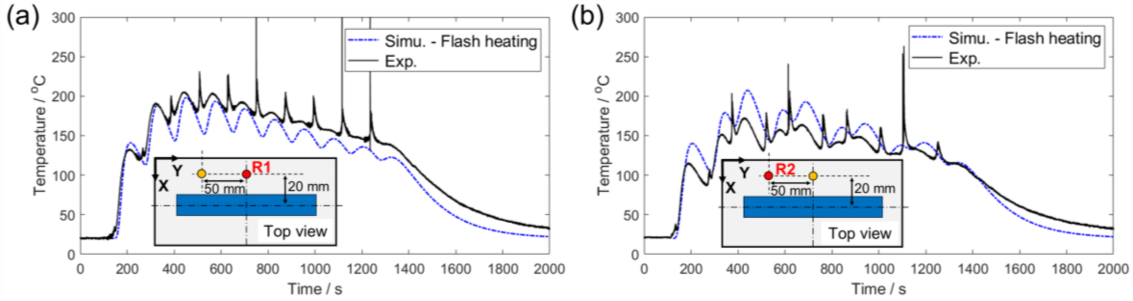

Figure 3.18 Temperature comparison for the large wall at (a) R1 and (b) R2.

The interpass temperatures for each layer are calculated after the flash heating simulation and shown in Figure 3.19, where the solid line and shaded area respectively represent the average and standard deviation. The overall trend is that the interpass temperature increases with the wall height. For the first two layers, the small and large walls have very similar interpass temperatures, indicating that the wall geometry has little effect on the heat accumulation at the beginning of the deposition. The interpass temperature of the large wall is higher than that of the small wall for Layer 3 and Layer 4, and becomes lower from Layer 6 onwards. The different increase rates of the interpass temperature for these two walls can be attributed to their geometries. The average interpass temperatures of the last two layers are almost the same for the small wall, indicating that heat input and dissipation are close to balance. Note that the standard deviation is more remarkable for the large wall than for the small wall. This is because the layer area of the large wall is greater, and therefore the non-uniformity of the interpass temperature distribution is more significant.

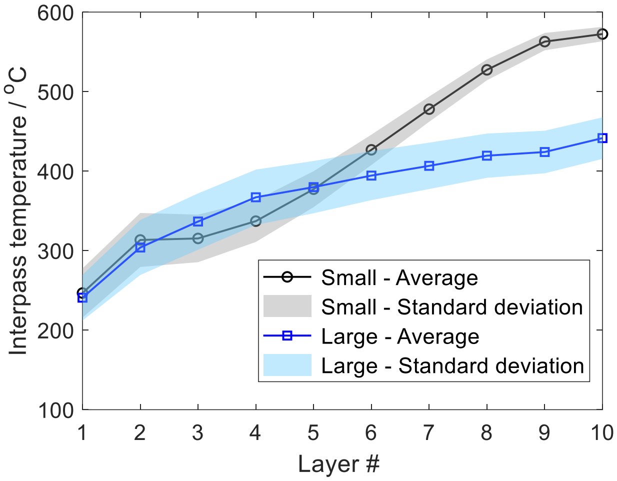

Figure 3.19 Average interpass temperature variation.

3.4.4 MIS-based Simulation on Ti6Al4V Walls

Given the interpass temperature calculated from the flash heating simulation, the MIS-based simulation applies different ISs to each segment according to the IS versus the interpass temperature relationship (see Figure 3.13). Mechanical analysis of the small wall using the Goldak heat source (detailed process simulation) is conducted because the computational cost is acceptable; however, this is not applicable for the large wall. As a comparison, the previous MIS method that uses constant ISs (at 20 °C) is also employed to evaluate the stress and deformation of the walls.

The von Mises stresses at several points on top of each thin-walled deposit are extracted and compared with the experimental measurement by X-ray diffraction (XRD). The approximate locations of these points are given in Figure 3.16: three on the small wall (P1-P3) and five on the large wall (P1-P5). The comparison results and the specific measurement locations are visualized in Figure 3.20 and Figure 3.21. The exact stress values can be found in the Appendix.

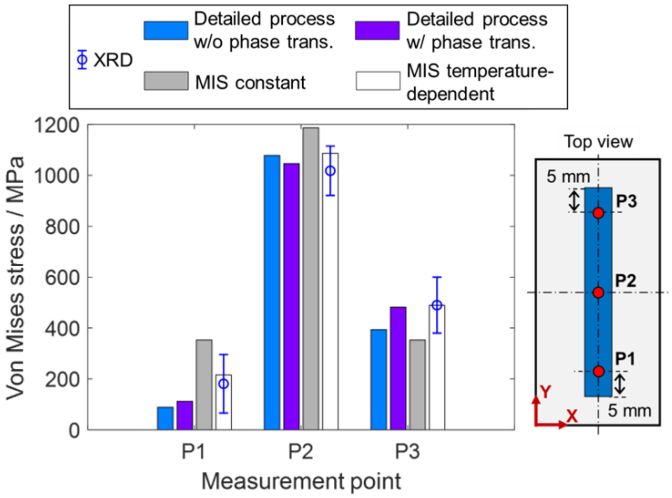

Figure 3.20 Von Mises stress comparison for the small wall.

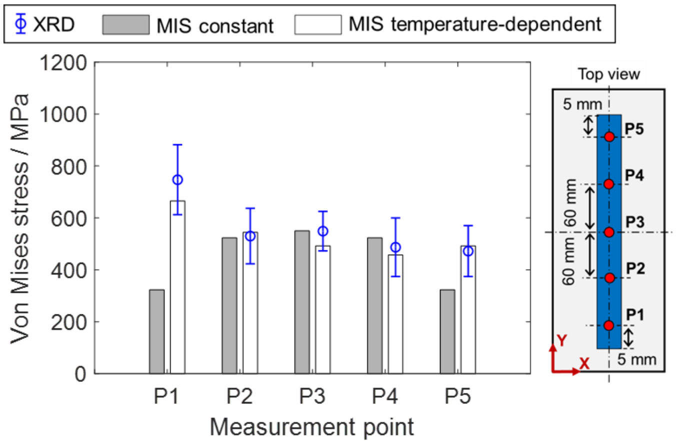

Figure 3.21 Von Mises stress comparison for the large wall.

For the small wall, the simulation results agree well with the XRD data. Stresses predicted by the temperature-dependent MIS method are within the experimental error bars for all measured locations. In contrast, the constant MIS method has all the predictions as outliers. According to XRD, the residual von Mises stress at the deposit center (P2) is much higher than at the deposit ends (P1 and P3), likely because the center point is more constrained structurally than the endpoints. Both MIS methods can capture this trend. Further, the XRD reveals that the stresses at P1 and P3 are different, which could be attributed to the deposition path (the torch moves through P1-P2-P3 to finish the top layer) and the resultant difference in interpass temperatures. The constant MIS cannot find the stress difference between P1 and P3 because it does not consider the aforementioned factors and applies constant ISs to all the layers. In contrast, the temperature-dependent MIS can more accurately predict the stresses at P1 and P3. The detailed process simulation results (w/o and w/ phase transformation) indicate that including the SSPT can increase the accuracy of stress prediction. Similar conclusions have been reported by other researchers [102, 112]. The ISs used in the present study are extracted from a detailed process FE model where the SSPT is considered. It is worth noting that although the detailed process simulation and the temperature-dependent MIS method both have predictions close to the measurement, the MIS-based simulation only takes about 13 min to complete, compared to 6.5 h for the detailed process simulation.

For the large wall, the temperature-dependent MIS method also predicts the residual von Mises stress well (see Figure 3.21). Similar to the small wall, stress predictions by the constant MIS are symmetric on measurement locations and are inaccurate at endpoints (P1 and P5). Note that the measured stress at endpoint P1 is significantly higher than at other locations. This is different from the small wall results, where the endpoints have von Mises stresses lower than the middle point. As discussed before, the low stress at endpoints in the small wall is due to the limited constraints. One explanation for the high-stress level at one end of the large wall is that, in this case, the heat accumulation effect becomes more important than the boundary constraints and thus alternates the stress distribution.

Since the substrate’s size is comparable with the deposit’s size in the large wall experiment, after being released from the platform of the wire-arc DED machine, the substrate significantly deforms due to the residual stress. We use a laser scanning device shown in Figure 3.22(a), FARO Quantum Max ScanArm, to get the point cloud of the whole structure and compare the distortion with the simulation results. Three longitudinal sections parallel to the YZ-plane are selected for comparison, as shown in Figure 3.22(b). Section A and C only contain the substrate and are 5 mm away from the substrate edge. Section B includes both the deposit and substrate. The deformed shapes of these sections are compared in Figure 3.22(c), where one end of the substrate is fixed to establish a reference configuration. That is why the substrate deforms like a cantilever beam with one end fixed. In the actual case, when placed on a level surface, the middle area of the substrate is in contact with the surface and the four corners curl up.

The similar distortions in Section A, B, and C indicate that most of the deformation occurs in the YZ-plane. The comparison in Section C shows that the temperature-dependent MIS has a good agreement with the scan data, while the constant MIS overestimates. The largest distortion via measurement is 12.45 mm, occurring at the free end of the substrate. The predictions by the constant and temperature-dependent MIS methods are 16.15 mm and 13.43 mm, respectively. Accordingly, the errors are 29.7% and 7.9%. Buchbinder et al. [113] investigated the influence of preheating on structural distortion in selective laser melting (SLM) for aluminum components and reported that increasing the preheating temperature can reduce the distortion in the as-built part. This explains why the temperature-dependent MIS method, where the heat accumulation can be considered as a generalized preheating process, predicts the distortion smaller than the constant MIS. In Figure 3.22(c), the deposit height (in the Z-dir.) in the simulation is smaller than the measurement. That is because we assume a flat top surface for the deposit in the FE model. In reality, the top has a dome shape within the XZ-plane and reaches its highest point in Section C.

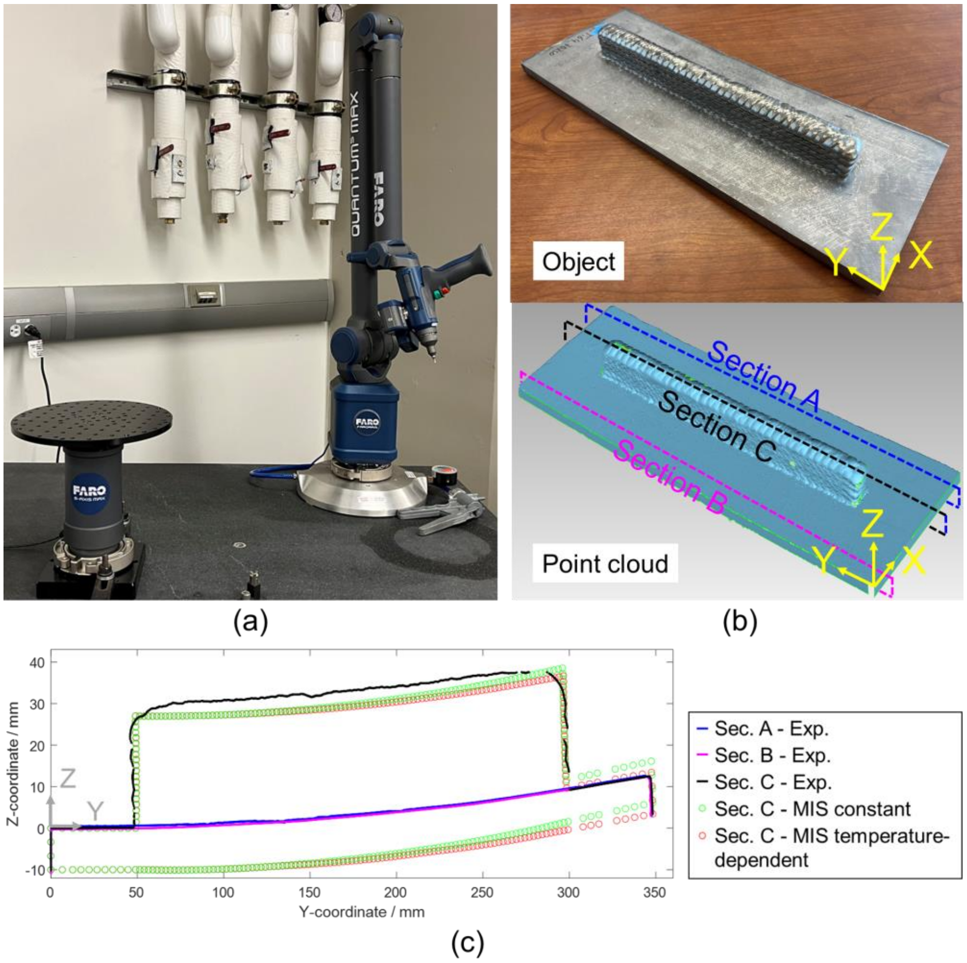

Figure 3.22 (a) FARO Quantum Max ScanArms; (b) real object and the point cloud; (c) comparison of the deformed shape.

3.4.5 Discussion

The XRD measurement in this study employs the $\sin^2\psi$ method. Similar to Ref. [53, 92], we convert the direct XRD results to von Mises stresses and compare them with simulation results for convenience. The measurement uncertainty depends on many factors, such as grain size, sample geometry, incident angle, surface condition, and material anisotropy [114-116]. In this study, the quantitative deviation (values after "±") indicates the fit quality of lattice spacing *d* against $\sin^2\psi$, where ψ is the angle between the normal to the diffracting lattice plane and the sample surface. It is noted that the deviation of the wire-arc DED samples (about ± 100 MPa) is greater than that of the L-PBF samples in Ref. [53] (approximately ± 20 MPa). However, given the large deviations, the temperature-dependent MIS is still considered more accurate than the constant MIS method. For the small wall, the temperature-dependent MIS predicts stresses at all points within the measurement deviation, while the predictions by the constant MIS method are all outside the range (see Figure 3.20). Both methods have similar predictions on P2, P3 and P4 for the large wall, but the temperature-dependent method is far better on P1 and P5 (see Figure 3.21).

To investigate the residual stress distribution along the deposit height, stresses along a vertical line EF on the mid-section of the wall structures are extracted from the MIS-based simulations, as shown in Figure 3.23. Stress results from the detailed process simulation (w/ SSPT) of the small wall are also visualized. For the small wall, the detailed process and MIS-based simulations yield similar results, where the residual stresses are mainly tensile in the deposit and compressive in the substrate. In contrast, the stress variations in the large wall are more complicated. Along the build direction, tensile stresses are present on the substrate bottom, deposit bottom, and deposit top, while compressive stresses occur in the middle of the substrate and deposit. References [117-120] have reported similar residual stress trends to those in the large wall. The difference in residual stress distribution between the small and the large wall is caused by the relatively large substrate of the small wall. Specifically, the small wall has a deposit of 112 × 14 × 27 mm^3 and a substrate of 250 × 250 × 22 mm^3. The large wall has a deposit of 250 × 20 × 27 mm^3 and a substrate of 350 × 120 × 10 mm^3. The large substrate leads to remarkable constraints on the small wall deposit and affects the residual stress distribution.

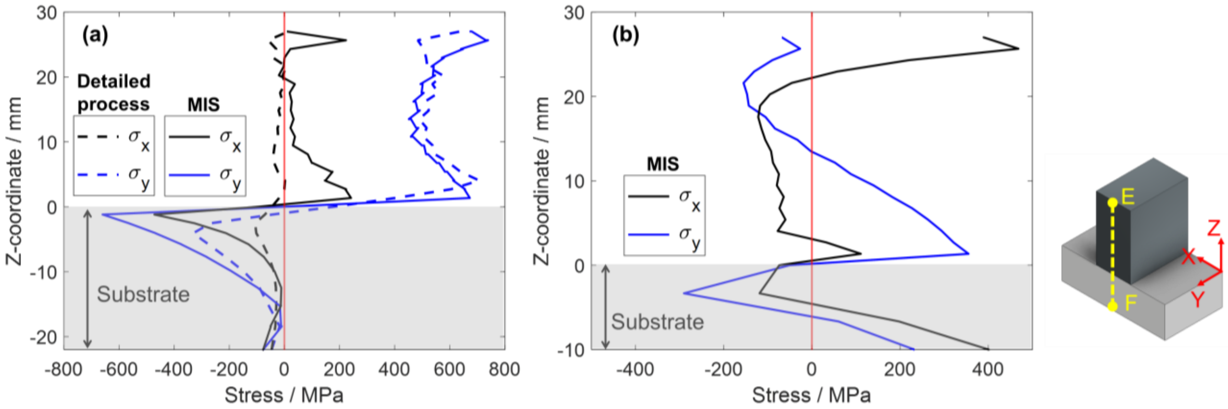

Figure 3.23 Comparison of residual stress distribution along line EF: (a) small wall and (b) large wall.

So far, in the flash heating and MIS-based simulations, each layer is divided into three segments. We perform a sensitivity test to investigate the effect of the number of segments on residual stress and distortion predictions. The von Mises stress at P1 and the maximum distortion in the large wall are selected as indicators for the test, as shown in Figure 3.24. For both indicators, the simulation results become closer to the measurements as the number of segments increases and become stable when the number of segments exceeds three. Therefore, in the current study, using three segments in each layer is proper for residual stress and distortion predictions. In general, the number of segments depends on many factors, such as the dimension and complexity of the deposit, the scanning path of the heat source, and the boundary conditions of the system. The sensitivity test is a good tool for estimating the number of segments.

The computational times and average prediction errors for the constant and temperature-dependent MIS methods are listed in Table 3.3. All simulations are implemented on a workstation (Intel Xeon CPU E5-1650 v4 3.60GHz, RAM 64G) by ANSYS 2020 R1. It shows that the temperature-dependent MIS method gives more accurate predictions at the expense of simulation time compared to the constant MIS method. However, the temperature-dependent MIS method is still much more efficient than the detailed process simulation, e.g., the former takes about 0.5 h to analyze the small wall, which is 13 times faster than the latter (6.5 h).

To summarize, the newly proposed temperature-dependent MIS method has been experimentally validated regarding residual stress and distortion in as-built wire-arc DED parts. The new method, which includes the effect of heat accumulation, has higher prediction accuracy than the previous one.

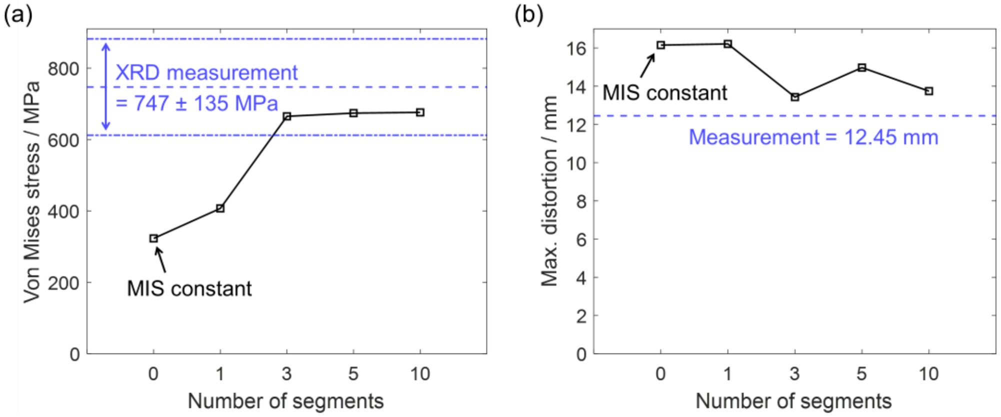

Figure 3.24 Sensitivity test regarding the number of segments in each layer for the temperature-dependent MIS method: (a) von Mises stress at P1 in the large wall; (b) maximum distortion in the large wall. Note that the data point of "zero segment" represents the result from the constant MIS method.

Table 3.3 Computational time and prediction error for the small and large walls

		MIS constant (MIS-based)	MIS temperature-dependent (Flash heating + MIS-based)
Small wall	Computational time	6 min	19 min + 13 min
	Error in von Mises stress	46.5%	8.7%
Large wall	Computational time	4 min	18 min + 13 min
	Error in von Mises stress	19.5%	6.9%
	Error in max. distortion	29.7%	7.9%

3.5 Conclusions

The MIS method was initially proposed for powder DED and L-PBF processes. Constant ISs are applied to all the layers to predict the residual stress and distortion of as-built parts. In this chapter, a temperature-dependent MIS method has been proposed to simulate the wire-arc DED process, where the large part size and extensive energy input lead to significant heat accumulation during the deposition. The difference between the constant and temperature-dependent MIS methods includes: (1) the detailed process simulation is implemented multiple times for different interpass temperatures to obtain corresponding ISs; (2) a part-scale flash heating simulation is added to obtain the interpass temperature for the deposit; (3) the ISs are applied segment-by-segment in the MIS-based simulation to approximate the effect of heat accumulation. Based on the present work, the following points are concluded:

(1) The proposed temperature-dependent MIS method is experimentally validated by two Ti6Al4V walls deposited by wire-arc DED. The results show that the new method has higher accuracy than the constant MIS method. Specifically, the error in residual stress prediction is reduced from 46.5% to 8.7% for the small wall and from 19.5% to 6.9% for the large wall. The error in maximum distortion is reduced from 29.7% to 7.9% for the large wall.

(2) The computational time of the temperature-dependent MIS method increases by five times compared to the constant MIS method. However, it is still an order of magnitude shorter than that of the detailed process simulation using a volumetric moving heat source.

(3) The good agreement in the residual stress profile on the wall ends between simulation and measurement indicates that the new method can reflect not only the influence of heat accumulation but also the deposition path.

(4) The magnitude of ISs decreases as the interpass temperature increases due to smaller thermal gradient.
(5) Including the solid-state phase transformation of Ti6Al4V is able to improve prediction accuracy.

Thus far, the extracted ISs are only applicable to Ti6Al4V deposits manufactured by wire-arc DED with a specific set of process parameters. However, given adequate process parameters and material properties, the proposed MIS method can be used for other metal alloys processed by wire-arc DED.

4.0 Predicting Recoater Interference for L-PBF by Considering Both Global Thermal Deformation and Local Edge Deformation Using the Modified Inherent Strain (MIS) Method

4.1 Current Progress in Prediction of Recoater Interference in L-PBF

A key challenge in the L-PBF process is manufacturing parts with overhanging features. Severe deformation in the build direction, which is vertical to the deposition plane, often accumulates at the edges of overhangs, leading to repeated collisions between the part and the recoating blade [121]. These collisions can be categorized into two types: recoater interference and recoater crash. In common L-PBF systems, as illustrated in Figure 4.1, when the part deformation in the build direction (U_z^{total}) is higher than the powder layer thickness (t_p), it will obstruct the recoater blade along the recoating path. In the case of EOS M290 DMLS whose recoating system is driven by stepper motors, once the blade encounters resistance from the deformed part, the current drawn by the motor would increase to overcome this resistance. If the deformation is minor, the blade continues to move along its path, either further deforming the part or peeling off some material from it, after which the current returns to normal. This phenomenon is referred to as recoater interference. On the other hand, when the part deformation becomes excessively large and creates substantial resistance to the blade, the control system detects a current surge and stops the motor to protect the recoating system. The printer displays an error message and halts the deposition process. This event is called a recoater crash. In practice, both recoater interference and crash should be avoided since they can lead to surface defects, reduced accuracy in part dimensions, build failure, and potential damage to the recoating system [122].

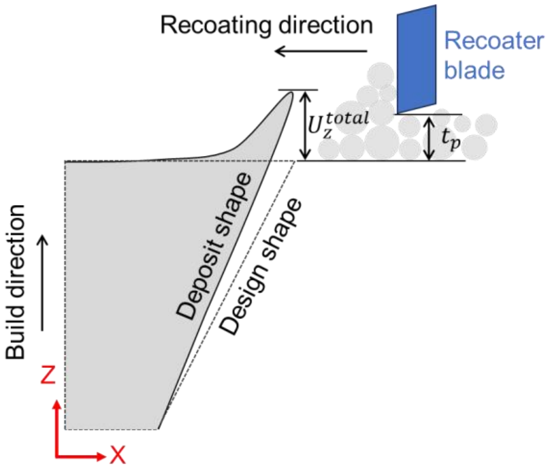

Figure 4.1 Illustration of recoater blade interference in the L-PBF process. U_z^{total} denotes the height difference in the build direction between the elevated overhang edge and the design shape. t_p is the real powder layer thickness. When U_z^{total} exceeds t_p, recoater interference occurs.

In the L-PBF process, the elevation of overhang edges primarily arises from two types of deformation: global thermal deformation (U_z^{global}), driven by relaxation of the thermal stresses induced by the rapid laser melting and solidification over the entire part [123], and local edge deformation (U_z^{local}), which is linked to the behavior of the melt pool near the edges, commonly referred to as the edge effect [124]. The former deformation type causes the entire part, including the overhang region, to distort. Conversely, the latter originates during the solidification of the melt pool near edges and is localized to areas close to the melt pool region [125]. Note that there are other causes for surface elevation in L-PBF, such as large splashes falling on the top surface of the deposit and delamination or cracking of the deposit [126].

Both global and local deformations are influenced by various design and process-related factors. These include the overhang angle and material selection [121, 127, 128], volumetric energy density [121, 129-131], rotation angle of the scanning direction between two consecutive layers [129], scanning strategy [127, 132], build direction [133], use of contour scan [130], and implementation of remelting [129]. In response to the diverse impacts of these factors, several researchers have proposed methods to mitigate overhang deformation. Yuan and Chen [134] introduced an innovative technique that involves altering the laser spot size through defocus control for the supportless fabrication of overhangs. Yeung et al. [135] developed a dynamic power control strategy for the laser spot when scanning overhang areas. Cheng and Chou [136, 137], Ameen et al. [138], and Kayacan et al. [139] have each suggested various support designs targeted at improving heat transfer within the overhang region, thus minimizing the warping caused by thermal stress.

Besides efforts to reduce overhang deformations, several researchers have focused on in-situ monitoring techniques for detecting recoater interference and crashes. Liu et al. [140, 141] developed an infrared thermography method to measure powder layer thickness after each recoating, capable of detecting potential recoater interference up to 8 to 10 layers in advance. Scime et al. [142] introduced a computer vision algorithm based on unsupervised machine learning, designed to identify and classify anomalies during the powder spreading, such as recoater hopping, streaking, and super elevation. Similarly, Fischer et al. [143] and Jacobsmühlen et al. [144] developed their deep learning models for detecting elevated regions.

In addition to in-situ monitoring, identifying potential recoater interference and crash during the design stage is crucial. Peter et al. [145] tested various commercial FE software packages, including ANSYS, Autodesk, MSC, Additive Works, and Atlas3D, for their ability to predict recoater crashes using two test geometries. However, the results were inconclusive since all software demonstrated some prediction error. Lu et al. [146] simulated recoater interference in numerical models by applying a virtual body force parallel to the powder spreading direction, though the magnitude of this force requires case-by-case calibration. Kamat and Pei [147] treated the overhang as a multilayer cantilever beam and used the Euler-Bernoulli beam theory to calculate deformation on the down-facing surface. This method, however, necessitates coefficient calibration and neglects the impact of process parameters and plastic deformation of the material. Yavari et al. [122] and Kobir et al. [148, 149] employed graph-theory-based simulations to predict recoater crashes when the build direction deformation of an area exceeds the solid layer thickness. It is important to note that the aforementioned simulation works primarily consider the global thermal deformation of the overhang, and due to limitations in model fidelity at the part scale, the edge effect is not included.

As will be discussed later, recoater interference is a necessary condition for a recoater crash but not a sufficient one. Additionally, the occurrence of a recoater crash is highly uncertain [145]. Therefore, our primary focus in this research is on predicting recoater interference. We propose an integrated numerical and experimental framework to predict the recoater interference in L-PBF processes for overhang structures. We extend the MIS method by introducing location-dependent ISs to predict the global thermal deformation of overhang structures. Additionally, we conduct experiments to explore the relationship between powder and solid layer thickness and, for the first time, estimate the local edge deformation by corroborating numerical simulation with experimental measurement.

4.2 Framework for Predicting Recoater Interference

Figure 4.2 outlines the flowchart of the proposed framework for predicting recoater interference. The criterion for interference in a part with n deposited layers is when the total deformation in the build direction U_z^{total} at any point on the top surface of the edge exceeds the real powder layer thickness t_p:

$$U_z^{total} > t_p \tag{4.1}$$

Note that the real powder layer thickness at a given layer is not the same as the printer's input layer thickness and thus will be obtained *a priori* through the so-called "staircase" experiment, which is a series of columns printed with a consecutive number of layers. If the above criterion is not met for the *n*th layer, the assessment continues in a layer-by-layer fashion until recoater interference is detected or the deposition ends.

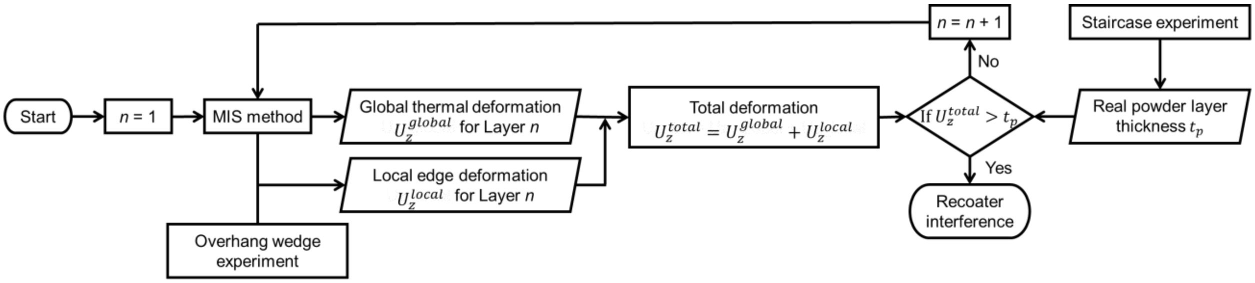

Figure 4.2 Flowchart of the framework for predicting the recoater interference.

The total build-directional deformation U_z^{total} on the top surface at the overhang edge is postulated to be the sum of two terms:

$$U_z^{total} = U_z^{global} + U_z^{local} \tag{4.2}$$

where U_z^{global} represents the global thermal deformation which is calculated directly by the MIS method and U_z^{local} denotes the local edge deformation which will be determined *a priori*. Specifically, its value is taken as the difference between U_z^{total} obtained from experimental measurement and U_z^{global} obtained from MIS simulation for overhang wedges with various angles.

4.3 Location-dependent MIS Method

In previous works employing the MIS method [29, 48, 49, 58], the deposit in the detailed process simulation is typically modeled as a block comprising three to five layers. The ISs are derived by averaging values from a stabilized region, often located at the core of the deposit, to reduce the impact of boundary effects. In the subsequent part-scale simulations, the averaged ISs are uniformly applied to the FE model, meaning that areas near edges or surfaces are assigned the same ISs as internal regions. This procedure neglects the IS features in boundary regions and may lead to significant errors in predicting residual stress and deformation within these regions.

In this study, we emphasize the importance of accounting for IS variations in boundary regions, particularly given our focus on investigating deformation near overhang edges. Accordingly, we make two modifications to the MIS method: (1) in the detailed process simulation, the deposit is modeled with an overhang region to capture IS variations within that area, and (2) in the part-scale simulation, we use location-dependent ISs rather than constant ones throughout the entire part. All simulations in this chapter are carried out using ANSYS 2021R1 with the Ansys Parametric Design Language (APDL).

4.4 Experiment

4.4.1 Overview

Four types of structures—staircase, overhang wedge, canonical part, and table—are investigated in this study, and their geometries are illustrated in Figure 4.3. The staircases are used to study the thickness of newly applied powder layers. The overhang wedges are employed to validate the proposed location-dependent MIS method and estimate the local edge deformation term. The canonical parts and tables are utilized as validation cases.

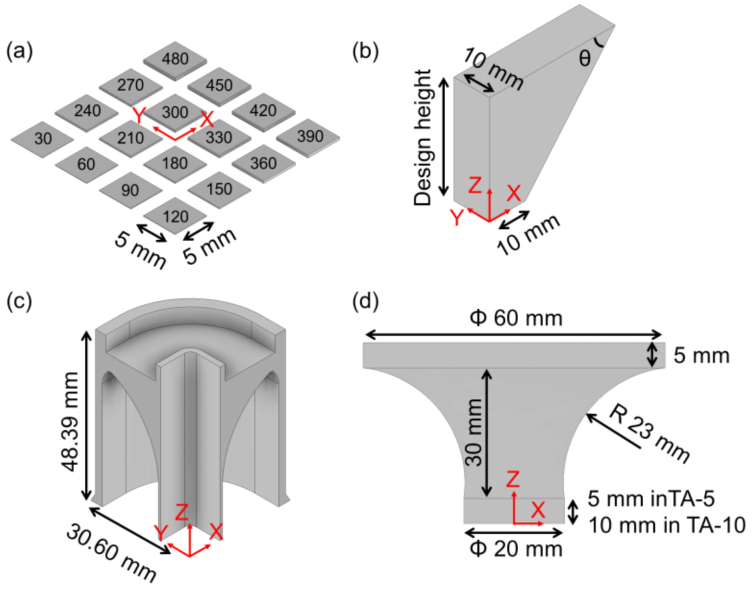

Figure 4.3 Geometries of the printed samples: (a) staircase (the number in the center of each step represents its design height in microns), (b) overhang wedge, (c) canonical part (quarter view), (d) table. The build direction is along the positive Z-axis.

All samples in this chapter are deposited using 316L stainless steel on an EOS M290 DMLS system with process parameters listed in Table 4.1. A recoater equipped with a steel blade is used to apply a new layer of powder. The 316L powder, manufactured by Praxair Surface

Technologies, Inc., has a packing density of 4 g/cm^3. The particle size distribution is measured to have d_{10} = 18 µm, d_{50} = 31 µm, and d_{90} = 49.3 µm according to ASTM B822.

In-situ video recording is employed to monitor the recoating anomaly during the deposition of overhang wedges. For this purpose, a Logitech Brio webcam is placed on a tripod outside the EOS machine chamber and directed toward the printing plane. The as-built deformation of samples is measured using an 8-axis Quantum Max (S Model) FaroArm laser scanning system. It is equipped with a FAROBlu Max (xP) laser line probe, which offers a high measurement accuracy of 15 µm [150].

Table 4.1 Process parameters for 316L on EOS M290

Parameter	Value
Laser power	195 W
Scanning velocity	1083 mm/s
Solid layer thickness	30 µm
Hatch spacing	90 µm
Stripe width	5 mm
Stripe overlap	0.12 mm
Laser rotation angle	66.7°

4.4.2 Staircase

Eight staircase samples are printed on four separate build plates. Each staircase sample consists of multiple independent steps with an area of 5 mm × 5 mm, as depicted in Figure 4.3(a). The height of these steps across all samples ranges from the thickness of one layer to that of 42 layers. Here, the layer thickness refers to the nominal (input) solid layer thickness of 30 µm, as listed in Table 4.1. Detailed information about the staircase samples is provided in Table 4.2. Note that the highest steps in SC5 and SC6 are intended to be 42 nominal solid layer thicknesses, but only 41 layers are deposited due to geometrical errors induced during the slicing process. After printing, all the staircase samples are scanned using the FaroArm to measure the height of each step.

It should be noted that many researchers have adopted similar experimental designs to investigate the powder and solid layer thickness in L-PBF processes [151-154]. Their reports indicate that the powder layer thickness depends on various factors, including process parameters, materials, and even printer brands, and may vary from case to case. That is why we repeat this experiment to determine the specific powder layer thickness rather than using data from other literature.

Table 4.2 Information of the printed staircases

Build plate No.	Sample No.	Number of steps	Step height in terms of the number of nominal solid layers
SC-BP1	SC1	16	1, 2, …, 15, 16
	SC2	16	1, 2, …, 15, 16
SC-BP2	SC3	16	1, 2, …, 15, 16
	SC4	16	1, 2, …, 15, 16
SC-BP3	SC5	36	1, 2, …, 29, 30, 32, 34, 36, 38, 40, 41
	SC6	36	1, 2, …, 29, 30, 32, 34, 36, 38, 40, 41
SC-BP4	SC7	36	1, 2, …, 29, 30, 32, 34, 36, 38, 40, 42
	SC8	36	1, 2, …, 29, 30, 32, 34, 36, 38, 40, 42

4.4.3 Overhang Wedge

The overhang wedge, shown in Figure 4.3(b), has a constant overhang angle (θ) ranging from 25° to 70°. The samples are printed on five separate build plates. On each build plate, the samples are distributed diagonally to avoid multiple simultaneous contacts with the recoater blade and to facilitate the identification of any failed part in the event of a recoater crash. Additionally, to prevent long contact lines between the part and the recoater blade, the long side of the overhangs are tilted at a 15° angle from the recoating direction in accordance with common design for additive manufacturing (DFAM) guidelines.

Some overhangs experience recoater crashes during the printing and others are successfully printed. If a recoater crash occurs, the affected part will be removed from the queue and the L-PBF system will be restarted to continue producing the remaining parts. The build height where a recoater crash occurs is recorded.

Table 4.3 lists the overhang samples on each build plate. The sample number is explained as follows: the two-digit number immediately after 'OH' represents the overhang angle θ in degrees, and the number after the dash symbol indicates the sample's design height in millimeters. For example, 'OH25-30' means the structure has an overhang angle of 25° and a design height of 30 mm, and 'OH60-6.0' corresponds to a 60° overhang sample with a design height of 6 mm. The design height is reached for completed samples but not for failed ones. The values in parentheses following the failed sample indicate the failure height in millimeters.

Table 4.3 Information of the printed overhang wedges

Build plate No.	Sample No.	
	Failed	Completed
OH-BP1	OH25-30 (2.85), OH30-30 (4.62), OH35-30 (6.42)	OH40-30, OH45-30, OH50-30 OH55-30, OH60-30-30, OH65-30, OH70-30
OH-BP2	OH25-30 (3.24), OH30-30 (3.12), OH35-30 (6.60)	None
OH-BP3	OH25-30 (2.64), OH30-30 (3.48), OH35-30 (6.84)	OH40-30
OH-BP4	OH40-30 (14.28)	OH45-30, OH50-30 OH55-30, OH60-30, OH65-30, OH70-30
OH-BP5	OH25-1.5 (1.23)	OH25-2.0, OH30-1.5, OH30-2.0, OH35-2.0, OH35-3.0, OH35-4.0, OH50-2.0, OH50-4.0, OH50-6.0, OH60-2.0, OH60-4.0, OH60-6.0

4.4.4 Canonical Part and Table

The canonical part and table have varying overhang angles with increased height, as shown in Figure 4.3(c) and (d). Specifically, from bottom to top, θ varies from 90° to 24.5° in the canonical part and 90° to 7° in the table in the design. Table 4.4 lists the details of printed canonical and table specimens. CA-100 represents a specimen with 100% of the design height, 48.39 mm. Taking this height as a reference, CA-60, CA-72, and CA-76 denote the specimens with 60%, 72%, and 76% of the design height, respectively. For example, CA-60 has the same geometry as CA-100 with heights between 0 and 48.38×60% = 29.03 mm. On build plate CT-BP2, one additional CA-100 and two table specimens, TA-5 and TA-10, are printed. The overhang sections in these two table samples are identical. The difference lies in their bases: TA-5 has a 5 mm high cylinder base, whereas TA-10 has a 10 mm base. These designs aim to minimize the interaction effect between their respective recoater crashes. The failure heights in millimeters and the corresponding overhang angles are listed in parentheses following the failed specimens. The recoater crash height of TA-10 is subtracted by 5 mm to allow comparison with the failure height of TA-5. In the subsequent sections, the computer simulation of the table specimen will use only the geometry of TA-5.

Table 4.4 Information of the canonical parts and tables

Build plate No.	Sample No.	
	Failed	Completed
CT-BP1	CA-100 (37.86, θ = 29.5°)	CA-60, CA-72, CA-76
CT-BP2	CA-100 (37.50, θ = 31.0°) TA-5 (28.08, θ = 30.0°) TA-10 (32.85-5.00 = 28.85, θ = 26.0°)	None

4.5 Results and Discussion

4.5.1 Determination of the Powder Layer Thickness

Figure 4.4 schematically illustrates the transition from a powder layer to a solid layer in terms of thickness in common L-PBF processes. In the figure, t_{pn} and t_{sn} denote the powder and solid layer thickness of the *n*th layer, respectively.

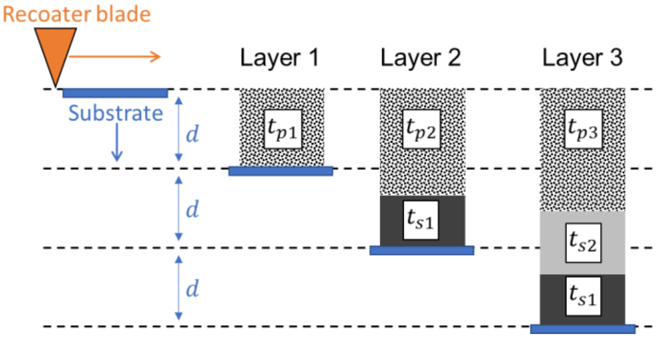

Figure 4.4 Schematic of the powder and solid layer thickness evolution in common L-PBF processes. t_{pn} and t_{sn} respectively represent the layer thickness of powder and resolidified deposit for Layer *n*. (Adapted from Ref. [151])

For each layer, the substrate descends a constant distance *d*, a process parameter that users can control. For Layer 1, the powder layer thickness is $t_{p1} = d$. After melting and solidification, the solid deposit shrinks, resulting in a layer thickness of t_{s1}. For layer 2, the substrate is lowered by d again, and the powder layer thickness becomes $t_{p2} = 2d - t_{s1}$. Likewise, for Layer 3, the powder layer thickness is calculated as $t_{p3} = 3d - t_{s2} - t_{s1}$. As illustrated in Ref. [151], the powder and solid layer thickness for Layer *n* can be expressed as:

$$t_{pn} = \frac{d}{c}[1 - (1 - c)^n] \tag{4.3}$$

$$t_{sn} = d[1 - (1 - c)^n] \tag{4.4}$$

where $c = t_{sn}/t_{pn}$ represents the relative layer thickness of a solid layer with respect to a powder layer. In this study, c is considered constant. As the number of deposited layers increases, the limits of t_{pn} and t_{sn} are found to be:

$$\lim_{n\to\infty} t_{pn} = \frac{d}{c} \tag{4.5}$$

$$\lim_{n\to\infty} t_{sn} = d \tag{4.6}$$

The above equations indicate that the powder and solid layer thickness become steady as the deposition proceeds, approaching d/c and d, respectively. d is actually the nominal (input) solid layer thickness and is set to be 30 μm in this study, as listed in Table 4.1. According to Eq. (4.4), the height of an n-layer deposit is calculated as:

$$S_n = \sum_{i}^{n} t_{si} = nd + \frac{d}{c}\,[c - 1 + (1-c)^{n+1}] \tag{4.7}$$

The relative thickness c, along with the powder layer thickness t_{pn}, can be determined using the staircase experiment. First, we measure the height of each step in the staircase samples to obtain a series of data points (n, S_n), where n represents the number of nominal solid layers that a step has and S_n is the deposit height of that step. Then, we estimate c through curve fitting using these data points according to Eq. (4.7).

Figure 4.5(a) shows the staircase SC1 as an example. Other samples are not displayed since their appearances are similar to SC1. Figure 4.5(b) presents the top surface topography of SC1, illustrating the height variation of individual steps. The scanned point cloud data are averaged over a 1 mm^2 square at the center of each step (as indicated by white dashed lines in Figure 4.5(b)) to determine the step height S_n. Curve fitting is performed in MATLAB using the `fit` function. The results are displayed in Figure 4.5(c), where 'EXP - SCATTER' denotes the (n, S_n) data point, ‘FIT’ represents the fitted line, ‘DESCENT’ is the descent distance of the substrate calculated by *nd*, and ‘FIT - 95% CI’ is the 95% confidence interval (CI) of the fitted curve. The mean relative thickness is $c = 0.316$. A very similar value of 0.3 for 316L is reported in Ref. [151].

Figure 4.5(d) illustrates the variations in powder and solid layer thicknesses as the deposited layer number n increases. In the plot, ‘EXP - AVG’ denotes the measured average value, and ‘ANA’ represents the analytical solution calculated by Eq. (4.3) for powder layer thickness and Eq. (4.4) for solid layer thickness. The shaded area labeled ‘ANA - 95% CI’ indicates the uncertainty of fitted relative thickness c. Overall, the experimental data for both the solid and powder layer thicknesses closely align with the trends of the analytical curves. It is observed that the powder and solid layer thicknesses converge rapidly and become stable after approximately ten layers of deposition. Table 4.5 summarizes the results of the staircase experiment. In the following sections, the real powder layer thickness of 95 µm is considered as the critical threshold for identifying the recoater interference, as mentioned in Section 4.2.

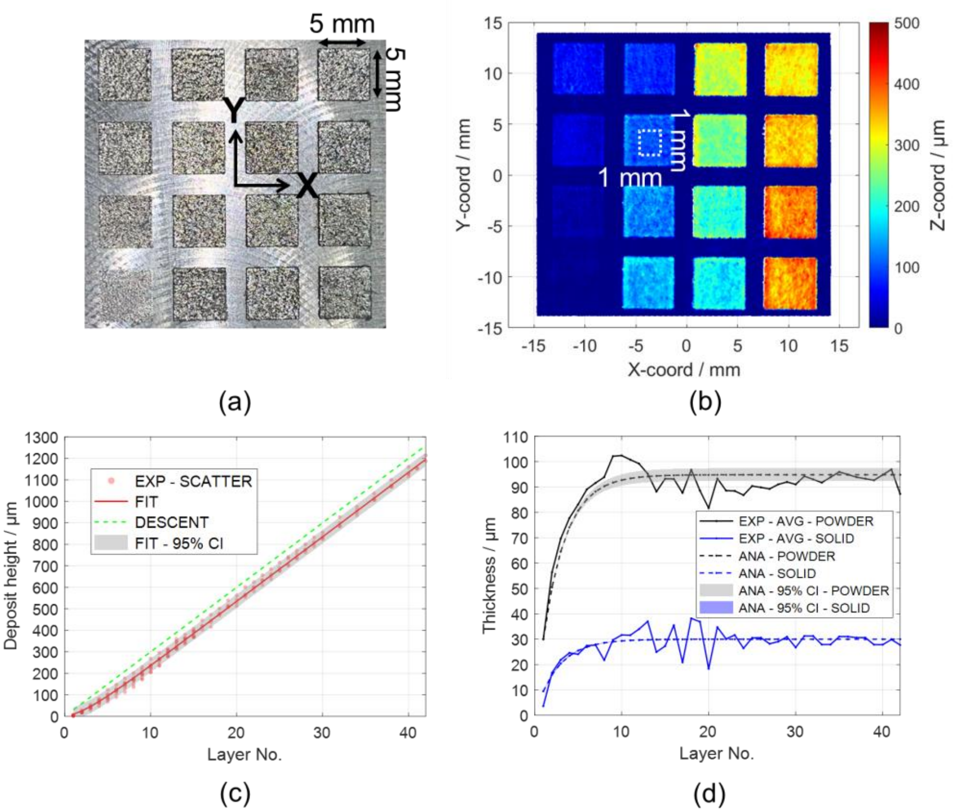

Figure 4.5 (a) As-built staircase SC1; (b) top surface topography of SC1; (c) curve fitting results of the staircase samples, where 'EXP - SCATTER' denotes the (n, S_n) data points, 'FIT' represents the fitted line, 'DESCENT' is the descent distance of the substrate calculated by *nd*, and 'FIT - 95% CI' is the 95% confidence interval of the fitted curve; (d) variations in powder and solid layer thicknesses, where 'EXP - AVG' denotes the measured average value, 'ANA' represents the analytical solution calculated by Eq. (4.3) and Eq. (4.4), and 'ANA - 95% CI' indicates the uncertainty of fitted relative thickness *c*.

Table 4.5 Results of the staircase experiment

	Average	95% confidence interval
Relative thickness c	0.316	(0.308, 0.325)
Powder layer thickness $t_p = d/c$	95 µm	(92 µm, 98 µm)

4.5.2 Experimental Investigation on Deformation of Overhang Wedges

Figure 4.6(a) displays the as-built overhang wedges on build plate OH-BP1 (refer to Table 4.3). The other build plates are not shown as they look similar to this one. The failure heights listed in Table 4.3 reveal two key observations. First, identical design geometries can fail at different heights in repeated experiments. For instance, OH25 fails at 2.85 mm, 3.24 mm, 2.64 mm, and 1.23 mm in five separate builds. Second, successfully printed geometries without a recoater crash in one experiment might fail in others. An example is OH40, which is completed on build plates OH-BP1 and OH-BP3 but fails at 14.28 mm on OH-BP4. These observations underscore the considerable uncertainty associated with recoater crashes.

Figure 4.6(b) illustrates the details of the failed specimens on build plate OH-BP1. When a specimen stops the recoating blade, its overhang tip has become severely deformed, and some materials have chipped off from the tip, presumably due to repeated recoater interference prior to recoater crash. During the overhang printings, scratching sounds are heard repeatedly long before the recoater crash.

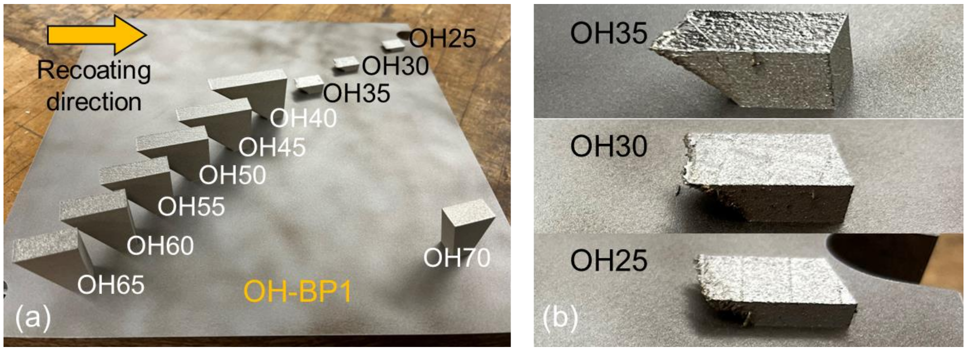

Figure 4.6 On build plate OH-BP1: (a) as-built overhang wedges; (b) details of the failed samples

To identify the occurrence of recoater interference in the experiment, a webcam is installed to monitor the printing process of build plate OH-BP4. Figure 4.7(a) presents a snapshot captured just before the recoater applies a new powder layer onto the already deposited part. At this point, the recoater blade is positioned on the right side of the snapshot, preparing to move to the left. Figure 4.7(b) shows a snapshot taken immediately after the recoater has spread the new powder layer. In areas where the top surface of the deposit is significantly elevated, the powder thickness should also be noticeably less than in other areas. This difference in powder thickness is challenging to discern with the naked eye in the original color images taken after each layer's recoating, like Figure 4.7(b). To address this, we utilize MATLAB for image post-processing. The color images are first converted to grayscale images via the `rgb2gray` function and then to black-and-white ones through the `imbinarize` function with an adaptive threshold and a sensitivity factor of 0.57. The post-processing focuses on a region of interest (ROI) predominantly covered by powders after recoating.

The binarized images after post-processing are shown in Figure 4.7(c), where the white pixels or segments suggest the elevated areas and the black background represents normal areas. The significantly elevated areas are only observed in OH40, OH45, and OH50 samples, among which OH45 and OH50 do not experience recoater crashes. To quantitatively analyze the change of these elevated areas as the deposit height increases, we measure the image intensity in the near-tip region of OH40, OH45, and OH50. In the black-and-white images, a white pixel signifies an intensity of 1, and a black pixel represents 0. The results are depicted in Figure 4.8. These intensity curves terminate at the height of 14.28 mm, at which the recoater crash occurs on OH40.

Figure 4.8 shows that, overall, the image intensity tends to increase with build height. However, several local fluctuations are also observed, indicating a high likelihood of recoater interference. As previously mentioned, when recoater interference occurs, the recoater blade either distorts the elevated area or removes some material from the part for it to pass through, thereby reducing the extent of distortion in the build direction. Consequently, in the following layers, the image intensity might decrease. A notable instance of this pattern is observable in Figure 4.7(c), where elevated areas are detected in OH50 at Layer 249 but not at Layer 250. As the printing process continues, the build-directional deformation accumulates, causing the elevated region to re-emerge and image intensity to increase again. This pattern can be found in both successfully printed overhangs like OH45 and OH50 and failed overhangs like OH40.

Recoater interference may occur multiple times during the deposition, so recognizing its initial occurrence is crucial. We determine a critical point P on the intensity curve for OH40, as shown in Figure 4.8. Up until this point, the intensity starts at zero and gradually increases. After this point, a significant change in the rate of intensity increase is observed, suggesting the first occurrence of recoater interference for OH40. The corresponding part height at P is 1.5 mm. In the zoomed-in section in Figure 4.8, the first intensity peaks for OH45 and OH50 also appear to reflect the initial interference. However, the data from these two samples are not used due to their relatively low intensities: the maximum intensities for OH45 and OH50 are only 17% and 5% of the maximum intensity for OH40, respectively.

With OH40 failing due to a recoater crash at 14.28 mm, the initial interference at the height of 1.5 mm implies that recoater interference starts early in the deposition process, approximately after 50 layers. This finding agrees with the fact that scratching sounds during printing have been heard long before the crash. In the following sections, we will utilize this initial interference height of 1.5 mm to estimate the local edge deformation.

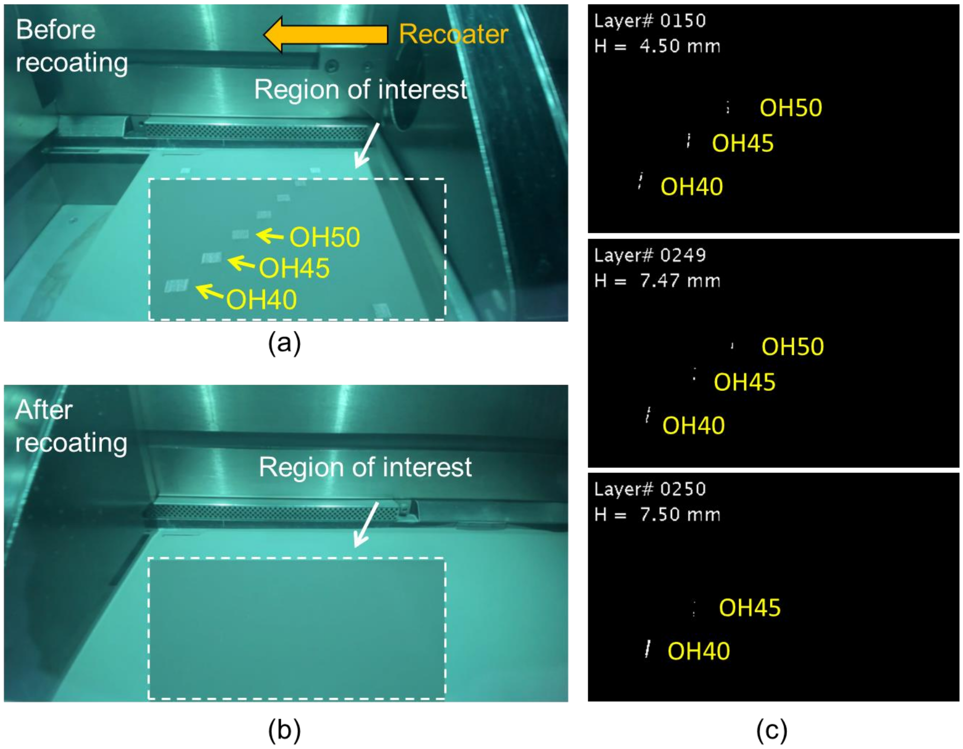

Figure 4.7 (a) Snapshot right before the recoater delivers a new layer of powder; (b) snapshot immediately after the recoater delivers a new layer of powder; (c) binarized images of the ROI at different deposition heights, where the white pixels or segments suggest the elevated areas and the black background represents normal areas.

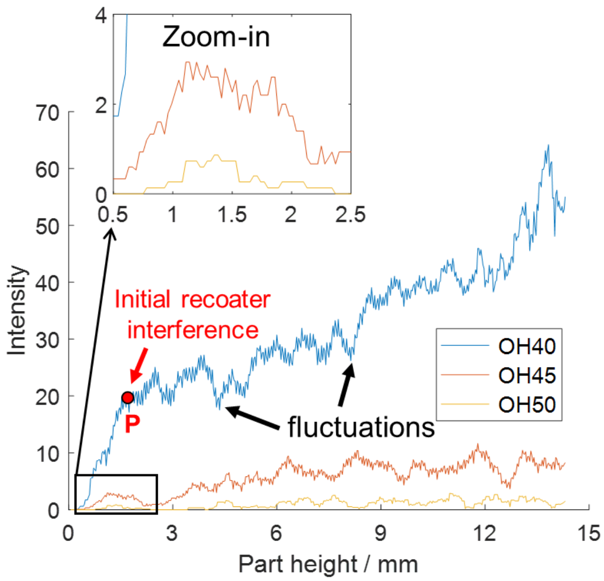

Figure 4.8 Intensity variation of OH40, OH45, and OH50 around overhang edge.

4.5.3 Validation of the Location-dependent MIS Method

To investigate the location dependence of the ISs, we employ four FE models with different overhang angles, θ = 25°, 45°, 70°, and 90°, in the detailed process simulation. Among them, the 90° overhang means a block deposit. Each model includes a four-layer deposit and a substrate representing the previously deposited material, as shown in Figure 4.9. The deposit measures 400 µm in width (Y-direction) and 120 µm in height (Z-direction), with each layer being 30 µm thick. The deposit length (X-direction) is 400 µm for the bottom layer and varies for the higher layers to form different overhang angles. The length difference between two consecutive layers is calculated by $\mathrm{d}L = t/\tan\theta$, where t is the solid layer thickness and θ is the overhang angle. The Goldak heat source, simulating the laser spot in the real printing process, alternates the scanning direction by 180° after each track and rotates by 66.7° after each layer. The parameters used in the Goldak heat source are the same as in Ref. [59]. The mesh size for the deposit is approximately 15 µm, while that for the substrate is coarser to save computational time. The element type is SOLID278 in the thermal analysis and SOLID185 in the mechanical analysis. The boundary conditions employed here are consistent with those in Ref. [59].

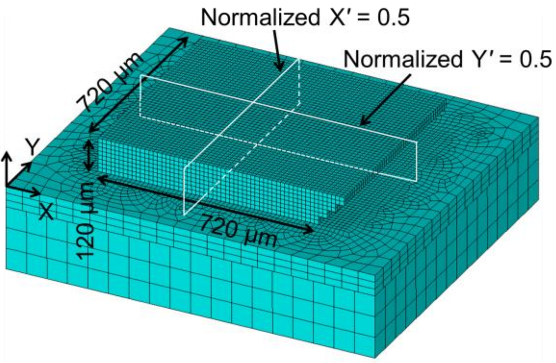

Figure 4.9 FE model of 45° overhang for the detailed process simulation

After the detailed process simulation, ISs are calculated element by element within the deposit. Note that the length in the X-direction of each layer in the four FE models is not the same due to different $\mathrm{d}L$. To conveniently present and compare the distribution of ISs, we normalize the X and Y dimensions of each deposit layer to be between 0 and 1. In the build direction (Z-direction), the ISs for elements that share the same normalized X and Y coordinates (X′ and Y′) are averaged over the two middle layers (excluding the bottom and top layers) to include the interlayer effect. We assume the ISs are constant throughout the build direction.

Figure 4.10 displays the normalized IS distributions on two orthogonal planes X′ = 0.5 and Y′ = 0.5, which are marked with white boxes in Figure 4.9. It can be observed in Figure 4.10 that, on both planes, the ISs are stable in the middle and vary at the two ends. Due to their orthogonality, the IS patterns of the X- and Y-components are reversed between the planes at X′ = 0.5 and Y′ = 0.5.

In Figure 4.10(a), the IS distributions in the block deposit (θ = 90°) are almost symmetrical with respect to X′ = 0.5. The stable region extends approximately from X′ = 0.2 to X′ = 0.8, accounting for 60% of the entire region. The IS distributions in the 25°, 45°, and 70° overhangs exhibit a certain asymmetry with respect to X′ = 0.5. Within the region from X′ = 0 to 0.6, the ISs of these overhangs essentially align with those of the block deposit. The primary difference is that the Z-component IS curves of the overhangs are lower than that of the block deposit. The X- and Z-component of ISs in the overhangs begin to decrease starting from X′ = 0.6 and have significantly lower values than those in the block deposit at X′ = 1.0. Note that the Y-component ISs in the overhangs still closely resemble those in the block deposit between X′ = 0.6 and 1.0. In Figure 4.10(b), the IS distributions for all the structures are symmetrical with respect to Y′ = 0.5, further confirming that the asymmetry in Figure 4.10(a) is caused by the overhang feature.

The 25°, 45°, and 70° overhangs exhibit IS distributions that are markedly different from those of the block deposit. This difference underscores the necessity of accounting for overhang features in the detailed process simulations in cases where the investigated part-scale component has overhangs. However, the results also indicate minor variations in IS distributions among these overhang angles. This observation suggests that the current level of modeling fidelity in detailed process simulations may not be sufficient to effectively distinguish the influence of different overhang angles on IS distributions. Therefore, in this study, the ISs used in the part-scale simulation are the average of all the overhang models (θ = 25°, 45°, 70°).

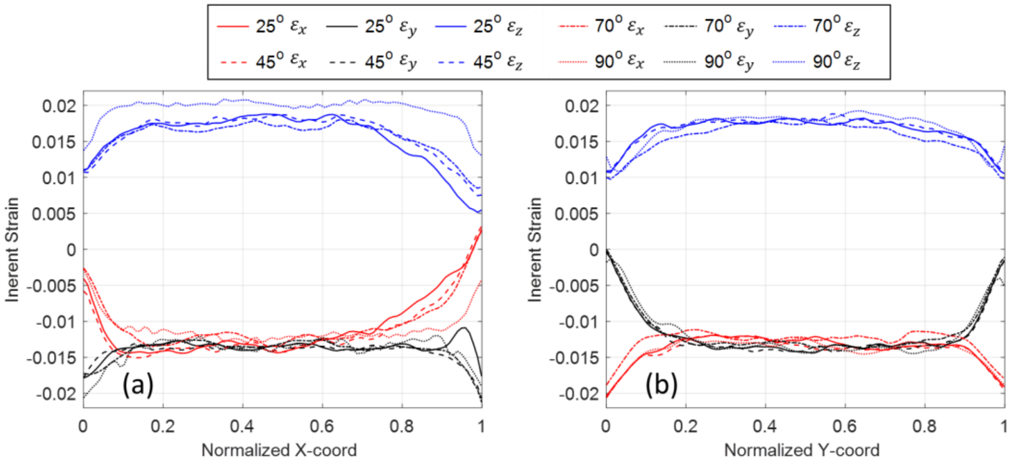

Figure 4.10 Normalized IS distributions on (a) plane Y′ = 0.5 and (b) plan X′ = 0.5. Note that the overhangs are along the X-direction from X′ = 0 towards X′ = 1. The θ = 90° denotes a block deposit with no overhang feature.

After getting the ISs from the detailed process simulation, the MIS-based part-scale simulation is implemented to predict the overhang deformation. As depicted in Figure 4.11(a), the FE model of the overhang wedge in the MIS-based simulation has a similar Cartesian coordinates system (OXYZ) as in the detailed process simulation. Each equivalent (lumped) layer to which the ISs are applied has its local coordinate system O′X′Y′Z′ that aligns with the global OXYZ and normalizes the layer length in the X′ direction to 1. Figure 4.11(b) illustrates the IS distributions along the X′ direction for each equivalent layer. These distributions are piecewise linear approximations to those in Figure 4.10(a). The IS distributions along the Y′ direction are assumed to be uniform. This assumption is justified by the fact that (1) we focus on the distortion within the mid-plane (parallel to the XZ-plane) of an overhang structure and (2) IS distributions along the Y direction, as shown in Figure 4.10(b), are stable near the mid-plane. In the MIS-based simulations, we assign ISs as thermal strains to each lumped layer via ANSYS user-defined field variables. The ISs are loaded by increasing the layer temperature by one degree.

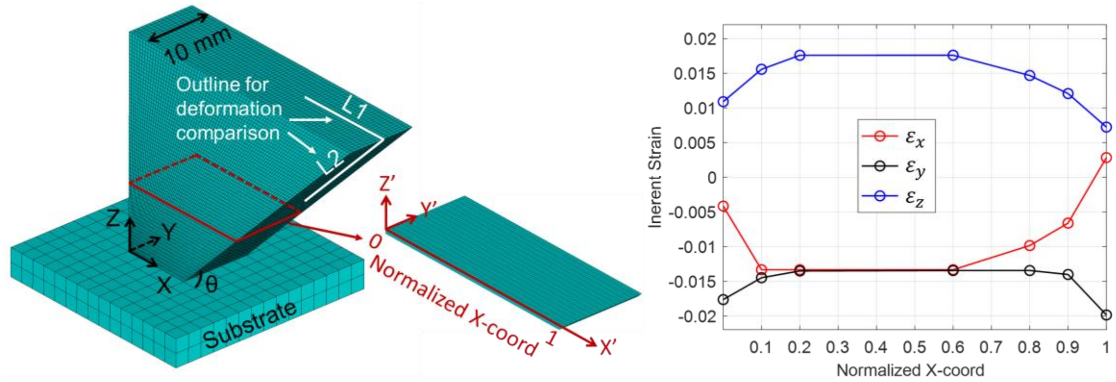

(a) (b)

Figure 4.11 Implementation of ISs in the part-scale MIS simulation.

The MIS method is employed to predict the deformation of successfully printed overhangs with θ = 45°, 50°, 55°, 60°, 65° and 70° to verify its validity. To compare the deformation results, we select two outlines on the mid-plane near the overhang tip: L1 on the top surface and L2 on the down-facing surface (see Figure 4.11(a)). These two lines intersect at the overhang tip, and their lengths are calculated as L1 = 20 mm / tanθ, L2 = 20 mm / sinθ. The deformed shapes of these outlines, as measured from the build plate OH-BP4, predicted by the MIS method with both constant and location-dependent ISs, and calculated by analytical equations derived in Ref. [147], are visualized in Figure 4.12. For clarity, the displayed deformation from all sources is scaled up in all directions by a factor of ten (×10). The legends in Figure 4.12 are explained as follows:

‘DESIGN’ represents the design shape of the overhang, ‘EXP-SCATTER’ denotes the scanned point cloud data, ‘MIS-CONST’ and ‘MIS-VAR’ represent the results predicted by the MIS method with constant and location-dependent ISs, respectively, and ‘ANA’ corresponds to the analytical solution proposed in Ref. [147]. The analytical solution assumes that the overhang is a cantilever beam with small deflections which follows the Euler-Bernoulli beam theory. This approach requires a coefficient *m*, defined as the ratio of melt penetration depth to the solid layer thickness, that must be calibrated experimentally. We calibrate this coefficient using measured data from OH45 and apply it to other overhangs.

Figure 4.12 shows that deformations predicted by the MIS method with location-dependent ISs are more accurate than those with constant ISs. The measured point cloud data on L2 deviates significantly from the trends predicted by the simulations and analytical solutions when Z < 15 mm, possibly due to measurement errors. When using a laser scanning device to measure the deformation, the laser beam should be as perpendicular to the object’s surface as possible to maintain a low signal-to-noise ratio [155]. The overhang wedges are measured while still attached to the build plate. When measuring the lower region of their down-facing surfaces, the limited operational space causes the laser beam to become almost parallel to these surfaces, leading to increased measurement errors. Therefore, we consider the measured deformation with Z < 15 mm as unreliable.

Figure 4.13 displays the total deformation on L2 on the down-facing surface. Legends in Figure 4.13 that do not appear in Figure 4.12 are explained as follows: ‘EXP - FIT’ is the fitted curve based on the point cloud data, and ‘EXP - 95% CI’ represents the 95% CI of the fitted curve. In general, the distortion pattern on the down-facing surface follows a specific trend: as the deposited height increases, the distortion initially rises and gradually reaches a maximum and then begins to decrease [147]. The measured data confirms this trend, and all the prediction methods can capture it, as illustrated in Figure 4.13. For example, the peak distortion in OH45 occurs at approximately Z = 20 mm. Below this height, distortion increases with build height, whereas above this point, it decreases as the height continues to grow.

Figure 4.13 reveals that, among the various analytical and numerical methods, the MIS method with constant ISs shows the lowest accuracy and significantly overestimates the distortion on L2. In contrast, both the analytical solution and the MIS method with location-dependent ISs align more closely with the scanning data. It is worth noting that although the analytical solution matches the accuracy of the location-dependent MIS method, the analytical solution requires coefficient calibration as the value of this coefficient is dependent on material properties, process parameters, and even part geometries [147]. Table 4.6 lists the mean absolute error between the measurement and the prediction of two MIS methods, as well as the percent change. It shows that the location-dependent MIS method can reduce the absolute error by 60% compared to the method with constant IS values.

Table 4.6 Comparison between the constant and location-dependent MIS method

Overhang angle θ	Mean absolute error compared to measurement / µm		Percent Change $\frac{e_{var} - e_{const}}{\lvert e_{const} \rvert} \times 100\%$
	Constant MIS e_{const}	Location-dependent MIS e_{var}	
45°	124	50	-60%
50°	106	37	-65%
55°	93	30	-68%
60°	94	36	-62%
65°	68	21	-69%
70°	66	22	-67%

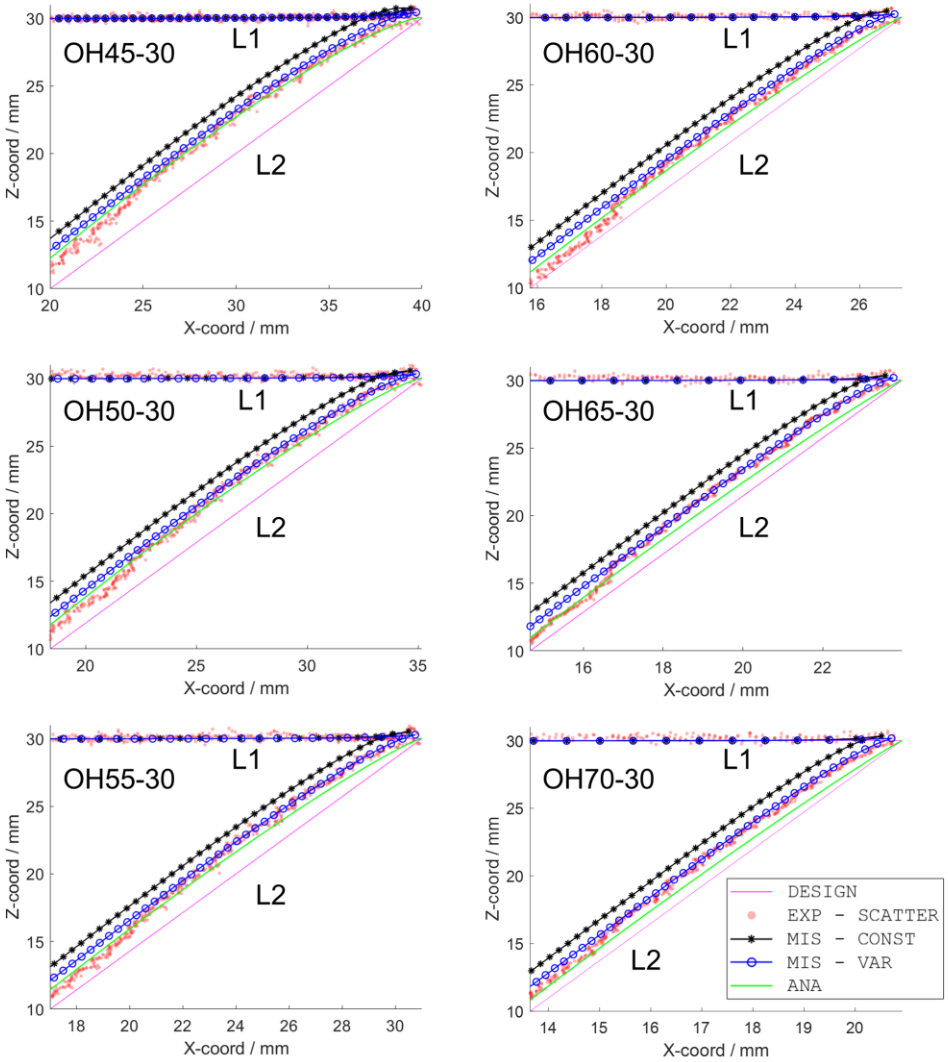

Figure 4.12 Comparison of the deformed shape of outlines L1 and L2. 'DESIGN' represents the design shape of the overhang, 'EXP-SCATTER' denotes the scanned point cloud data, 'MIS-CONST' is the result predicted by the MIS method with constant ISs, 'MIS-VAR' is the result predicted by the MIS method with location-dependent ISs, and 'ANA' represents the analytical solution by Ref. [147]. The deformation is upscaled by a factor of 10 for clarity.

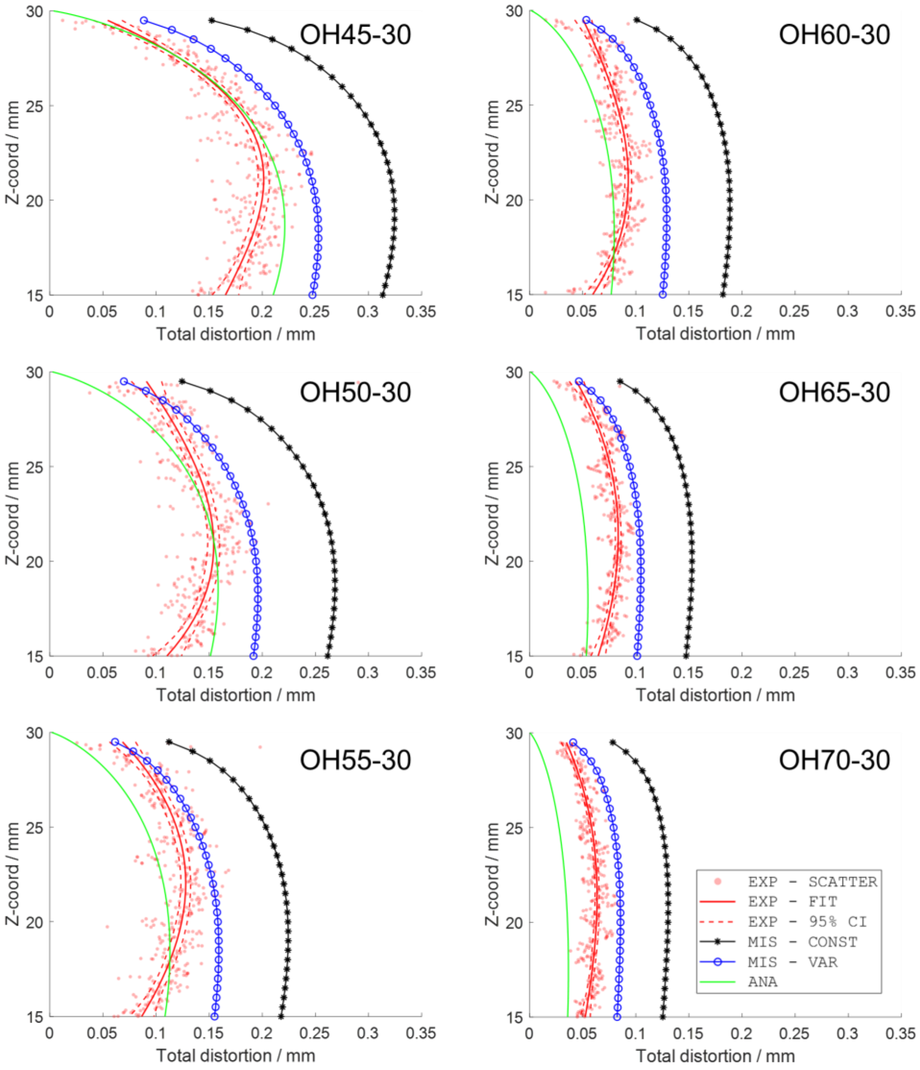

Figure 4.13 Comparison of the distortion on outline L2. 'EXP-SCATTER' denotes the scanned point cloud data, 'EXP - FIT' is the fitted curve based on the point cloud data, 'EXP - 95% CI' represents the 95% confidence interval of the fitted curve, 'MIS-CONST' is the result predicted by the MIS method with constant ISs, 'MIS-VAR' is the result predicted by the MIS method with location-dependent ISs, and 'ANA' represents the analytical solution by Ref. [147].

4.5.4 Prediction of Recoater Interference

Figure 4.14(a) shows the global thermal deformation U_z^{global} at the overhang tip, calculated by the location-dependent MIS method, for overhang wedges (OH), canonical parts, and tables. There is a rapid increase in U_z^{global} at the start of the deposition for overhang wedges with constant overhang angles. The smaller the overhang angle, the faster the increase is. After reaching a peak, the deformation gradually decreases. Conversely, a different deformation pattern is observed for canonical parts and tables: the U_z^{global} monotonically increases with increasing rate with build height, which is caused by varying overhang angles in these two geometries.

In Figure 4.14(a), the asterisk symbols (*) indicate the occurrence of recoater crashes. Multiple asterisks that appear on a single curve denote repeated experiments. For the failed overhang wedges (OH25, OH30, OH35, and OH40), it is observed that the smaller the overhang angle, the earlier the recoater crash occurs, and the greater the U_z^{global} at the time of the recoater crash. The specimens of canonical parts and tables fail at overhang angles between 26° and 31°, with the U_z^{global} at failure comparable to that of OH25 and OH30.

Figure 4.14(a) additionally displays the real powder layer thickness of 95 μm and its 95% CI calculated in Section 4.5.1. Two key observations emerge: (1) In each case where the recoater crash occurs, the U_z^{global} at the failure height remains smaller than the real powder layer thickness. (2) According to Section 4.5.2, the initial recoater interference on OH40 occurs at the height of 1.5 mm. But the corresponding U_z^{global} at this height is only 40 μm, significantly less than the real powder layer thickness. These observations confirm that it is not sufficient to consider global thermal deformation alone when predicting recoater interference; local edge thermal deformation must also be taken into account.

Note that the edge effect mainly affects the build-directional deformation at part edges on the top surface [124, 144]. The deformation on the side surface is predominantly controlled by the thermal gradients distributed in the entire part, that is, the global thermal deformation term. This is why, in Section 4.5.3, the location-dependent MIS method agrees well with the experimental measurement regarding the deformation on the down-facing surface of the overhang wedge.

Considering that the numerical modeling or analytical solution for calculating U_z^{local} is unavailable to date, we try to estimate U_z^{local} based on both experiments and simulations. According to MIS simulations, the global thermal deformation for OH40 at the height of 1.5 mm is 40 μm. Given that the powder layer thickness is 95 μm, the local edge deformation can be estimated by Eq. (4.2), U_z^{local} = 95 μm - 40 μm = 55 μm, which accounts for 58% of the powder layer thickness. Although it has been reported that the edge effect depends on the overhang angles [127], due to limited experimental resources to study this dependence, we assume the local edge deformation of 55 μm is applicable to any overhang angle here.

Figure 4.14(b) depicts the variation of the total deformation in the build direction U_z^{total}; that is, all deformation curves in Figure 4.14(a) are shifted upward by 55 μm. Several observations can be made from this figure:

(1) For samples that undergo recoater crash, including OH25, OH30, OH35, OH40, CA-100, TA-5, and TA-10, the crash always occurs at heights where U_z^{total} is greater than the powder layer thickness.

(2) While OH45 does not experience a recoater crash, portions of its deformation curve are above the line for powder layer thickness, indicating a high possibility of recoater interference. This is confirmed by the experiment where elevated areas are observed during the deposition (see Figure 4.7(c)).

(3) The U_z^{total} of OH30 surpasses the powder layer thickness between deposit heights of 1.0 mm and 1.5 mm, signaling the start of recoater interference. This is confirmed by the top surface topography of OH35-2.0, OH35-3.0, and OH35-4.0 shown in Figure 4.15(a) - (c). These samples, located on build plate OH-BP5, are 35° overhang wedges with respective heights of 2 mm, 3 mm, and 4 mm. At these heights, elevated edges on the right are noticeable. Furthermore, as the deposit height increases, the extent of edge deformation becomes more pronounced. The areas of negative deformation next to the elevated edges might be caused by recoater interference, wherein the recoater blade bends the overhang tip after running across it.

(4) The U_z^{total} of OH50 enters the CI of the powder layer thickness at around 4 mm in height, suggesting impending recoater interference. Figure 4.15(d) and (e) shows the U_z^{total} on the top surfaces of OH50-2.0 and OH50-4.0, with no signs of interference at the respective heights of 2 mm and 4 mm. On the other hand, the top surface topography of OH50-6.0 (6 mm high) shown in Figure 4.15(f) reveals noticeably elevated edges on the right.

(5) The U_z^{total} of the canonical part exceeds the powder layer thickness at a height of approximately 30 mm. However, there are no signs of recoater interference for CA-60 (29.03 mm in height) and CA-72 (34.84 mm in height), as shown in Figure 4.16(a) and (b). Significantly raised edges emerge at 36.78 mm for CA-76, as shown in Figure 4.16(c). This suggests that the actual occurrence of recoater interference is between 34.84 mm and 36.78 mm, not at the predicted 30 mm. This discrepancy may be attributed to the assumption that local thermal deformation remains constant across all overhang angles. The variability of the overhang angle with height in the canonical part

makes predicting recoater interference more challenging. Although there is some error in the prediction, the conservative estimate of 30 mm provides a safety margin in part design.

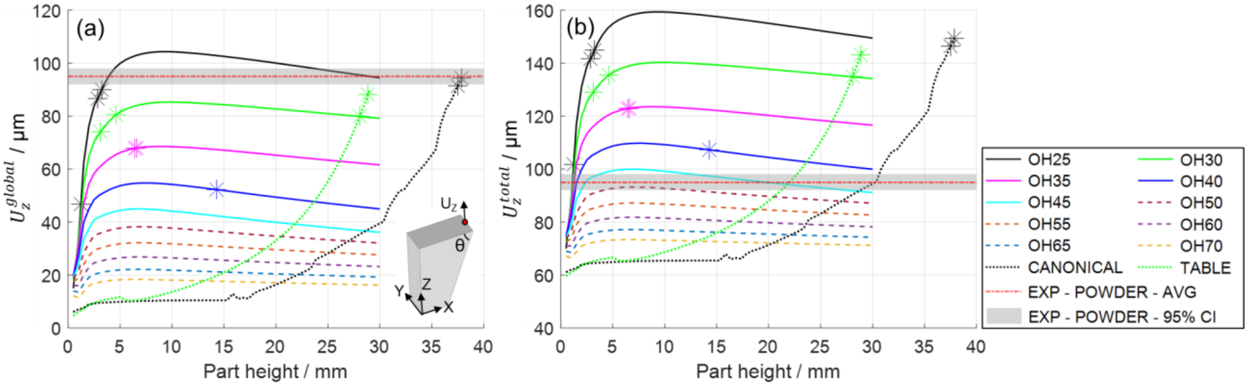

Figure 4.14 (a) Build-directional global thermal deformation U_z^{global} versus part height, and (b) build-directional total deformation U_z^{total} versus part height. The asterisk symbols (*) mark the part heights at which recoater crashes occur. Multiple asterisks on a curve represent duplicate experiments. No asterisk symbol on a curve means the corresponding structure was printed without a recoater crash. 'EXP - AVG - POWDER' is the average powder thickness, and 'EXP - 95% CI - POWDER' denotes the 95% confidence interval of the powder thickness.

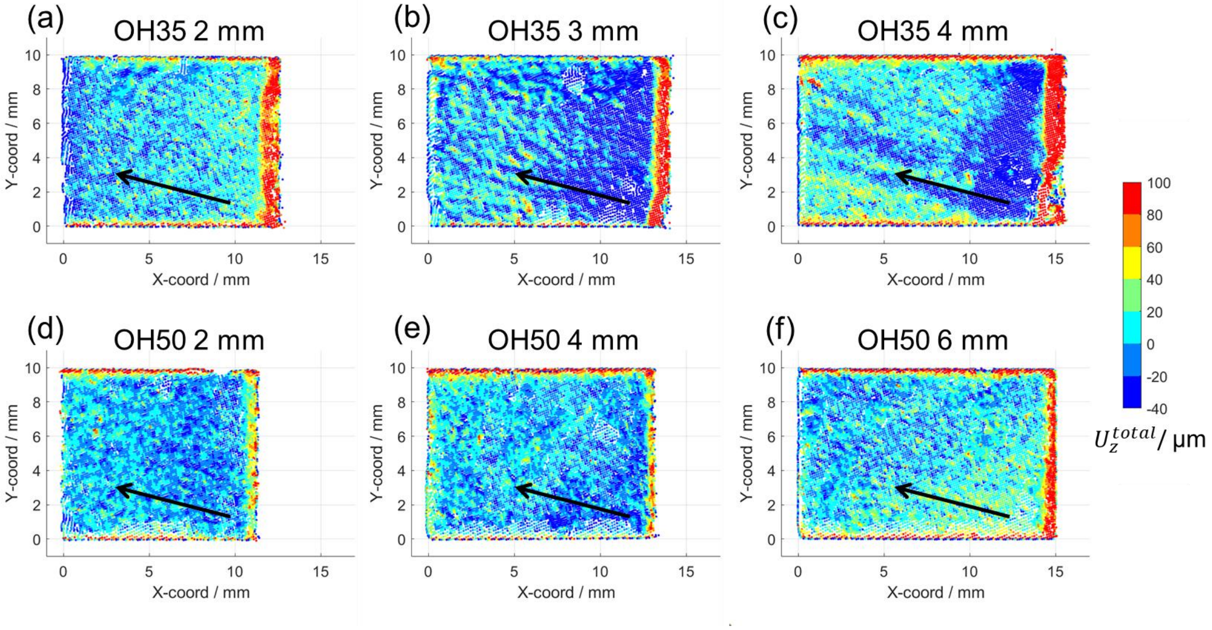

Figure 4.15 Top surface topography of the overhangs on build plate OH-BP5: (a) OH35-2.0; (b) OH35-3.0; (c) OH35-4.0; (d) OH50-2.0; (e) OH50-4.0; (f) OH50-6.0. The black arrows show the direction of the recoater blade.

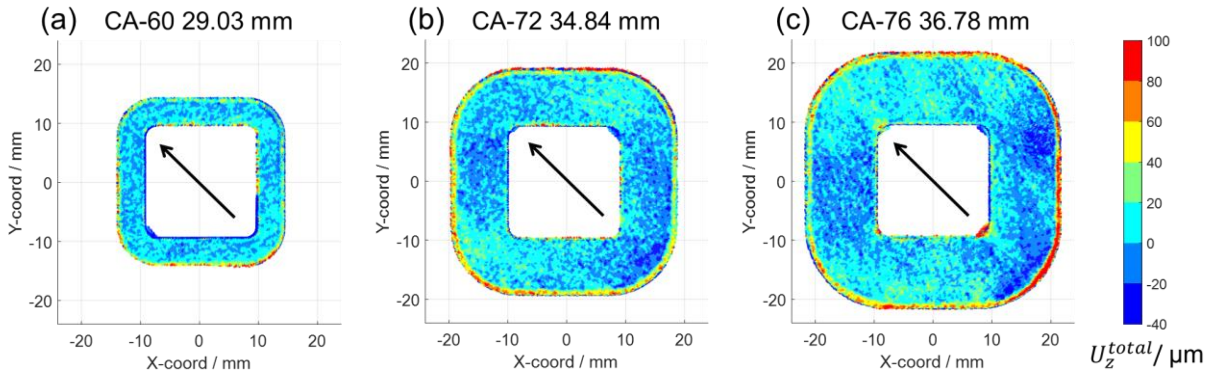

Figure 4.16 Top surface topography of the canonical parts on build plate CT-BP1: (a) CA-60; (b) CA-72; (c) CA-76. The black arrows show the direction of the recoater blade.

4.6 Conclusions

In this work, we propose and validate a framework that combines simulation and experimental approaches for predicting recoater interference and investigating recoater crashes in the L-PBF process. We use numerical simulations with the MIS method, incorporating location-dependent ISs, to predict global thermal deformation in parts with overhangs. The local edge deformation is determined by reconciling the simulated global deformation with the measured deformation in the printed overhang wedges. In addition, calibration/validation experiments are conducted using geometries of staircases, canonical parts, and tables. Both in-situ video monitoring and ex-situ deformation measurements are employed in this study. The key findings from the study are summarized as follows:

(1) The staircase experiment indicates a powder layer thickness of 95 μm, approximately 3.2 times the nominal solid layer thickness.

(2) Experiments on overhang wedges reveal that (i) initial recoater interference may occur at the early stage of deposition, around 50 layers, (ii) parts that are successfully printed can still encounter recoater interference during deposition, and (iii) smaller overhang angles lead to earlier crashes and greater deformation of the overhang edge in the build direction upon recoater crash.

(3) An overhang angle θ of approximately 45° is commonly recognized as the limit for printing overhangs without support structures [156, 157]. When θ is less than this angle, achieving satisfactory surface quality in overhang regions is challenging. Our numerical simulations and experimental measurements reveal that even at an angle of 45°, recoater interference cannot be entirely ruled out. In fact, we observe recoater interference in overhangs with θ up to 50°.

(4) The MIS method with location-dependent ISs can effectively capture IS variations in the overhang region. The new method reduces the absolute error in deformation prediction by approximately 60% compared to the MIS method with constant ISs.

(5) The total build-direction deformation at the edges of an overhang structure comprises a global thermal component from laser-induced thermal gradients distributed throughout the part and a local edge component due to melt pool dynamics near the edges. The global thermal deformation is calculated by the MIS method, and the local edge deformation is estimated at 55 μm. The threshold for potential interference is set when the deformation in the build direction surpasses the powder layer thickness.

5.0 Data-driven Distortion Compensation for L-PBF Using the Gaussian Process Regression and Inherent Strain (IS) Method

5.1 Current Progress of Distortion Compensation in L-PBF

The thermal-gradient-induced distortion in L-PBF processes adversely affect the dimensional quality of manufactured components [158]. One way to address this issue is through the distortion compensation technique. The fundamental idea of this technique is to pre-distort the design geometry of a part prior to manufacturing, resulting in an as-built part that closely matches the intended design geometry. Within the framework of distortion compensation, two crucial tasks emerge: determining the deformation and calculating the pre-deformation.

Experimental measurement is a practical approach to obtaining part deformations. Afazov et al. [159, 160], Xu et al. [161], and Wang et al. [162] introduced distortion compensation approaches using 3D optically scanned data. Due to the mismatch between the mesh of the design part and the mesh of the corresponding as-built part which is converted from the scanned point cloud data, various point registration techniques were developed to determine the deformation of the part accurately. Afazov et al. [159, 160] employed a search algorithm to locate the projection point of the deformed node on the reference plane. Xie et al. [163, 164] proposed a generalized Bayesian regularization network approach to map the distorted structure back to its original designed configuration. The pre-deformation of a surface point is derived by simply inverting its deformation.

However, considering that experimental measurement is time-consuming and costly, especially when determining the deformation of internal features inside a part, some researchers leverage physics-based numerical simulations, such as FE analysis (FEA), to predict the part deformation. Afazov et al. [165], Yaghi et al. [166], Stiuso [167] and Biegler et al. [168] developed similar FE-based compensation methods for L-PBF and DED processes. These methods involve numerical determination of deformations, thereby eliminating the need for scanning and point registration. The compensated geometry is created by superimposing the inverted deformation onto the original design.

The studies above set the pre-deformation as a linear inversion of the part deformation. However, Biegler et al. [168] reported that in the case of complex geometries, the deformations are non-linear and dependent on the geometry itself. Therefore, using linearly inverted deformation to pre-distort the design geometry may lead to inaccuracies.

One way to deal with non-linear deformation is to use iterative methods [168]. In this method, each iteration involves setting the pre-deformation to be a portion of the linearly inverted deformation (typically using a scaling factor of 75% [169]) computed from the previous iteration. The compensation process continues until the deviation between the as-built part and the intended design geometry is below a specified tolerance. Due to its ease of implementation, the iterative method has gained widespread adoption in commercial software, such as ANSYS Additive Print [169] and Autodesk Fusion 360 Netfabb [170]. However, it should be noted that the iterative method can be computationally expensive if an inappropriate scaling factor or tolerance is chosen.

Besides the iterative method, several studies have focused on utilizing machine learning (ML) approaches to calculate the pre-deformation due to their ability to address non-linear problems in AM processes [171]. Chowdhury and Anand [172] proposed a compensation approach based on artificial neural networks (ANN). This method first performs thermomechanical FEA to determine the deformed shape of a given design. Then, the design and deformed shape, represented in terms of nodal coordinates, are utilized to train an ANN model by mapping the deformed shape (input) to the design shape (output). After training, the design shape is used as the model input, and the model output becomes the compensated shape. In a subsequent study, McConaha and Anand [18] extended this method from two perspectives. First, the deformed shape is acquired experimentally using an optical scanning device instead of numerical simulations. Second, they use the deformation relative to the design shape, rather than the nodal coordinates, to train the ANN model, with the aim of improving its performance. Hong et al. [173] implemented both linear inversion and ANN approaches to compensate for submillimeter overhang trusses fabricated using L-PBF. Experimental results demonstrate that the ANN approach achieves higher geometrical accuracy.

In this work, we propose a distortion compensation framework, adapted from [174], for L-PBF that includes an IS model for determining part deformation and a Gaussian process (GP) model for calculating pre-deformation. Additionally, we examine the effects of (1) lumped layer thickness and surface curviness, (2) the number of trial geometries, and (3) the number of transient deformation states on the accuracy of the compensation method.

5.2 Framework for Distortion Compensation

Given a geometry, the distortion compensation framework consists of four steps: (1) generating a training dataset containing deformation data using the IS method combined with the experimental measurement; (2) employing principal component analysis (PCA) to reduce the dimensionality of the data; (3) training the Gaussian process regression (GPR) model and computing the pre-deformation; (4) generating the compensated shape and exporting it as a printable CAD file. Figure 5.1 shows the flowchart of the proposed distortion compensation framework. These steps will be described in detail in this section.

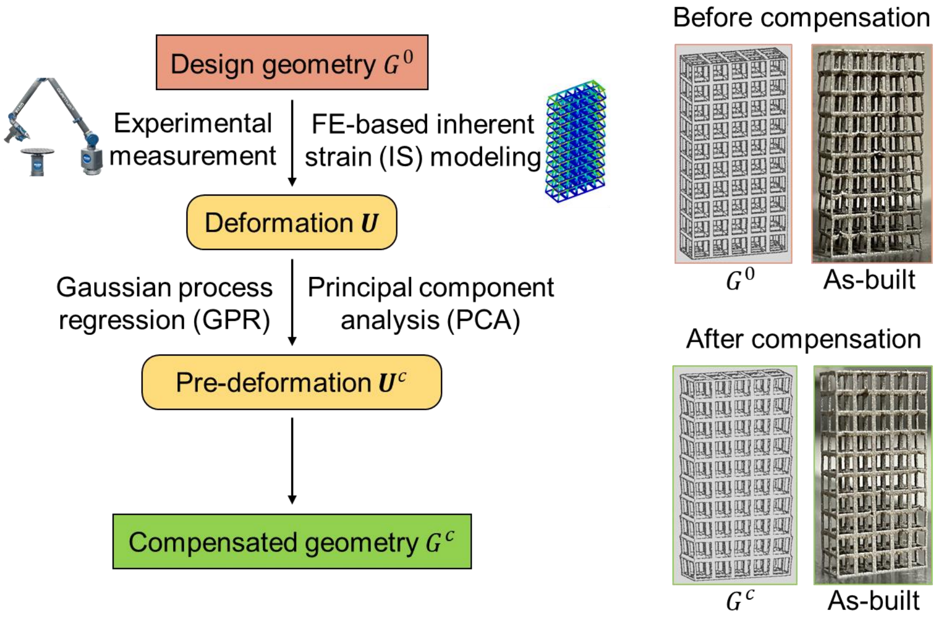

Figure 5.1 Flowchart of the distortion compensation framework.

5.2.1 Optimization of Inherent Strains

Considering that accurate predictions of the distortion are critical to the subsequent compensation process and the influence of deposition process parameters on ISs is beyond the scope of this research, we employ the empirical method to find the ISs in this chapter. The IS values are optimized in ANSYS optiSLang 2021R1 [175] as a single-objective optimization task. The design variables are the directional components of the ISs, and the objective function g is the error between the experimental measurements and the simulation results in terms of part distortion. The mathematic expression of the task is:

$$g(\varepsilon_x, \varepsilon_y, \varepsilon_z) \rightarrow \min \tag{5.1}$$

where ε_x, ε_y, and ε_z are the ISs in three orthogonal directions. In this work, ε_x, ε_y are defined in the printing plane and ε_z is along the build direction. Furthermore, constraints on design variables such as lower and upper bounds can be generalized by the following expressions:

$$\begin{aligned} &h_i\left(\varepsilon_x, \varepsilon_y, \varepsilon_z\right) = 0, \quad i = 1,2,\dots,m_e \\ &l_j\left(\varepsilon_x, \varepsilon_y, \varepsilon_z\right) \geq 0, \quad j = 1,2,\dots,m_u \end{aligned} \tag{5.2}$$

where h_i and l_j are equality and inequality constraints that are required to be satisfied, respectively; m_e and m_u are the number of equalities and inequalities, respectively.

In this study, we use the gradient-based non-linear programming by quadratic Lagrangian (NLPQL) approach to search the local optimum as it is recommended by ANSYS optiSLang for low-dimensional tasks with fewer than 20 design variables. The objective function is the mean squared error between the measured and simulated deformations. The IS method is implemented using ANSYS Mechanical 2021R1 in this chapter.

5.2.2 Gaussian Process

The Gaussian process is a popular framework for supervised ML, which is utilized extensively in regression and classification tasks. A GPR model allows for the prediction of continuous quantities that integrate prior knowledge, such as kernels, and also provides measures of uncertainty for those predictions [176, 177].

In general, for a regression problem, we have a training set $\mathcal{D}$ of n observations, $\mathcal{D} = \{(\mathbf{x}_i, y_i) | i = 1, \dots, n\}$, where $\mathbf{x}_i$ denotes a d-by-1 input vector (d is the number of predictors or features) and y_i denotes a scalar response [176]. The regression is to estimate a function f that most closely fits the data:

$$y_i = f(\mathbf{x}_i) + \varepsilon_i, \quad i = 1, \ldots, n \tag{5.3}$$

where ε is a noise.

A GPR model, denoted as $\mathcal{GP}$, uses a mean function $m(\mathbf{x})$ and a covariance (kernel) function $k(\mathbf{x}_i, \mathbf{x}_j)$ to achieve the estimation [176]:

$$f(\mathbf{x}) \sim \mathcal{GP}\left(m(\mathbf{x}), k(\mathbf{x}_i, \mathbf{x}_j)\right) \tag{5.4}$$

$$m(\mathbf{x}) = \mathbb{E}[f(\mathbf{x})] \tag{5.5}$$

$$k(\mathbf{x}_i, \mathbf{x}_j) = \mathbb{E}\left[\left(f(\mathbf{x}_i) - m(\mathbf{x}_i)\right)\left(f(\mathbf{x}_j) - m(\mathbf{x}_j)\right)\right] \tag{5.6}$$

In the present work, the GPR analysis is implemented in MATLAB. An ARD squared exponential kernel function is employed, where ARD denotes automatic relevance determination [178]:

$$k(\mathbf{x}_i, \mathbf{x}_j) = \sigma_f^2 \exp\left[-\frac{1}{2}\sum_{m=1}^{d}\frac{\left(x_{im} - x_{jm}\right)^2}{\sigma_m^2}\right] \tag{5.7}$$

where σ_m represents the length scale for predictor *m*, *m* = 1, 2, ..., *d* and σ_f is the signal standard deviation. Both σ_m and σ_f are hyper-parameters in the kernel function. x_{im} is the value of predictor *m* in the input vector $\mathbf{x}_i$.

5.2.3 Generation of the Deformation Dataset

The IS method is first implemented on the design geometry G^0 to obtain the deformation $\boldsymbol{U}^0$, which can be written as a matrix:

$$\boldsymbol{U}^0 = \begin{bmatrix} \boldsymbol{u}^{0-0} & \cdots & \boldsymbol{u}^{0-k} & \cdots & \boldsymbol{u}^{0-N_L} \end{bmatrix}^T \tag{5.8}$$

$$\boldsymbol{u}^{0-k} = \begin{bmatrix} u_{1x}^{0-k} & u_{1y}^{0-k} & u_{1z}^{0-k} & \cdots & u_{ij}^{0-k} & \cdots & u_{Nz}^{0-k} \end{bmatrix} \tag{5.9}$$

where the superscript 0 in $\boldsymbol{U}^0$ and $\boldsymbol{u}^{0-k}$ denotes that the deformation belongs to geometry G^0. $\boldsymbol{u}^{0-k}$ is the *k*th deformation state and its component u_{ij}^{0-k} represents the deformation value of node *i* ($i = 1, \ldots, N$) in the *j*-direction ($j = x, y, z$) when the *k*th layer ($0 \leq k \leq N_L$) has been deposited. *N* is the total number of nodes in the FE model (total degrees of freedom are 3*N*). N_L is the number of lumped layers in the FE model. Vector $\boldsymbol{u}$ has a constant length 3*N*, which means it always contains deformation of all the nodes in the FE model, regardless of their activation status.

The deformation matrix $\boldsymbol{U}^0$ does not necessarily need to include the deformation state for every layer in the IS model but should at least contain the initial deformation state $\boldsymbol{u}^{0-0}$ and the final deformation state $\boldsymbol{u}^{0-N_L}$. It is worth noting that in the current study, the deformation of a geometry is always calculated with respect to the design shape G^0 (reference configuration). Therefore, we have $\boldsymbol{u}^{0-0} = \boldsymbol{0}$ in $\boldsymbol{U}^0$. Later, we will introduce the concept of trial geometry, for which the initial state does not always equal to zero.

In addition to the initial and final states, we have the option to store several intermediate states (usually evenly distributed) in $\boldsymbol{U}^0$. The total number of deformation states is denoted as N_k. For example, for a model with $N_L = 40$ layers, $\boldsymbol{U}^0$ can be assembled with different N_k:

$$\begin{gathered}
\boldsymbol{U}^0 = \begin{bmatrix} \boldsymbol{u}^{0-0} & \boldsymbol{u}^{0-40} \end{bmatrix}^{\mathrm{T}} \quad (N_k = 2) \\
\boldsymbol{U}^0 = \begin{bmatrix} \boldsymbol{u}^{0-0} & \boldsymbol{u}^{0-20} & \boldsymbol{u}^{0-40} \end{bmatrix}^{\mathrm{T}} \quad (N_k = 3) \\
\boldsymbol{U}^0 = \begin{bmatrix} \boldsymbol{u}^{0-0} & \boldsymbol{u}^{0-10} & \boldsymbol{u}^{0-20} & \boldsymbol{u}^{0-30} & \boldsymbol{u}^{0-40} \end{bmatrix}^{\mathrm{T}} \quad (N_k = 5)
\end{gathered} \tag{5.10}$$

It will be pointed out in Section 5.4.3 that using the design geometry alone in the compensation is not sufficient. Several trial geometries are created based on the design geometry and its distortion [174]. The shape of a trial geometry G^t is determined by multiplying the final deformation of the design geometry $\boldsymbol{U}^0$ by a scaling factor r_t, which is typically selected within the range [-1.5, -0.5], and adding it to the design shape G^0:

$$G^t = G^0 + r_t \boldsymbol{u}^{0-N_L} \tag{5.11}$$

As mentioned previously, since the design geometry G^0 is the reference configuration for calculating the deformation, the initial state of a trial geometry G^t is not zero and can be expressed as:

$$\boldsymbol{u}^{t-0} = r_t \boldsymbol{u}^{0-N_L} \tag{5.12}$$

Similar to the design geometry, the IS method is applied to simulate the deformation of the trial geometries. The total deformation matrix consisting of deformation states of both design and trial geometries can be expressed as:

$$\boldsymbol{U} \quad = [\boldsymbol{U}^0 \quad \boldsymbol{U}^1 \quad \cdots \quad \boldsymbol{U}^t \quad \cdots \quad \boldsymbol{U}^{N_t}]^T \tag{5.13}$$

where $\boldsymbol{U}^t$ is the deformation matrix of geometry G^t $(t = 0, \dots, N_t)$. N_t is the number of trial geometries.

The use of trial geometries aims to collect more deformation data and expand the training dataset to make the ML model more accurate. The influence of N_t on compensation accuracy will be discussed in Section 5.4.3. The total deformation dataset $\boldsymbol{U}$ is a $(N_t + 1)N_k$-by-$3N$ matrix where each row represents a particular deformation state for a geometry, and each column represents a degree of freedom.

5.2.4 Principal Component Analysis

For a large FE model with tens or even hundreds of thousands of nodes, the deformations of these nodes are not independent because they are connected by elements that follow specific material constitutive behavior. When we use the GPR model to learn the deformation pattern and predict the pre-deformation, it is a good practice to use a reduced order model (ROM) for efficiency [174]. We perform PCA to the deformation dataset $\boldsymbol{U}$ before training the GPR model, aiming to reduce the dimensionality of the dataset while minimizing the loss of information. The dimensional reduction is achieved by finding new linear combinations of variables known as principal components to characterize the dataset [179, 180]. The PCA of the deformation dataset $\boldsymbol{U}$ can be expressed as [181]:

$$\boldsymbol{S} = \boldsymbol{U}\boldsymbol{W} \tag{5.14}$$

where $\boldsymbol{W}$ is a $3N$-by-N_p matrix whose columns are eigenvectors of $\boldsymbol{U}^{\mathrm{T}}\boldsymbol{U}$. $\boldsymbol{S}$ is a $(N_t + 1)N_k$-by-N_p matrix of principal component scores. Each row of $\boldsymbol{S}$ corresponds to scores characterizing one deformation state of the FE model. N_p is the number of principal components retained from dataset $\boldsymbol{U}$ such that $0 < N_p \leq N_{pt}$. $N_{pt} = \min\big((N_t + 1)N_k, 3N\big)$ is the maximum number of principal components that can be obtained through PCA. In this study, N_p is determined such that the retained principal components (in descending order according to their eigenvalues) can explain 99% of the variation in the data:

$$e = \sum\nolimits_{i=1}^{N_p} \sigma_i \Big/ \sum\nolimits_{i=1}^{N_{pt}} \sigma_i \geq 99\% \tag{5.15}$$

where σ_i represents the eigenvalue of the *i*th principal component.

After performing PCA, the goal of the GPR is to learn and predict the scores corresponding to each principal component. Therefore, the number of GPR models is N_p.

5.2.5 Gaussian Process Regression

In the GPR model, the score matrix $\boldsymbol{S}$ is defined as:

$$\boldsymbol{S} = \begin{bmatrix} \boldsymbol{S_1} & \cdots & \boldsymbol{S_p} & \cdots & \boldsymbol{S_{N_p}} \end{bmatrix} \tag{5.16}$$

$$\boldsymbol{S_p} = \Big[\underbrace{s_p^{0-0} \quad \cdots \quad s_p^{0-N_L}}_{For\ design\ geometry\ G^0} \quad \underbrace{s_p^{1-0} \quad \cdots \quad s_p^{1-N_L}}_{For\ trial\ geometry\ G^1} \quad \cdots \quad \underbrace{s_p^{N_t-0} \quad \cdots \quad s_p^{N_t-N_L}}_{For\ trial\ geometry\ G^{N_t}}\Big]^T \tag{5.17}$$

The input feature of the GPR model for each principal component for a given geometry is a two-dimensional vector. The first entry is the kth deposited layer of the output geometry, and the second entry is the principal component score when the entire part is done printing (i.e., after the last layer is deposited); whereas the output is the principal component score after the kth layer is deposited, see Figure 5.2 (left). To predict the compensated geometry using the trained model, we set the input feature to be $(0 \quad s_p^{0-0})$, and the corresponding output s_p^c is then the component score for the pre-deformation of the geometry, as shown in Figure 5.2 (right). Suppose a geometry has a pre-deformation s_p^c, its final deformation should be s_p^{0-0}, which corresponds to the deformation of the design geometry at the initial state and equals zero ($\boldsymbol{u}^{0-0} = \boldsymbol{0}$).

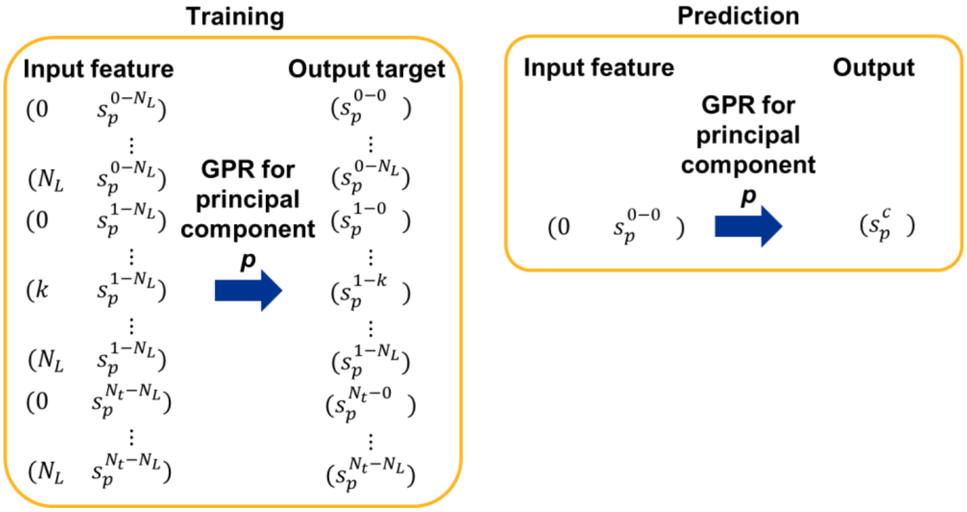

Figure 5.2 Structure of the GPR model for *p*th principal component $(0 < p \leq N_p)$.

5.2.6 Generation of the Compensated Geometry

After GPR, the principal component scores corresponding to the compensated shape $\boldsymbol{S^c}$ are determined (Equation (5.18)). Then, the pre-deformation $\boldsymbol{U^c}$ is calculated by multiplying $\boldsymbol{S^c}$ by the transpose of $\boldsymbol{W}$ (Equation (5.19)). Finally, the compensated shape G^c is obtained via Equation (5.20). The compensated shape is created based on the FE model. It is stored as a text file containing the nodal coordinates and element connectivity. This file can be easily converted to STP format for subsequent manufacturing. In this study, the conversion process is performed using ANSYS Workbench 2021R1.

$$\boldsymbol{S^c} = \begin{bmatrix} \boldsymbol{s_1^c} & \boldsymbol{s_2^c} & \cdots & \boldsymbol{s_{N_p}^c} \end{bmatrix} \tag{5.18}$$

$$\boldsymbol{u^c} = \boldsymbol{S^c}(\boldsymbol{W})^{\boldsymbol{T}} \tag{5.19}$$

$$\boldsymbol{G^c} = \boldsymbol{G^0} + \boldsymbol{u^c} \tag{5.20}$$

5.3 Experimental Validation

Two geometries were utilized for validating the proposed data-driven compensation approach. One is a lattice structure and the other is a canonical part, as shown in Figure 5.3. The objective of the compensation was to minimize the geometric disparity between the original design and the as-built part. The validation process includes the following procedures: (1) printing the part using the design CAD file; (2) measuring the part distortion; (3) using the measurement to optimize the ISs; (4) implementing the distortion compensation; (5) printing the part again using the compensated shape.

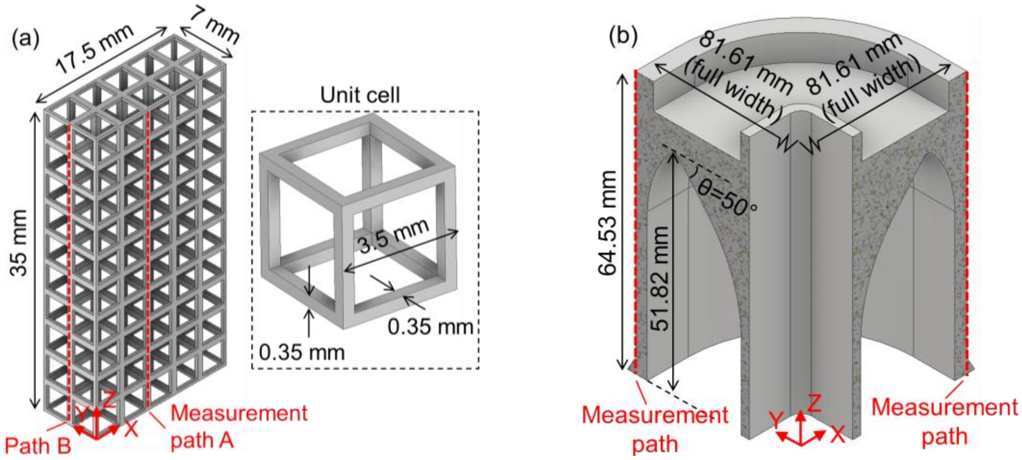

Figure 5.3 Geometries for validation: (a) lattice and (b) canonical (quarter view).

All the parts were printed on an EOS M290 DMLS system using AISI stainless steel 316L powder. The default process parameters for 316L were employed, including a layer thickness of 40 µm. The chamber was filled with argon to create an inert environment, and a brush powder recoater was used. The 316L powder was manufactured by Praxair Surface Technologies, Inc., having a packing density of 4 g/cm^3. The particle size distribution was reported as, according to ASTM B822, d_{10} = 18 µm, d_{50} = 31 µm, and d_{90} = 49.3 µm. The part distortion was measured by an 8-axis Quantum Max (S Model) FaroArm laser scanning system [150]. In the current validation, three trial geometries ($N_t = 3$) were generated with scaling factors of $r_1 = -1.5$, $r_2 = -1.0$, and $r_3 = -0.5$. The number of principal components to be extracted for the regression process is determined by Equation (5.15).

5.3.1 Distortion Compensation on Lattice Structure

The as-built lattice structure printed using the design shape is shown in Figure 5.4(a). The part distortion is evident, particularly around the corners where the horizontal (in X- and Y-direction) and vertical (in Z-direction) bars intersect. During the printing, when it comes to depositing layers that solely consist of vertical bars, as shown in Figure 5.5(a), the shrinkage effect in the XY-plane is relatively subtle because the deposited area for each bar is small, approximately 0.7 × 0.7 mm², and they are not connected. However, in deposit layers containing both horizontal and vertical bars shown in Figure 5.5(b), the deposited area is connected and expands to 0.7 × 17.5 mm² for bars along the X-direction and 0.7 × 7 mm² for bars along the Y-direction. Consequently, the shrinkage in the XY-plane becomes much more pronounced, resulting in noticeable distortion in the corners.

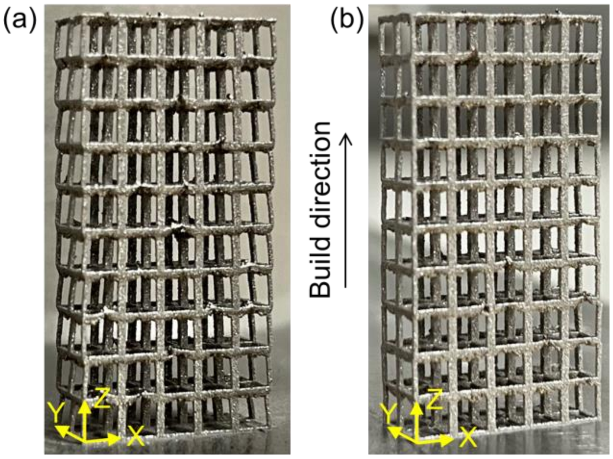

Figure 5.4 As-built lattice structure printed with: (a) design shape; (b) compensated shape.

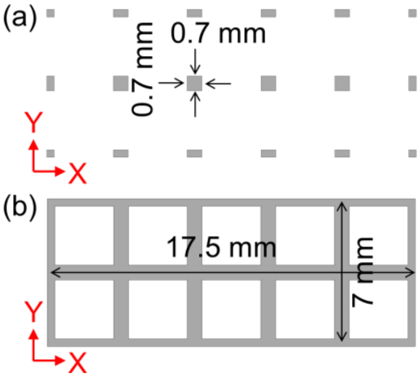

Figure 5.5 Cross-section of the lattice structure in the build direction that contains: (a) only vertical bars; (b) both vertical and horizontal bars.

The distortion of the design shape along two measurement paths A and B (see Figure 5.3(a)) were extracted to calibrate the IS values. In the FE model, the lumped layer thickness (LLT) is set to 0.175 mm so that, within a unit cell, each bar consists of at least two lumped layers in the build direction. Since the layer thickness set on the EOS system is 40 µm, each layer of element corresponds to approximately 4.4 real layers. Figure 5.6 presents the distortion in Path A and B obtained from the measurement (EXP - DSGN) and calibrated IS simulation (SIM - DSGN). The distortion variation patterns in the two paths are similar but have different amplitudes. This is because the horizontal bars in the X- and Y-directions have different lengths and thus different shrinkages. A quantitative comparison regarding the maximum and average absolute distortion along Path A and B is listed in Table 5.1, where the error varies between 2.5% and 9.6%. The results demonstrate a good agreement between the simulation and measurement. The calibrated IS values are listed in Table 5.2.

After calibrating the IS values, we followed the procedures presented in Section 5.2 to compensate for the lattice structure: creating three trial geometries, generating the deformation dataset, performing PCA and GPR, and finally obtaining the compensated shape. The as-built compensated part is shown in Figure 5.4(b). The distortions along Path A and B extracted from measurement (EXP - COMP) and simulation (SIM - COMP) are shown in Figure 5.6. Compared with the design shape, the distortion of the compensated shape is significantly decreased. The maximum and average absolute distortions along these two paths are listed in Table 5.3 and visualized in Figure 5.7. Overall, the reduction in distortion in the experiment (EXP - COMP) is less pronounced than in the simulation (SIM - COMP). For instance, the simulation data indicate that the proposed compensation approach can reduce the maximum distortion in Path A by 92.7%, whereas the experiment shows only a 53.7% reduction. The reasons for this discrepancy will be discussed in Section 5.4.

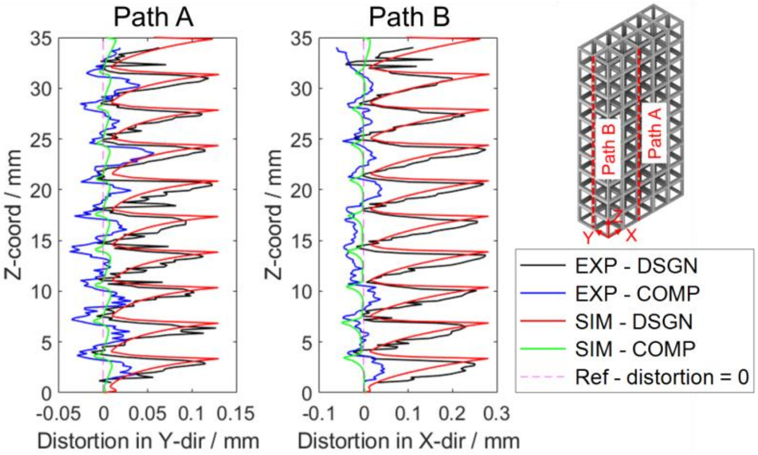

Figure 5.6 Distortion results for the lattice structure. EXP represents measurement and SIM represents simulation. DSGN denotes the original design shape and COMP denotes the compensated shape.

Table 5.1 Distortion (absolute value) of the lattice structure printed with the design shape

	Maximum (mm)		Error in max. (%)		Average (mm)		Error in avg. (%)	
	Path A	Path B	Path A	Path B	Path A	Path B	Path A	Path B
EXP - DSGN	0.123	0.275	N/A	N/A	0.052	0.118	N/A	N/A
SIM - DSGN	0.130	0.282	5.7	2.5	0.047	0.110	9.6	6.8

Table 5.2 Calibrated IS values for the lattice structure

LLT (mm)	X-dir.	Y-dir.	Z-dir.
0.175	-0.023	-0.023	0.019

Table 5.3 Distortion (absolute value) of the lattice structure printed with the compensated shape

	Maximum (mm)		Reduction in max. (%)		Average (mm)		Reduction in avg. (%)	
	Path A	Path B	Path A	Path B	Path A	Path B	Path A	Path B
EXP - COMP	0.057	0.048	53.7	82.5	0.015	0.023	71.2	80.5
SIM - COMP	0.009	0.040	92.7	85.5	0.004	0.008	92.3	93.2

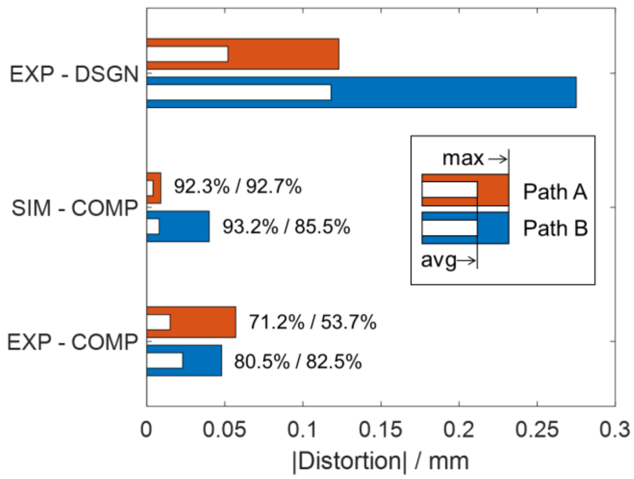

Figure 5.7 Maximum and average distortion (absolute value) of the lattice structure. The percentages next to the bars represent the reduction in avg. (left) and max. (right) distortion with respect to EXP - DSGN.

5.3.2 Distortion Compensation on Canonical Part

Figure 5.8(a) illustrates the as-built canonical part printed using the design shape. To calibrate the ISs, the distortion along four measurement paths on the outer surface in the build direction (as depicted in Figure 5.3(b)) was extracted. Note that Figure 5.3(b) only displays two marked paths because it provides a quarter view and does not show the remaining two paths on the hidden sides. We noted that the IS values depend on the LLT in the FE model during the calibration process. Therefore, three FE models with LLT of 0.5 mm (LL05), 1.0 mm (LL10), and 1.5 mm (LL15) were created and calibrated individually.

The calibration results are shown in Figure 5.9(a). The negative distortion indicates that points on the measurement path deform towards the center of the canonical part. The curve representing the experiment is obtained by averaging the distortion data over all the paths. The distortion curve exhibits two peaks along the build direction, around Z = 52 mm and 14 mm. Both of these peaks are attributed to the joining of the inner and outer structures approximately at the height of Z= 52 mm. After joining together, the inner overhang structure exerts a strong constraint on the outer wall, resulting in a large deformation there. The quantitative comparison between the experimental and simulated distortion is presented in Table 5.4. Overall, all the numerical models can follow the distortion pattern with errors ranging from 2.0% to 13.7%, demonstrating their effectiveness in predicting the distortion of the canonical part.

Table 5.5 lists the calibrated IS values for the canonical part. Two points are worth noting: (1) the ISs listed in Table 5.5 differ from those in Table 5.2 for lattice structures, indicating that the IS values are geometry-dependent. Reference [52] further states that the ISs for a lattice structure depend on its relative density. (2) FE models with different LLTs yield different accuracies in distortion predictions and varying IS values, even after undergoing the same optimization process. These discrepancies will be further discussed in Section 5.4.

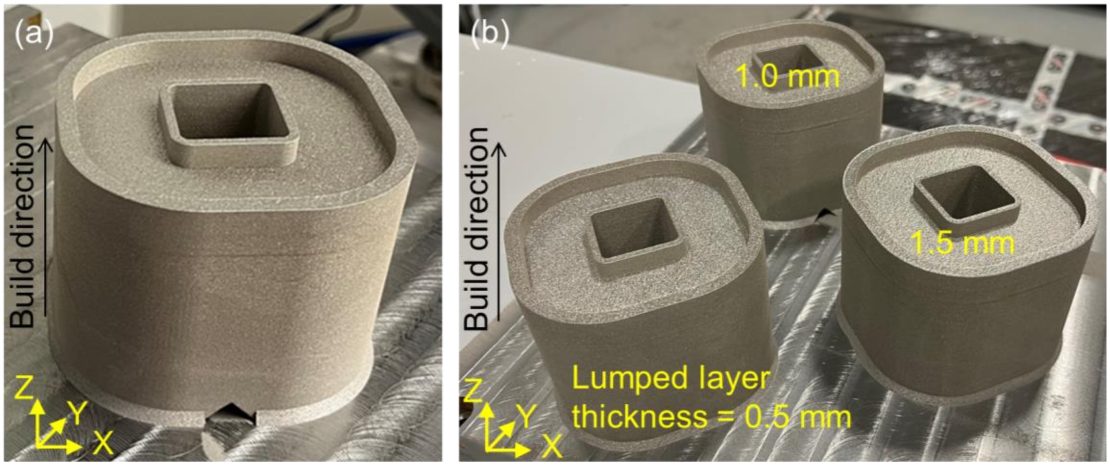

Figure 5.8 As-built canonical part printed with (a) design shape; (b) compensated shape.

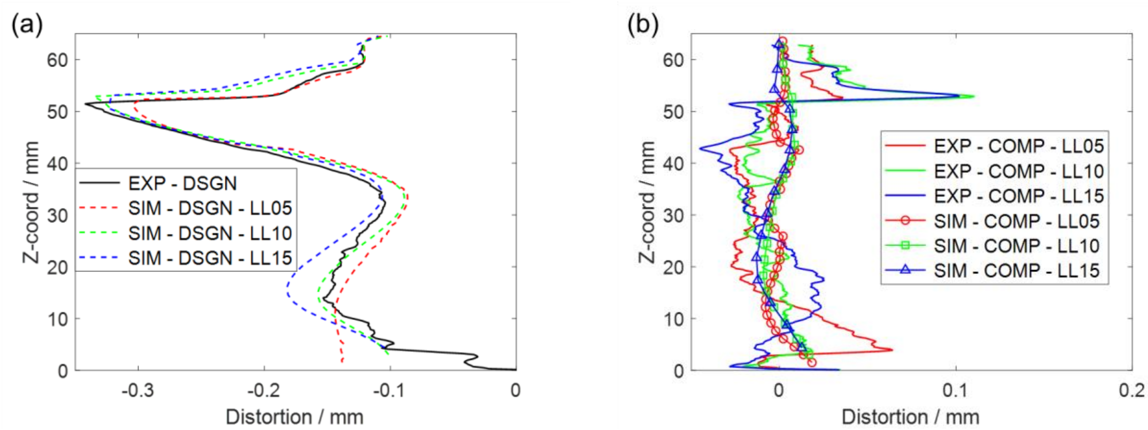

Figure 5.9 Distortion results for the canonical part: (a) design shape; (b) compensated shape. LL05, LL10, and LL15 represent LLT of 0.5 mm, 1.0 mm, 1.5 mm.

Table 5.4 Distortion (absolute value) of the canonical part printed with the design shape

	Maximum (mm)	Error in max. (%)	Average (mm)	Error in avg. (%)
EXP - DSGN	0.347	N/A	0.153	N/A
SIM - DSGN:				
LL05	0.305	12.1	0.150	2.0
LL10	0.336	3.2	0.158	3.3
LL15	0.323	6.9	0.174	13.7

Table 5.5 Calibrated IS values for the canonical part

LLT (mm)	X-dir.	Y-dir.	Z-dir.
0.5	-0.050	-0.050	0.020
1.0	-0.018	-0.018	0.020
1.5	-0.015	-0.015	0.015

Similar to the lattice structure, the canonical part was compensated on the numerical models with different LLTs (LL05, LL10, and LL15) individually. The as-built compensated parts are shown in Figure 5.8(b). The distortions from the measurement (EXP - COMP) and simulation (SIM - COMP) are shown in Figure 5.9(b). Compared with the design shape, the compensated shape can significantly decrease distortion. As listed in Table 5.6 and visualized in Figure 5.10, the experimental measurement shows that the proposed compensation method can reduce up to 89.5% in maximum distortion (EXP - COMP - LL10) and 77.8% in average distortion (EXP - COMP - LL05) of the canonical part. Similar to the lattice structure, the overall reduction of the printed part is lower than that of the corresponding FE models, regardless of the LLTs used. For example, the simulation SIM - COMP - LL15 exhibits a distortion reduction of 94.8% for the maximum value and 97.4% for the average value. However, the measurements of EXP - COMP - LL15 indicate the actual reductions are only 77.8% and 86.9%, respectively. These observations will be discussed further in Section 5.4.

Table 5.6 Distortion (absolute value) of the canonical part printed with the compensated shape

	Maximum (mm)	Reduction in max. (%)	Average (mm)	Reduction in avg. (%)
EXP - COMP:				
LL05	0.077	77.8	0.020	86.9
LL10	0.131	62.2	0.016	89.5
LL15	0.106	69.5	0.020	86.9
SIM - COMP:				
LL05	0.018	94.8	0.004	97.4
LL10	0.017	95.1	0.006	96.1
LL15	0.013	96.3	0.006	96.1

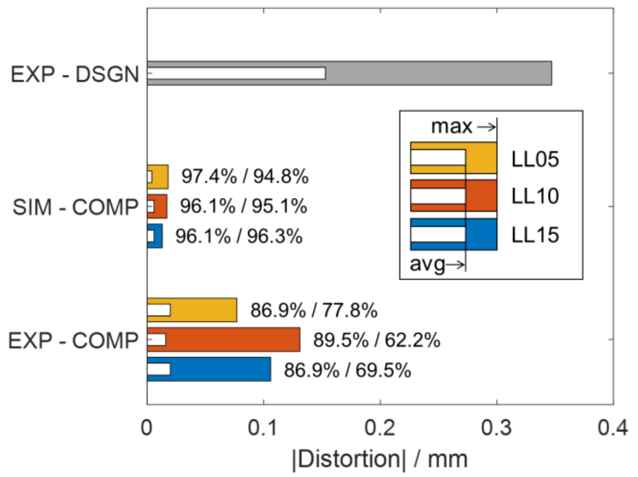

Figure 5.10 Maximum and average distortion (absolute value) of the canonical part. The percentages next to the bars represent the reduction in avg. (left) and max. (right) distortion with respect to EXP - DSGN.

In summary, the proposed compensation method has shown significant promise in reducing the geometric disparity between the as-built and design shapes. In the case of the lattice structure, experimental results show that it achieves a reduction of up to 82.5% in maximum distortion and up to 80.5% in average distortion. Similarly, for the canonical part, the method results in a reduction of up to 77.8% for maximum distortion and up to 89.5% for average distortion.

5.4 Discussion

5.4.1 Influence of Lumped Layer Thickness (LLT) in Finite Element (FE) Models

In theory, the most accurate way to predict part distortion using the IS method is to set the LLT equal to the thickness of a real print layer of the L-PBF process. However, this is not feasible due to the exceedingly high computational costs [182]. In part-scale FE simulations, it is common practice to utilize a lumped layer to model multiple real print layers. However, this simplification ignores the fact that the simulated stress fields differ between models based on sequentially activating multiple layers (layer-by-layer) and activating these layers simultaneously (i.e., one-shot) [60]. Liang et al. [48] reported that, at the same IS values, varying the LLT in the FE model resulted in different deformations. This observation is further supported by the current study, as evidenced by the distinct calibrated IS values for LLT of 0.5 mm, 1.0 mm, and 1.5 mm (refer to Table 5.5).

In order to compensate for the error caused by the LLT, Ref. [182] proposed an enhanced layer lumping method, in which the IS values were kept unchanged, whereas strength of the material in each lumped layer was adjusted according to its activation sequence. As an alternative, in this study, the IS values are calibrated individually for each LLT using experimental measurements, while the material properties are kept unchanged.

According to simulation results in Table 5.6 and Figure 5.10, the compensated geometries obtained by simulation based on different LLTs (SIM - COMP - LL05/LL10/LL15) exhibit comparable levels of distortion reduction, ranging from 94.8% to 96.3% for maximum distortion and from 96.1% to 97.4% for average distortion, respectively. The difference in reduction among the three LLTs is less than 1.5%, meaning that the LLT has little effect on the simulated distortion reduction. This finding demonstrates the robustness of the proposed compensation approach.

However, the printed compensated geometries (EXP - COMP - LL05/LL10/LL15) reveal that the actual distortion reduction may depend on the LLT. More specifically, the reduction ranges from 62.2% to 77.8% in maximum distortions, a 15.6% difference. This difference could be attributed to representing curvy surfaces with sharp transitions in the compensated shape (i.e., FE mesh), which will be discussed next.

5.4.2 Influence of Curvy Surfaces in Trial and Compensated Shapes

For both the lattice structure and canonical part, the actual distortion reduction achieved in experiments (EXP - COMP) is generally worse than that obtained in simulations (SIM - COMP). In addition, the actual distortion reduction for the canonical part is related to the LLT. These observed results could be attributed to the curvy surfaces that arise in the geometric representation of the trial and compensated geometries.

Both trial and compensated geometries are generated by adding a pre-deformation to the nodes of the FE mesh of the design geometry, which is originally represented by high-resolution STL discretization. The pre-deformation in trial geometries is proportional to the distortion of the design (see Equation (5.11)), while in compensated geometries, it is computed by the GPR model. Taking the canonical part as an example, the smooth and vertical outer side surface in the design shape has sharp transitions (e.g., two surface curves joining to form a sharp edge) in the trial and compensated shapes, as shown in red circled regions in Figure 5.11. The presence of abrupt transitions has two effects on the compensation method: (1) discretization error in geometric representation and (2) modeling error involving different process parameters.

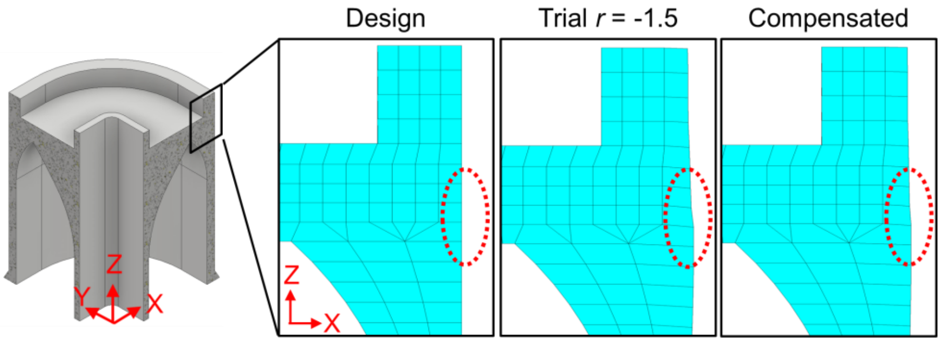

Figure 5.11 Outer side surface profiles in different canonical geometries (LLT = 1.5 mm).

The discretization error comes from the use of FE models in the compensation framework. A part is sliced into many lumped layers in the build direction in FE models. The discretization error can be ignored for vertically smooth surfaces (in the build direction). But for vertically curvy surfaces with sharp transitions, the larger the difference between the LLT and the real print layer thickness, the larger the discretization error in representing these surfaces. For example, the true compensated geometry may have fine geometric details on the outer side surface that a coarse mesh with a large LLT cannot represent. This can explain why the case of LLT = 0.5 mm (LL05) has better compensation performance in experiments than the cases of LLT = 1.0 mm (LL10) and 1.5 mm (LL15). Specifically, LL05 has a reduction of 77.8% in maximum distortion, while LL10 has 66.2% and LL15 has 69.5%. The fact that LL10 has a smaller reduction in maximum distortion than LL15 seems to be contradictory to the above analysis. This could be attributed to other factors in the printing process, such as dimensional errors [183].

The involvement of different process parameters during deposition is due to the slicing procedure on the STL model. Before being sent to the printer, an STL model is sliced into thousands of layers in the build direction according to the real print layer thickness, which is 40 μm in the current study, as shown in Figure 5.12. The EOS uses three sets of process parameters for 316L, chosen based on the location of the deposited area: up-skin, in-fill, and down-skin, as illustrated in Figure 5.12. The up-skin parameters are used for areas with no deposit above them, while the down-skin parameters are used for areas with no deposit beneath them. The in-fill parameters are adopted for areas where deposits exist both above and beneath. Studies have demonstrated that utilizing different process parameters can enable control over product qualities, such as surface finish and mechanical properties [184]. On the other hand, prior research has also shown that using different process parameters can significantly influence the distortion and IS values of a part [52, 185].

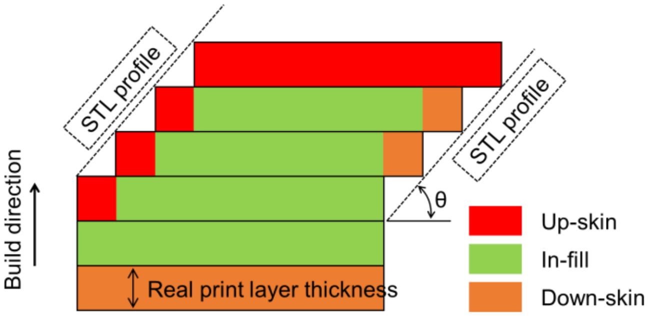

Figure 5.12 Schematic of up-skin, in-skin and down-skin areas. θ is the overhang angle of the side surface. (Adapted from Refs. [184, 186])

Taking the canonical part as an example, the outer side surface of the design shape is smooth and vertical (with an overhang angle $\theta = 90°$), meaning that most of the deposit is produced using in-fill parameters. However, as shown in Figure 5.11, the side surfaces of the trial and compensated geometries become curvy (as opposed to straight) in the build direction due to the superposition of pre-deformation, thereby exhibiting varying overhang angles. As a result, if these geometries were to be printed, the edges would be deposited using not only in-fill parameters but also up-skin and down-skin parameters. Consequently, the IS values, calibrated based on parts printed primarily using in-fill parameters, might be inaccurate when predicting the distortion of parts printed using up-skin and down-skin parameters. In other words, the IS model, calibrated via experimental measurement of the design geometry may not accurately predict the distortion of the trial and compensated geometries. This inconsistency helps to clarify why the real reduction of distortion seen in experiments generally falls below what is achieved in simulations.

As mentioned earlier, the as-built canonical part with the design shape has two distortion peaks along the measurement path, one at around Z = 52 mm and the other at around Z = 14 mm. Therefore, the compensated shapes also exhibit substantial pre-deformations in these two areas, as shown in Figure 5.13. The sharp transitions around these regions may require extensive up-skin and down-skin scanning, leading to inaccurate distortion predictions. The results presented in Figure 5.9(b) confirm there is a significant discrepancy between the experiment (EXP - COMP) and simulation (SIM - COMP) in terms of distortion in these two areas. Adopting region-wise IS values to account for the influence of varying process parameters could be a potential solution to this issue. However, this aspect requires extensive study and is beyond the scope of this study.

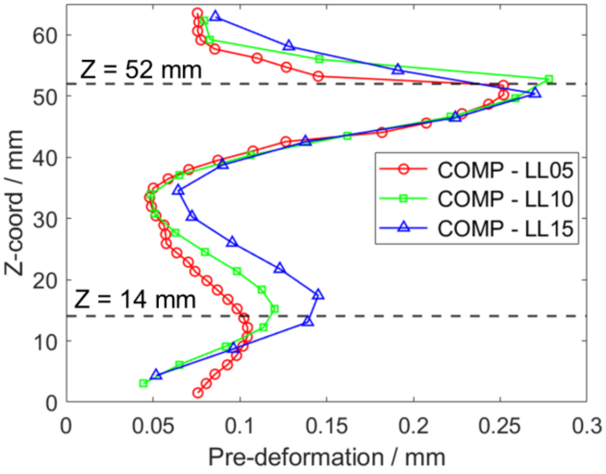

Figure 5.13 Pre-deformation along the measurement path in compensated geometries with different LLTs. The positive pre-deformations indicate that the point pre-deforms outward from the canonical center.

5.4.3 Influence of N_t and N_k

In this section, we perform a two-way analysis of variance (ANOVA) to investigate the influence of two factors on the accuracy of compensation: the number of trial geometries (N_t) and the number of deformation states (N_k). These factors mainly affect the GPR process. We select the FE model of the canonical part with an LLT of 1.5 mm ($N_L = 46$) to conduct compensations and calculate the average distortion along the measurement path (see Figure 5.3(b)), which serves as the response variable in the ANOVA.

Each factor has three levels, as detailed in Table 5.7. The number of trial geometries is set to be 0 (only the design geometry), 1 (one trial geometry with a scaling factor of $r_1 = -1.5$), and 3 (three trial geometries with scaling factors of $r_1 = -1.5$, $r_2 = -1.0$, and $r_3 = -0.5$). The number of deformation states is set to be 2 ($k = 0, 46$), 24 ($k = 0, 2, 4, \cdots, 46$), and 47 ($k = 0, 1, 2, \cdots, 46$). A Taguchi orthogonal array corresponding to these two factors and three levels is generated for the experimental design, as illustrated in Table 5.8. The number of experiments is 9 (Run #1-9). It is worth noting that the number of retained principal components N_p is not considered a factor here because its value depends on N_t and N_k. For each combination of N_t and N_k, the N_p is determined by Equation (5.15) and provided in Table 5.8.

After conducting numerical experiments, we extract the distortion of the compensated part along the measurement path, as shown in Figure 5.14. The positive distortion indicates that points on the measurement path deform outwards from the canonical center. We then calculate the absolute average distortion, the results of which are presented in Table 5.8 and Figure 5.15.

Table 5.7 ANOVA factor

Factor	Level
N_t	0, 1, 3
N_k	2, 24, 47

Table 5.8 Taguchi orthogonal array and corresponding results

Run #	N_t	N_k	N_p	Avg. distortion (mm)
1	0	2	1	0.200
2	0	24	6	0.196
3	0	47	6	0.194
4	1	2	1	0.109
5	1	24	7	0.026
6	1	47	8	0.032
7	3	2	1	0.004
8	3	24	5	0.007
9	3	47	5	0.006

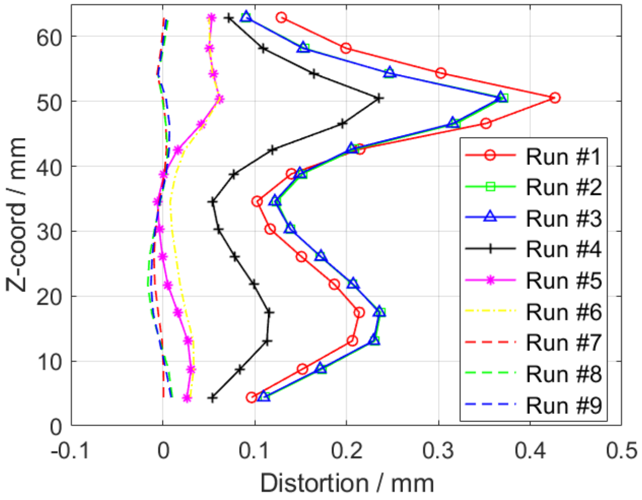

Figure 5.14 Distortion results for the canonical part printed with compensated shape in ANOVA.

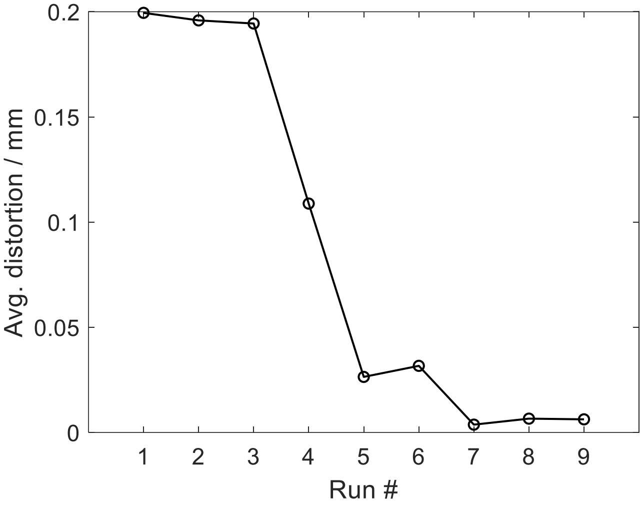

Figure 5.15 Average distortion for the canonical part printed with compensated shape in ANOVA.

Runs #1, #2, and #3 involve only the design shape and do not include any trial geometries ($N_t = 0$). Regardless of the number of deformation states (N_k), these runs deliver comparable average distortions, falling between 0.194 mm and 0.200 mm. Considering that the average distortion of the design shape itself is -0.174 mm (see SIM - DSGN - LL15), these three cases show a substantial overcompensation, which emphasizes the inadequacy of excluding trial geometries in the compensation process. Runs #4, #5, and #6, on the other hand, each includes a single trial geometry ($N_t = 1$). The overall performance for these three runs is better than that of runs without trial geometries, suggesting that incorporating trial geometries enhances the effectiveness of the GPR modeling. Finally, runs #7, #8, and #9, which include three trial geometries each ($N_t = 3$), exhibit average distortions of less than 0.007 mm, clearly underlining the significance of including trial geometries in the GPR modeling process.

In the present ANOVA, the interaction effect is not measured due to the absence of replications, which means there are no repeated observations or experiments for each combination of N_t and N_k. The ANOVA is carried out using MATLAB `anova2` function [187], which provides the F-statistic and p-value for each factor, as listed in Table 5.9. Assuming a significance level $\alpha = 0.05$, a p-value of 0.002 for N_t indicates its statistical significance, whereas a p-value of 0.429 for N_k suggests that it is not statistically significant.

Note that although N_k is not statistically significant according to ANOVA, it can still influence the compensation to a certain degree. For instance, in runs where $N_t = 1$, setting $N_k = 1$ results in an average distortion of 0.109 mm (Run #4), while setting $N_k = 24$ and 47 lead to average distortions around 0.029 mm (Run #5 and #6), only 27% of the former. Conversely, when N_t is either too low (i.e., 0) or too high (i.e., 3), the variation in N_k seems to have less impact on compensation performance.

Table 5.9 Statistic results of ANOVA

Factor	F-statistic	p-value
N_t	42.07	0.002
N_k	1.05	0.429

Overall, the compensation accuracy improves as the number of trial geometries increases. Similar observations were reported in Ref. [174], where the compensation method is applied to the sintering process. From the perspective of ML, the use of trial geometries increases the variability of the deformation dataset, thereby enhancing the capacity of the GPR model to learn the deformation patterns of the object.

In contrast, the number of deformation states is deemed insignificant to the compensation results. Run #7 only has two deformation states, namely the initial and final, but still yields an average distortion as small as 0.004 mm. This can be attributed to the characteristic of the L-PBF process, where the distortion is relatively small compared to the size of the part. For example, in the as-built canonical part, the maximum distortion along the measurement path is merely 0.347 mm, which accounts for approximately 0.4% of the part width and length (81.61 mm). Given the relatively small deformation in the final state, the evolution path of the deformation (intermediate states) becomes less important. Khan et al. [117] proposed an analytical model to describe the residual stress distribution in L-PBF parts. They assumed that the deposition of a new layer would induce linear changes in the residual stress within the previously deposited material. The residual stress this model predicted aligns well with numerical prediction and experimental measurement. Similarly, in the current study, when only the initial and final deformation states are provided ($N_k = 2$), the underlying assumption is that the deformation follows a linear progression, which is considered to be a good approximation for the L-PBF process based on the discussion above.

However, it is important to note that this linear assumption may not be valid for other AM processes, such as sintering in binder jetting, due to the significant change in part shape during the process. In such cases, it becomes necessary to incorporate multiple intermediate states to capture the non-linearity accurately in the deformation evaluation.

5.5 Conclusions

This research proposed a data-driven-based deformation compensation framework for L-PBF processes. The framework starts with utilizing the experimentally calibrated IS method to generate a deformation dataset. Next, GPR models are trained using the dataset to predict the compensated geometry. Finally, an STL file of the compensated geometry is created and sent to the printer for manufacturing. The key findings of this research are summarized as follows:

(1) Compared to the as-built design shape, the proposed compensation method achieves reductions of up to 82.5% in maximum distortion and 80.5% in average distortion for a lattice structure. In the case of a canonical part, the maximum and average distortion

reduction can reach up to 77.8% and 89.5%, respectively. These results provide strong validation for the effectiveness of the proposed method.

(2) The LLT of the FE model has a negligible impact on the simulated distortion reduction but can affect the actual reduction due to the discretization error between the FE mesh and the real part. Overall, the compensation accuracy of the canonical part with an LLT of 0.5 mm is better than that with LLTs of 1.0 mm and 1.5 mm, as it renders a smoother outer surface.

(3) The distortion reduction achieved in experiments is generally poorer compared to simulations. This discrepancy can be traced back to the inaccuracies of the IS values when dealing with trial and compensated geometries, which feature curvy outer surfaces in the build direction due to pre-deformation. Depositing these curvy surfaces with sharp transitions requires substantial use of up-skin and down-skin process parameters, along with in-fill parameters. The IS values, which are calibrated mainly based on in-fill process parameters, may not be suitable in this case.

(4) The ANOVA analysis reveals that the number of trial geometries significantly influences the compensation results for L-PBF processes. In general, a higher number of trial geometries leads to a larger reduction in distortion. On the other hand, due to the assumption of a linear progression of deformation induced in L-PBF, the number of deformation states does not have statistical significance on the compensation outcomes.

6.0 Conclusions

6.1 Main Contributions

The research works in this dissertation are mainly focused on improving the IS method in L-PBF and wire-arc DED processes for predicting residual stress and deformation, with applications in recoater interference prediction and distortion compensation. The main contributions of this research are summarized as follows:

(1) **A new implementation procedure for the MIS method is proposed to improve the simulation accuracy of residual stress without degrading the residual deformation prediction.** Previously, part-scale simulation in the MIS method utilized mechanical properties solely at ambient temperature, which proved to be inaccurate for predicting residual stress. The new procedure adds one more solution step employing mechanical properties at an elevated temperature determined from the IS extraction step. Both numerical and experimental studies are conducted to validate the proposed new implementation procedure. It shows that the MIS-based simulation with the new procedure can predict both residual stress and deformation of as-built L-PBF metal parts with good accuracy.

(2) **The MIS method is extended to use temperature-dependent ISs to capture the effect of heat accumulation commonly observed in large parts built by wire-arc DED.** Previously, the MIS method could not account for heat accumulation in the wire-arc DED process. In the extended method, instead of loading constant ISs layer-by-layer, each layer is divided into several segments according to the deposition path and sequentially loads

temperature-dependent ISs based on the interpass temperature of the build. A flash heating simulation involving transient thermal analysis is added to obtain the interpass temperature. The proposed temperature-dependent MIS method has been experimentally validated. Compared with the constant MIS method, the new method reduces the stress prediction error from 46.5% to 8.7% for a 112 mm small wall and from 19.5% to 6.9% for a 250 mm large wall. Both of them are built with Ti6Al4V. The prediction error in maximum deformation of the large wall is reduced from 29.7% to 7.9%.

(3) **An integrated simulation and experimental framework to predict potential recoater interference for a given part designed for L-PBF fabrication.** In prior studies employing numerical simulations to predict recoater interference, the criterion for defining interference has not been explicitly established. Furthermore, these studies did not account for deformation caused by the edge effect — the formation of elevated edges resulting from melt pool dynamics — due to constraints in model fidelity at the part scale. In the newly proposed framework, the recoater interference is defined to occur when the deformation of the part in the build direction exceeds the thickness of a newly spread powder layer after recoating. The largest deformation in the build direction is assumed to occur at the edge of a part and is postulated to be the sum of two contributions: global thermal deformation and local edge deformation. The global thermal deformation, generated by the relaxation of thermal stresses induced by the rapid laser melting and solidification over the entire part, is predicted using the MIS method. A key novelty in this work lies in employing location-dependent ISs in the MIS method to simulate the global thermal deformation of overhangs, which shows a 60% improvement in prediction accuracy compared with that using constant ISs. On the other hand, the local edge

deformation, associated with melt pool dynamics near the edge, is estimated by reconciling the MIS simulated and experimentally measured deformation on several overhang wedges. The validity of the proposed framework for predicting recoater interference is confirmed by experiments on different part geometries with overhangs.

(4) **A data-driven distortion compensation framework for the L-PBF process is presented.** Rather than adopting the iterative approach for solving the compensation problem as seen in ANSYS and Autodesk Fusion 360 Netfabb, the proposed framework employs the experimentally-calibrated IS method to generate a dataset and utilizes the Gaussian process regression to create the compensated geometry. The effectiveness of the proposed method is confirmed by experimental measurements, which show a reduction in maximum distortions by up to 82.5% for a lattice structure and up to 77.8% for a canonical part. Furthermore, the compensation results indicate that (i) the lumped layer thickness of the FE model has little impact on the simulated reduction in distortion but can notably affect the experimental reduction in distortion; (ii) the discrepancy between the simulated and experimental compensation performance can be attributed to the curvy surfaces with sharp transitions in the trial and compensated shapes resulting from the pre-deformation; (iii) the number of trial geometries considerably affects the compensation results, as indicated by the analysis of variance, while the number of deformation states does not have a statistically significant impact.

6.2 Future Works

While this dissertation demonstrates that the IS method has been refined for more accurate residual stress and deformation prediction for L-PBF and wire-arc DED processes and can be effectively applied to recoater interference prediction and distortion compensation, there remains room for further development of the proposed models and frameworks. The potential future works based on the research works in this dissertation are summarized below:

(1) **Development of comprehensive material constitutive models.** In the present work involving thermomechanical analysis, the mechanical behavior of the deposited material is assumed to be ideally plastic for simplification, which is a possible source of error in the prediction of residual stress and deformation [87]. Therefore, future efforts can be devoted to developing more comprehensive material constitutive models to include more physics phenomena and improve the modeling accuracy, such as strain hardening, flow softening, microstructure evolution, and cracking.

(2) **Development of data-driven distortion compensation models.** The data flow is unidirectional in the proposed data-driven framework for distortion compensation. Initially, experimentally measured deformations are used to calibrate the numerical model by optimizing the ISs. The calibrated model is then used to generate training data for GPR. This approach does not account for errors and uncertainties inherent in the measurement, calibration, and optimization processes. Multi-fidelity modeling [188, 189], which can simultaneously leverage high-fidelity measurement data and low-fidelity simulation results, offers a promising solution. This modeling approach can not only predict part deformation but also provide associated uncertainties. Therefore, future work could focus

on integrating multi-fidelity modeling into the distortion compensation model to enhance its accuracy and reliability.

(3) **Development of recoater interference prediction models.** In the present framework for predicting the recoater interference, the local edge deformation is determined by reconciling experimentally measured deformation with numerically simulated deformation of overhang wedges. Due to limitations in our modeling fidelity, we assume this deformation to be constant across different overhang angles, as our current model does not fully capture the influence of these angles on local edge deformation. Future work could therefore be directed towards developing a micro-scale modeling approach to study and quantitatively calculate surface elevation caused by the edge effect. Additionally, developing high-fidelity numerical modeling could enable the exploration of the collision between the recoater blade and the overhang tip, providing valuable insights for predicting recoater crashes.

Appendix

Appendix A Material Properties of 316L and 17-4PH

Material properties of 316L and 17-4PH [71, 74-76] used in the simulation are listed as follows:

Appendix Table 1 Constant material properties of 316L and 17-4PH used in the simulation

	316L	17-4PH
Solidus point T_S	1360 °C	1432 °C
Liquidus point T_L	1450 °C	1487 °C
Latent heat of fusion	270 kJ/kg	270 kJ/kg
Poisson’s ratio	0.3	0.3

Appendix Table 2 Temperature-dependent material properties of 316L used in the simulation

Temperature (°C)	Density (kg/m^3)	Heat conductivity (W/mK)	Specific heat (J/Kg°C)	Coefficient of thermal expansion (10^{-6})	Yield strength (MPa)	Young's modulus (GPa)
25	7948	13.3	467	14.3	520	196
204	7881	17.6	519	15.6	494	165
315	7826	19.4	539	-	353	154
371	7796	20.9	552	-	309	148
427	7770	22.0	561	16.9	287	142
482	7742	22.9	567	-	257	136
538	7711	23.6	576	-	236	128
650	7651	24.7	596	18.1	171	114
950	7487	28.3	648	-	40	62
1102	7392	29.0	666	19.3	40	62
1395	7264	31.9	717	19.5	40	62

Appendix Table 3 Temperature-dependent material properties of 17-4PH used in the simulation

Temperature (°C)	Density (kg/m^3)	Heat conductivity (W/mK)	Specific heat (J/Kg°C)	Coefficient of thermal expansion (10^{-6})	Yield strength (MPa)	Young's modulus (GPa)
25	7717	11.3	-	10.7	1158	205
204	-	12.9	442	11.4	958	194
315	7657	15.3	547	11.6	931	187
371	-	16.5	623	11.7	903	183
427	-	17.7	673	11.9	889	176
482	7623	19.1	723	11.7	814	173
538	-	19.9	754	-	696	165
650	7585	21.8	881	-	283	149
950	7460	26.3	637	11.7	104	110
1102	7400	28.4	694	13.4	104	78
1395	7276	32	814	15.1	104	78

Appendix B Von Mises Stress Data for L-bracket and Canonical Part

Appendix Table 4 Von Mises stress (in MPa) at different locations on top of the L-bracket with 316L

Location	ANSYS AM	MIS-EXT	MIS-NEW	EXP-ALT	EXP-ROT
P1	116	281	113	40 ± 25	171 ± 36
P2	136	504	132	179 ± 27	231 ± 23
P3	84	281	112	239 ± 30	210 ± 42
P4	115	498	152	226 ± 43	179 ± 39
P5	174	520	166	207 ± 34	164 ± 31
P6	143	498	154	190 ± 38	236 ± 35
P7	148	503	181	165 ± 23	117 ± 31
P8	174	520	164	214 ± 26	156 ± 29
P9	83	277	113	118 ± 27	113 ± 20
P10	106	505	157	148 ± 34	268 ± 26
P11	183	520	173	153 ± 27	206 ± 30
P12	134	505	156	103 ± 28	246 ± 28
P13	60	359	119	93 ± 29	166 ± 32
P14	105	504	140	106 ± 51	107 ± 35
P15	72	358	119	148 ± 41	220 ± 42

Appendix Table 5 Von Mises stress (in MPa) at different locations on top of the L-bracket with 17-4PH

Location	ANSYS AM	MIS-EXT	MIS-NEW	EXP-ALT	EXP-ROT
P1	437	488	219	444 ± 46	338 ± 93
P2	511	1095	276	340 ± 64	482 ± 94
P3	318	488	219	418 ± 72	245 ± 72
P4	385	1110	395	462 ± 73	305 ± 85
P5	585	1157	411	238 ± 78	108 ± 90
P6	535	111	405	443 ± 82	539 ± 88
P7	505	1127	496	634 ± 139	526 ± 73
P8	530	1157	397	524 ± 87	508 ± 95
P9	317	479	219	119 ± 72	540 ± 69
P10	380	1125	396	505 ± 109	588 ± 116
P11	603	1158	436	337 ± 104	515 ± 74
P12	464	1124	392	568 ± 104	507 ± 91
P13	229	648	233	441 ± 57	516 ± 66
P14	377	1115	313	607 ± 100	330 ± 61
P15	274	648	233	226 ± 89	286 ± 102

Appendix Table 6 Von Mises stress (in MPa) at different locations on top of the canonical part with 316L

Location	ANSYS AM	MIS-EXT	MIS-NEW	EXP-1	EXP-2
P1	278	512	308	148 ± 37	252 ± 21
P2	186	416	254	189 ± 38	209 ± 34
P3	215	435	268	277 ± 29	192 ± 17
P4	244	462	284	245 ± 36	245 ± 46
P5	277	512	308	325 ± 16	307 ± 35
P6	186	418	255	196 ± 32	294 ± 48
P7	216	435	268	214 ± 23	255 ± 15
P8	245	463	284	360 ± 50	231 ± 45
P9	287	512	304	299 ± 42	274 ± 28
P10	155	371	224	209 ± 53	249 ± 47
P11	198	416	256	192 ± 27	206 ± 35
P12	261	462	305	326 ± 41	226 ± 29

Appendix C Von Mises Stress Data for Small and Large Wall

Appendix Table 7 Von Mises stress (MPa) comparison of the small wall

Location	XRD	Detailed process simulation w/o SSPT		Detailed process simulation w/ SSPT		MIS constant		MIS temperature-dependent	
		Value	Error	Value	Error	Value	Error	Value	Error
P1	181 ± 115	89	-50.8%	112	-38.1%	353	95.0%	216	19.3%
P2	1018 ± 97	1078	5.9%	1046	2.8%	1187	16.6%	1086	6.7%
P3	490 ± 110	394	-19.6%	482	-1.6%	353	-28.0%	489	-0.2%
Average			25.4%		14.2%		46.5%		8.7%

Appendix Table 8 Von Mises stress (MPa) comparison of the large wall

Location	XRD	MIS constant		MIS temperature-dependent	
		Value	Error	Value	Error
P1	747 ± 135	323	-56.8%	665	-11.0%
P2	530 ± 107	523	-1.3%	544	2.6%
P3	549 ± 76	550	0.2%	492	-10.4%
P4	487 ± 113	523	7.4%	457	-6.2%
P5	472 ± 98	323	-31.6%	492	4.2%
Average			19.5%		6.9%

Bibliography

[1] *Additive manufacturing—General principles—Fundamentals and vocabulary*, ISO/ASTM, Geneva, Switzerland, 2021.

[2] R. Ganeriwala *et al.*, "Evaluation of a thermomechanical model for prediction of residual stress during laser powder bed fusion of Ti-6Al-4V," *Additive Manufacturing,* vol. 27, pp. 489-502, 2019.

[3] J. L. Bartlett and X. Li, "An overview of residual stresses in metal powder bed fusion," *Additive Manufacturing,* vol. 27, pp. 131-149, 2019.

[4] J. Spencer, P. Dickens, and C. Wykes, "Rapid prototyping of metal parts by three-dimensional welding," *Proceedings of the Institution of Mechanical Engineers, Part B: Journal of Engineering Manufacture,* vol. 212, no. 3, pp. 175-182, 1998.

[5] S. Srivastava, R. K. Garg, V. S. Sharma, and A. Sachdeva, "Measurement and Mitigation of Residual Stress in Wire-Arc Additive Manufacturing: A Review of Macro-Scale Continuum Modelling Approach," *Archives of Computational Methods in Engineering,* vol. 28, no. 5, pp. 3491-3515, 2020, doi: 10.1007/s11831-020-09511-4.

[6] D. Chakraborty, T. Tirumala, S. Chitral, B. Sahoo, D. Kiran, and P. A. Kumar, "The state of the art for wire arc additive manufacturing process of titanium alloys for aerospace applications," *Journal of Materials Engineering and Performance,* vol. 31, no. 8, pp. 6149-6182, 2022.

[7] M. Chaturvedi, E. Scutelnicu, C. C. Rusu, L. R. Mistodie, D. Mihailescu, and A. V. Subbiah, "Wire Arc Additive Manufacturing: Review on Recent Findings and Challenges in Industrial Applications and Materials Characterization," *Metals,* vol. 11, no. 6, 2021, doi: 10.3390/met11060939.

[8] C. Ma *et al.*, "Investigation of the in-situ gas cooling of carbon steel during wire and arc additive manufacturing," *Journal of Manufacturing Processes,* vol. 67, pp. 461-477, 2021, doi: 10.1016/j.jmapro.2021.05.022.

[9] S. W. Williams, F. Martina, A. C. Addison, J. Ding, G. Pardal, and P. Colegrove, "Wire + Arc Additive Manufacturing," *Materials Science and Technology*, vol. 32, no. 7, pp. 641-647, 2016, doi: 10.1179/1743284715y.0000000073.

[10] TWI. "MIG/MAG - DEVELOPMENTS IN LOW HEAT INPUT TRANSFER MODES." https://www.twi-global.com/technical-knowledge/job-knowledge/mig-mag-developments-in-low-heat-input-transfer-modes-133 (accessed 03-13, 2022).

[11] W. E. King *et al.*, "Laser powder bed fusion additive manufacturing of metals; physics, computational, and materials challenges," *Applied Physics Reviews*, vol. 2, no. 4, 2015, doi: 10.1063/1.4937809.

[12] "Gas Metal Arc Welding (GMAW) or MIG Welding." http://mechanicalinventions.blogspot.com/2012/11/gas-metal-arc-welding-gmaw-or-mig.html (accessed 11-08, 2023).

[13] S. H. Khajavi, J. Partanen, and J. Holmström, "Additive manufacturing in the spare parts supply chain," *Computers in Industry*, vol. 65, no. 1, pp. 50-63, 2014, doi: 10.1016/j.compind.2013.07.008.

[14] T. Pereira, J. V. Kennedy, and J. Potgieter, "A comparison of traditional manufacturing vs additive manufacturing, the best method for the job," *Procedia Manufacturing*, vol. 30, pp. 11-18, 2019.

[15] J. P. Oliveira, A. D. LaLonde, and J. Ma, "Processing parameters in laser powder bed fusion metal additive manufacturing," *Materials & Design*, vol. 193, 2020, doi: 10.1016/j.matdes.2020.108762.

[16] M. F. Zaeh and G. Branner, "Investigations on residual stresses and deformations in selective laser melting," *Production Engineering*, vol. 4, no. 1, pp. 35-45, 2009, doi: 10.1007/s11740-009-0192-y.

[17] N. Nadammal *et al.*, "Critical role of scan strategies on the development of microstructure, texture, and residual stresses during laser powder bed fusion additive manufacturing," *Additive Manufacturing*, vol. 38, p. 101792, 2021.

[18] M. McConaha and S. Anand, "Additive manufacturing distortion compensation based on scan data of built geometry," *Journal of Manufacturing Science and Engineering*, vol. 142, no. 6, p. 061001, 2020.

[19] M. D. Barath Kumar and M. Manikandan, "Assessment of Process, Parameters, Residual Stress Mitigation, Post Treatments and Finite Element Analysis Simulations of Wire Arc Additive Manufacturing Technique," *Metals and Materials International,* vol. 28, no. 1, pp. 54-111, 2021, doi: 10.1007/s12540-021-01015-5.

[20] L. Han, F. W. Liou, and S. Musti, "Thermal Behavior and Geometry Model of Melt Pool in Laser Material Process," *Journal of Heat Transfer,* vol. 127, no. 9, pp. 1005-1014, 2005, doi: 10.1115/1.2005275.

[21] A. Bauereiß, T. Scharowsky, and C. Körner, "Defect generation and propagation mechanism during additive manufacturing by selective beam melting," *Journal of Materials Processing Technology,* vol. 214, no. 11, pp. 2522-2528, 2014, doi: 10.1016/j.jmatprotec.2014.05.002.

[22] Q. Chen *et al.*, "Elucidating the effect of preheating temperature on melt pool morphology variation in Inconel 718 laser powder bed fusion via simulation and experiment," *Additive Manufacturing,* 2020, doi: 10.1016/j.addma.2020.101642.

[23] J. Goldak, A. Chakravarti, and M. Bibby, "A new finite element model for welding heat sources," *Metallurgical transactions B,* vol. 15, no. 2, pp. 299-305, 1984.

[24] V. Pavelic, R. Tanbakuchi, O. A. Uyehara, and P. S. Myers, "Experimental and computed temperature histories in gas tungsten arc welding of thin plates," *Welding Journal Research Supplement,* vol. 48, pp. 296-305, 1969.

[25] Y. Li, K. Zhou, P. Tan, S. B. Tor, C. K. Chua, and K. F. Leong, "Modeling temperature and residual stress fields in selective laser melting," *International Journal of Mechanical Sciences,* vol. 136, pp. 24-35, 2018, doi: 10.1016/j.ijmecsci.2017.12.001.

[26] P. Tan, F. Shen, B. Li, and K. Zhou, "A thermo-metallurgical-mechanical model for selective laser melting of Ti6Al4V," *Materials & Design,* vol. 168, 2019, doi: 10.1016/j.matdes.2019.107642.

[27] J. Ding, P. Colegrove, J. Mehnen, S. Williams, F. Wang, and P. S. Almeida, "A computationally efficient finite element model of wire and arc additive manufacture," *The International Journal of Advanced Manufacturing Technology,* vol. 70, no. 1-4, pp. 227-236, 2013, doi: 10.1007/s00170-013-5261-x.

[28] L.-E. Lindgren, A. Lundbäck, M. Fisk, R. Pederson, and J. Andersson, "Simulation of additive manufacturing using coupled constitutive and microstructure models," *Additive Manufacturing,* vol. 12, pp. 144-158, 2016, doi: 10.1016/j.addma.2016.05.005.

[29] X. Liang, L. Cheng, Q. Chen, Q. Yang, and A. C. To, "A modified method for estimating inherent strains from detailed process simulation for fast residual distortion prediction of single-walled structures fabricated by directed energy deposition," *Additive Manufacturing,* vol. 23, pp. 471-486, 2018, doi: 10.1016/j.addma.2018.08.029.

[30] M. Bugatti and Q. Semeraro, "Limitations of the inherent strain method in simulating powder bed fusion processes," *Additive Manufacturing,* vol. 23, pp. 329-346, 2018, doi: 10.1016/j.addma.2018.05.041.

[31] D. Jia, F. Li, and Y. Zhang, "3D-printing process design of lattice compressor impeller based on residual stress and deformation," *Sci Rep,* vol. 10, no. 1, p. 600, Jan 17 2020, doi: 10.1038/s41598-019-57131-1.

[32] A. Yaghi, S. Afazov, A. Holloway, and W. Denmark, "Comparison of fast finite element modelling techniques for prediction of distortion and residual stresses in laser powder bed fusion," *Design and Manufacturing Simulation of Additive Manufacturing,* 2017.

[33] A. J. Dunbar, E. R. Denlinger, M. F. Gouge, and P. Michaleris, "Experimental validation of finite element modeling for laser powder bed fusion deformation," *Additive Manufacturing,* vol. 12, pp. 108-120, 2016, doi: 10.1016/j.addma.2016.08.003.

[34] M. Megahed, H.-W. Mindt, N. N'Dri, H. Duan, and O. Desmaison, "Metal additive-manufacturing process and residual stress modeling," *Integrating Materials and Manufacturing Innovation,* vol. 5, no. 1, pp. 61-93, 2016, doi: 10.1186/s40192-016-0047-2.

[35] Y. Ueda and K. Fukuda, "New measuring method of three-dimensional residual stresses in long welded joints using inherent strains as parameters—Lz method," 1989.

[36] Y. Ueda, K. Fukuda, K. Nakacho, and S. Endo, "A new measuring method of residual stresses with the aid of finite element method and reliability of estimated values," *Journal of the Society of Naval Architects of Japan,* vol. 1975, no. 138, pp. 499-507, 1975.

[37] Y. Ueda and M. Yuan, "Prediction of residual stresses in butt welded plates using inherent strains," 1993.

[38] N. Keller and V. Ploshikhin, "New Method for Fast Predictions on Residual Stress and Distortion of AM Parts," in *2014 International Solid Freeform Fabrication Symposium*, 2014: University of Texas at Austin.

[39] T. Mayer, G. Brändle, A. Schönenberger, and R. Eberlein, "Simulation and validation of residual deformations in additive manufacturing of metal parts," *Heliyon,* vol. 6, no. 5, p. e03987, 2020.

[40] J. Pellens, G. Lombaert, M. Michiels, T. Craeghs, and M. Schevenels, "Topology optimization of support structure layout in metal-based additive manufacturing accounting for thermal deformations," *Structural and Multidisciplinary Optimization,* vol. 61, no. 6, pp. 2291-2303, 2020.

[41] Z.-D. Zhang *et al.*, "Topology optimization parallel-computing framework based on the inherent strain method for support structure design in laser powder-bed fusion additive manufacturing," *International Journal of Mechanics and Materials in Design,* vol. 16, no. 4, pp. 897-923, 2020.

[42] G. Vastola, W. J. Sin, C. N. Sun, and N. Sridhar, "Design guidelines for suppressing distortion and buckling in metallic thin-wall structures built by powder-bed fusion additive manufacturing," *Materials & Design,* vol. 215, 2022, doi: 10.1016/j.matdes.2022.110489.

[43] M. Bayat, W. Dong, J. Thorborg, A. C. To, and J. H. Hattel, "A review of multi-scale and multi-physics simulations of metal additive manufacturing processes with focus on modeling strategies," *Additive Manufacturing,* vol. 47, 2021, doi: 10.1016/j.addma.2021.102278.

[44] P. Alvarez, J. Ecenarro, I. Setien, M. S. Sebastian, A. Echeverria, and L. Eciolaza, "Computationally efficient distortion prediction in powder bed fusion additive manufacturing," *Int. J. Eng. Res. Sci,* vol. 2, no. 10, pp. 39-46, 2016.

[45] I. Setien, M. Chiumenti, S. van der Veen, M. San Sebastian, F. Garciandía, and A. Echeverría, "Empirical methodology to determine inherent strains in additive manufacturing," *Computers & Mathematics with Applications,* vol. 78, no. 7, pp. 2282-2295, 2019, doi: 10.1016/j.camwa.2018.05.015.

[46] M. Siewert, F. Neugebauer, J. Epp, and V. Ploshikhin, "Validation of Mechanical Layer Equivalent Method for simulation of residual stresses in additive manufactured components," *Computers & Mathematics with Applications,* vol. 78, no. 7, pp. 2407-2416, 2019, doi: 10.1016/j.camwa.2018.08.016.

[47] X. Liang, Q. Chen, L. Cheng, Q. Yang, and A. To, "A modified inherent strain method for fast prediction of residual deformation in additive manufacturing of metal parts," in *2017 International Solid Freeform Fabrication Symposium*, 2017: University of Texas at Austin.

[48] X. Liang, Q. Chen, L. Cheng, D. Hayduke, and A. C. To, "Modified inherent strain method for efficient prediction of residual deformation in direct metal laser sintered components," *Computational Mechanics,* vol. 64, no. 6, pp. 1719-1733, 2019, doi: 10.1007/s00466-019-01748-6.

[49] Q. Chen *et al.*, "An inherent strain based multiscale modeling framework for simulating part-scale residual deformation for direct metal laser sintering," *Additive Manufacturing,* vol. 28, pp. 406-418, 2019, doi: 10.1016/j.addma.2019.05.021.

[50] Q. Chen, J. Liu, X. Liang, and A. C. To, "A level-set based continuous scanning path optimization method for reducing residual stress and deformation in metal additive manufacturing," *Computer Methods in Applied Mechanics and Engineering,* vol. 360, p. 112719, 2020.

[51] X. Liang, W. Dong, Q. Chen, and A. C. To, "On incorporating scanning strategy effects into the modified inherent strain modeling framework for laser powder bed fusion," *Additive Manufacturing,* 2020, doi: 10.1016/j.addma.2020.101648.

[52] X. Liang *et al.*, "Inherent strain homogenization for fast residual deformation simulation of thin-walled lattice support structures built by laser powder bed fusion additive manufacturing," *Additive Manufacturing,* vol. 32, 2020, doi: 10.1016/j.addma.2020.101091.

[53] H. T. Tran, Q. Chen, J. Mohan, and A. C. To, "A new method for predicting cracking at the interface between solid and lattice support during laser powder bed fusion additive manufacturing," *Additive Manufacturing,* vol. 32, 2020, doi: 10.1016/j.addma.2020.101050.

[54] H. T. Tran, X. Liang, and A. C. To, "Efficient prediction of cracking at solid-lattice support interface during laser powder bed fusion via global-local J-integral analysis based on modified inherent strain method and lattice support homogenization," *Additive Manufacturing,* vol. 36, 2020, doi: 10.1016/j.addma.2020.101590.

[55] J. H. Robinson, I. R. T. Ashton, E. Jones, P. Fox, and C. Sutcliffe, "The effect of hatch angle rotation on parts manufactured using selective laser melting," *Rapid Prototyping Journal,* vol. 25, no. 2, pp. 289-298, 2018.

[56] L. E. Lindgren, H. Runnemalm, and M. O. Näsström, "Simulation of multipass welding of a thick plate," *International journal for numerical methods in engineering,* vol. 44, no. 9, pp. 1301-1316, 1999.

[57] P. Michaleris, "Modeling metal deposition in heat transfer analyses of additive manufacturing processes," *Finite Elements in Analysis and Design,* vol. 86, pp. 51-60, 2014, doi: 10.1016/j.finel.2014.04.003.

[58] W. Dong, X. A. Jimenez, and A. C. To, "Temperature-dependent modified inherent strain method for predicting residual stress and distortion of Ti6Al4V walls manufactured by wire-arc directed energy deposition," *Additive Manufacturing,* vol. 62, p. 103386, 2023.

[59] W. Dong, X. Liang, Q. Chen, S. Hinnebusch, Z. Zhou, and A. C. To, "A new procedure for implementing the modified inherent strain method with improved accuracy in predicting both residual stress and deformation for laser powder bed fusion," *Additive Manufacturing,* vol. 47, 2021, doi: 10.1016/j.addma.2021.102345.

[60] Q. Lu, E. Beauchesne, and T. Liszka, "Enhancements to the inherent strain method for Additive Manufacturing analysis," *International Journal for Multiscale Computational Engineering,* vol. 17, no. 1, 2019.

[61] G. Yang *et al.*, "Effect of processing parameters on the density, microstructure and strength of pure tungsten fabricated by selective electron beam melting," *International Journal of Refractory Metals and Hard Materials,* vol. 84, p. 105040, 2019.

[62] N. Keller and V. Ploshikhin, "New method for fast predictions of residual stress and distortion of AM parts," in *Solid freeform fabrication symposium*, 2014, vol. 25.

[63] Q. Yang, P. Zhang, L. Cheng, Z. Min, M. Chyu, and A. C. To, "Finite element modeling and validation of thermomechanical behavior of Ti-6Al-4V in directed energy deposition additive manufacturing," *Additive Manufacturing,* vol. 12, pp. 169-177, 2016, doi: 10.1016/j.addma.2016.06.012.

[64] J. Ding, "Thermo-mechanical Analysis of Wire and Arc Additive Manufacturing Process," PhD, Cranfield University, 2012.

[65] D. De Baere *et al.*, "Thermo-mechanical modelling of stress relief heat treatments after laser-based powder bed fusion," *Additive Manufacturing,* vol. 38, p. 101818, 2021.

[66] E. R. Denlinger, J. Irwin, and P. Michaleris, "Thermomechanical Modeling of Additive Manufacturing Large Parts," *Journal of Manufacturing Science and Engineering,* vol. 136, no. 6, 2014, doi: 10.1115/1.4028669.

[67] L.-E. Lindgren, *Computational welding mechanics*. Elsevier, 2014.

[68] H. Ambarita, F. H. Napitupulu, and T. B. Sitorus, "Numerical study on melting process of Phase Change Material as thermal energy storage," in *IOP Conference Series: Materials Science and Engineering,* 2020, vol. 725, no. 1: IOP Publishing, p. 012051.

[69] E. Haque and P. Hampson, "Modelling phase change in a 3D thermal transient analysis," *The International Journal of Multiphysics,* vol. 8, no. 1, pp. 49-68, 2014.

[70] M. Biegler, B. Graf, and M. Rethmeier, "In-situ distortions in LMD additive manufacturing walls can be measured with digital image correlation and predicted using numerical simulations," *Additive Manufacturing,* vol. 20, pp. 101-110, 2018, doi: 10.1016/j.addma.2017.12.007.

[71] C. Li, Z. Y. Liu, X. Y. Fang, and Y. B. Guo, "On the Simulation Scalability of Predicting Residual Stress and Distortion in Selective Laser Melting," *Journal of Manufacturing Science and Engineering,* vol. 140, no. 4, 2018, doi: 10.1115/1.4038893.

[72] N. E. Hodge, R. M. Ferencz, and J. M. Solberg, "Implementation of a thermomechanical model for the simulation of selective laser melting," *Computational Mechanics,* vol. 54, no. 1, pp. 33-51, 2014, doi: 10.1007/s00466-014-1024-2.

[73] R. Sharma and A. Kumar, "Track-scale simulations of selective laser melting to investigate development and mitigation of thermal stresses," *Lasers in Manufacturing and Materials Processing,* vol. 6, pp. 464-492, 2019.

[74] K. C. Mills, *Recommended values of thermophysical properties for selected commercial alloys*. Woodhead Publishing, 2002.

[75] A. S. Sabau and W. D. Porter, "Alloy Shrinkage Factors for the Investment Casting of 17-4PH Stainless Steel Parts," *Metallurgical and Materials Transactions B,* vol. 39, no. 2, pp. 317-330, 2008, doi: 10.1007/s11663-007-9125-3.

[76] A. S. Wu, D. W. Brown, M. Kumar, G. F. Gallegos, and W. E. King, "An Experimental Investigation into Additive Manufacturing-Induced Residual Stresses in 316L Stainless

Steel," *Metallurgical and Materials Transactions A*, vol. 45, no. 13, pp. 6260-6270, 2014, doi: 10.1007/s11661-014-2549-x.

[77] *Standard Test Methods for Tension Testing of Metallic Materials*, ASTM, 2013.

[78] EOS. https://www.eos.info/en/additive-manufacturing/3d-printing-metal/dmls-metal-materials/stainless-steel (accessed 9 August, 2020).

[79] J. X. Fang *et al.*, "The effects of solid-state phase transformation upon stress evolution in laser metal powder deposition," *Materials & Design*, vol. 87, pp. 807-814, 2015, doi: 10.1016/j.matdes.2015.08.061.

[80] Z. Hu and J. Zhao, "Effects of martensitic transformation on residual stress of P91 welded joint," *Materials Research Express*, vol. 5, no. 9, 2018, doi: 10.1088/2053-1591/aad901.

[81] J. Li, Q. Wang, and P. Michaleris, "An Analytical Computation of Temperature Field Evolved in Directed Energy Deposition," *Journal of Manufacturing Science and Engineering*, vol. 140, no. 10, 2018, doi: 10.1115/1.4040621.

[82] D. Hu and R. Kovacevic, "Modelling and measuring the thermal behaviour of the molten pool in closed-loop controlled laser-based additive manufacturing," *Proceedings of the Institution of Mechanical Engineers, Part B: Journal of Engineering Manufacture*, vol. 217, no. 4, pp. 441-452, 2003.

[83] M. Labudovic, D. Hu, and R. Kovacevic, "A three dimensional model for direct laser metal powder deposition and rapid prototyping," *Journal of materials science*, vol. 38, no. 1, pp. 35-49, 2003.

[84] V. Vinokurov, "Welding stresses and distortion," *The British Library Board*, 1977.

[85] T. Mukherjee, W. Zhang, and T. DebRoy, "An improved prediction of residual stresses and distortion in additive manufacturing," *Computational Materials Science*, vol. 126, pp. 360-372, 2017, doi: 10.1016/j.commatsci.2016.10.003.

[86] P. S. Prevey, "X-ray diffraction residual stress techniques," *ASM International, ASM Handbook.*, vol. 10, pp. 380-392, 1986.

[87] E. Mirkoohi, H.-C. Tran, Y.-L. Lo, Y.-C. Chang, H.-Y. Lin, and S. Y. Liang, "Analytical mechanics modeling of residual stress in laser powder bed considering flow hardening and softening," *The International Journal of Advanced Manufacturing Technology,* vol. 107, no. 9-10, pp. 4159-4172, 2020, doi: 10.1007/s00170-020-05304-y.

[88] L. J. da Silva, D. M. Souza, D. B. de Araújo, R. P. Reis, and A. Scotti, "Concept and validation of an active cooling technique to mitigate heat accumulation in WAAM," *The International Journal of Advanced Manufacturing Technology*, vol. 107, no. 5-6, pp. 2513-2523, 2020, doi: 10.1007/s00170-020-05201-4.

[89] D. Fan, M. Gao, C. Li, J. Huang, and X. Yu, "Residual stress and microstructure properties by trailing cooling of argon gas of wire and arc additive manufacturing," *Journal of Manufacturing Processes,* vol. 77, pp. 32-39, 2022, doi: 10.1016/j.jmapro.2022.03.007.

[90] B. Wu *et al.*, "Effects of heat accumulation on the arc characteristics and metal transfer behavior in Wire Arc Additive Manufacturing of Ti6Al4V," *Journal of Materials Processing Technology,* vol. 250, pp. 304-312, 2017, doi: 10.1016/j.jmatprotec.2017.07.037.

[91] L. Vázquez, N. Rodríguez, I. Rodríguez, E. Alberdi, and P. Álvarez, "Influence of interpass cooling conditions on microstructure and tensile properties of Ti-6Al-4V parts manufactured by WAAM," *Welding in the World,* vol. 64, no. 8, pp. 1377-1388, 2020, doi: 10.1007/s40194-020-00921-3.

[92] X. Jimenez, W. Dong, S. Paul, M. A. Klecka, and A. C. To, "Residual Stress Modeling with Phase Transformation for Wire Arc Additive Manufacturing of B91 Steel," *Jom,* vol. 72, no. 12, pp. 4178-4186, 2020, doi: 10.1007/s11837-020-04424-w.

[93] J. Xiong, Y. Li, R. Li, and Z. Yin, "Influences of process parameters on surface roughness of multi-layer single-pass thin-walled parts in GMAW-based additive manufacturing," *Journal of Materials Processing Technology,* vol. 252, pp. 128-136, 2018, doi: 10.1016/j.jmatprotec.2017.09.020.

[94] T. Mishurova *et al.*, "Residual Stress and Microstructure of a Ti-6Al-4V Wire Arc Additive Manufacturing Hybrid Demonstrator," *Metals,* vol. 10, no. 6, 2020, doi: 10.3390/met10060701.

[95] B. Ahmad, X. Zhang, H. Guo, M. E. Fitzpatrick, L. M. S. C. Neto, and S. Williams, "Influence of Deposition Strategies on Residual Stress in Wire + Arc Additive Manufactured Titanium Ti-6Al-4V," *Metals,* vol. 12, no. 2, 2022, doi: 10.3390/met12020253.

[96] Y. Lee, Y. Bandari, P. Nandwana, B. T. Gibson, B. Richardson, and S. Simunovic, "Effect of Interlayer Cooling Time, Constraint and Tool Path Strategy on Deformation of Large Components Made by Laser Metal Deposition with Wire," *Applied Sciences*, vol. 9, no. 23, 2019, doi: 10.3390/app9235115.

[97] M. Bayat *et al.*, "Part-scale thermo-mechanical modelling of distortions in Laser Powder Bed Fusion–Analysis of the sequential flash heating method with experimental validation," *Additive Manufacturing*, vol. 36, p. 101508, 2020.

[98] M. Liu *et al.*, "A characteristic time-based heat input model for simulating selective laser melting," *Additive Manufacturing*, vol. 44, p. 102026, 2021.

[99] B. Nijhuis, H. Geijselaers, and A. H. van den Boogaard, "Efficient thermal simulation of large-scale metal additive manufacturing using hot element addition," *Computers & Structures*, vol. 245, p. 106463, 2021.

[100] S. M. Kelly, "Thermal and microstructure modeling of metal deposition processes with application to Ti-6Al-4V," PhD, Virginia Tech, 2004.

[101] R. Pederson, "Microstructure and phase transformation of Ti-6Al-4V," Luleå tekniska universitet, 2002.

[102] L. Xiong, G. Mi, C. Wang, G. Zhu, X. Xu, and P. Jiang, "Numerical Simulation of Residual Stress for Laser Welding of Ti-6Al-4V Alloy Considering Solid-State Phase Transformation," *Journal of Materials Engineering and Performance*, vol. 28, no. 6, pp. 3349-3360, 2019, doi: 10.1007/s11665-019-04135-7.

[103] C. Baykasoglu, O. Akyildiz, D. Candemir, Q. Yang, and A. C. To, "Predicting Microstructure Evolution During Directed Energy Deposition Additive Manufacturing of Ti-6Al-4V," *Journal of Manufacturing Science and Engineering*, vol. 140, no. 5, 2018, doi: 10.1115/1.4038894.

[104] W. Sun, F. Shan, N. Zong, H. Dong, and T. Jing, "A simulation and experiment study on phase transformations of Ti-6Al-4V in wire laser additive manufacturing," *Materials & Design*, vol. 207, 2021, doi: 10.1016/j.matdes.2021.109843.

[105] J. Ahn, E. He, L. Chen, R. C. Wimpory, J. P. Dear, and C. M. Davies, "Prediction and measurement of residual stresses and distortions in fibre laser welded Ti-6Al-4V considering phase transformation," *Materials & Design*, vol. 115, pp. 441-457, 2017, doi: 10.1016/j.matdes.2016.11.078.

[106] C. Baykasoğlu, O. Akyildiz, M. Tunay, and A. C. To, "A process-microstructure finite element simulation framework for predicting phase transformations and microhardness for directed energy deposition of Ti6Al4V," *Additive Manufacturing,* vol. 35, 2020, doi: 10.1016/j.addma.2020.101252.

[107] A. Crespo and R. Vilar, "Finite element analysis of the rapid manufacturing of Ti–6Al–4V parts by laser powder deposition," *Scripta Materialia,* vol. 63, no. 1, pp. 140-143, 2010, doi: 10.1016/j.scriptamat.2010.03.036.

[108] S. Babu, S. Kelly, E. Specht, T. Palmer, and J. Elmer, "Measurement of phase transformation kinetics during repeated thermal cycling of Ti-6Al-4V using time-resolved X-ray diffraction," in *International Conference on Solid-Solid Phase Transformations in Inorganic Materials 2005,* 2005.

[109] C. C. Murgau, R. Pederson, and L. E. Lindgren, "A model for Ti–6Al–4V microstructure evolution for arbitrary temperature changes," *Modelling and Simulation in Materials Science and Engineering,* vol. 20, no. 5, 2012, doi: 10.1088/0965-0393/20/5/055006.

[110] J. Nitzler, C. Meier, K. W. Müller, W. A. Wall, and N. E. Hodge, "A novel physics-based and data-supported microstructure model for part-scale simulation of laser powder bed fusion of Ti-6Al-4V," *Advanced Modeling and Simulation in Engineering Sciences,* vol. 8, no. 1, 2021, doi: 10.1186/s40323-021-00201-9.

[111] X. Lu *et al.*, "Finite element analysis and experimental validation of the thermomechanical behavior in laser solid forming of Ti-6Al-4V," *Additive Manufacturing,* vol. 21, pp. 30-40, 2018, doi: 10.1016/j.addma.2018.02.003.

[112] X. Lu *et al.*, "In situ measurements and thermo-mechanical simulation of Ti–6Al–4V laser solid forming processes," *International Journal of Mechanical Sciences,* vol. 153-154, pp. 119-130, 2019, doi: 10.1016/j.ijmecsci.2019.01.043.

[113] D. Buchbinder, W. Meiners, N. Pirch, K. Wissenbach, and J. Schrage, "Investigation on reducing distortion by preheating during manufacture of aluminum components using selective laser melting," *Journal of Laser Applications,* vol. 26, no. 1, 2014, doi: 10.2351/1.4828755.

[114] Q. Luo and S. Yang, "Uncertainty of the x-ray diffraction (XRD) sin2 ψ technique in measuring residual stresses of physical vapor deposition (PVD) hard coatings," *Coatings,* vol. 7, no. 8, p. 128, 2017.

[115] N. Rossini, M. Dassisti, K. Benyounis, and A.-G. Olabi, "Methods of measuring residual stresses in components," *Materials & Design,* vol. 35, pp. 572-588, 2012.

[116] F. Kandil, J. Lord, A. T. Fry, and P. Grant, "A review of residual stress measurement methods-a guide to technique selection," 2001.

[117] K. Khan, L. S. Mohan, A. De, and T. DebRoy, "Rapid calculation of part scale residual stresses in powder bed additive manufacturing," *Science and Technology of Welding and Joining,* pp. 1-9, 2022.

[118] Q. Wang, J. Shi, L. Zhang, S. Tsutsumi, J. Feng, and N. Ma, "Impacts of laser cladding residual stress and material properties of functionally graded layers on titanium alloy sheet," *Additive Manufacturing,* vol. 35, p. 101303, 2020.

[119] W. Huang, Q. Wang, N. Ma, and H. Kitano, "Distribution characteristics of residual stresses in typical wall and pipe components built by wire arc additive manufacturing," *Journal of Manufacturing Processes,* vol. 82, pp. 434-447, 2022.

[120] Y. Ueda, H. Murakawa, and N. Ma, *Welding deformation and residual stress prevention*. Elsevier, 2012.

[121] D. Wang, Y. Yang, Z. Yi, and X. Su, "Research on the fabricating quality optimization of the overhanging surface in SLM process," *The International Journal of Advanced Manufacturing Technology,* vol. 65, pp. 1471-1484, 2013.

[122] R. Yavari *et al.*, "Part-scale thermal simulation of laser powder bed fusion using graph theory: Effect of thermal history on porosity, microstructure evolution, and recoater crash," *Materials & Design,* vol. 204, p. 109685, 2021.

[123] J.-P. Kruth, G. Levy, F. Klocke, and T. Childs, "Consolidation phenomena in laser and powder-bed based layered manufacturing," *CIRP annals,* vol. 56, no. 2, pp. 730-759, 2007.

[124] E. Yasa, J. Deckers, T. Craeghs, M. Badrossamay, and J.-P. Kruth, "Investigation on occurrence of elevated edges in selective laser melting," in *2009 International Solid Freeform Fabrication Symposium,* 2009: University of Texas at Austin.

[125] S. Feng, S. Chen, A. M. Kamat, R. Zhang, M. Huang, and L. Hu, "Investigation on shape deviation of horizontal interior circular channels fabricated by laser powder bed fusion," *Additive Manufacturing,* vol. 36, p. 101585, 2020.

[126] M. Qu *et al.*, "Controlling process instability for defect lean metal additive manufacturing," *Nature communications,* vol. 13, no. 1, p. 1079, 2022.

[127] S. Feng, A. M. Kamat, S. Sabooni, and Y. Pei, "Experimental and numerical investigation of the origin of surface roughness in laser powder bed fused overhang regions," *Virtual and Physical Prototyping,* vol. 16, no. sup1, pp. S66-S84, 2021.

[128] D. Thomas, "The development of design rules for selective laser melting," Cardiff Metropolitan University, 2009.

[129] A. Paraschiv, G. Matache, N. Constantin, and M. Vladut, "Investigation of Scanning Strategies and Laser Remelting Effects on Top Surface Deformation of Additively Manufactured IN 625," *Materials,* vol. 15, no. 9, p. 3198, 2022.

[130] E. Abele and M. Kniepkamp, "Analysis and optimisation of vertical surface roughness in micro selective laser melting," *Surface Topography: Metrology and Properties,* vol. 3, no. 3, p. 034007, 2015.

[131] H. Chen, D. Gu, J. Xiong, and M. Xia, "Improving additive manufacturing processability of hard-to-process overhanging structure by selective laser melting," *Journal of Materials Processing Technology,* vol. 250, pp. 99-108, 2017.

[132] F. Wu, Z. Sun, W. Chen, and Z. Liang, "The Effects of Overhang Forming Direction on Thermal Behaviors during Additive Manufacturing Ti-6Al-4V Alloy," *Materials,* vol. 14, no. 13, p. 3749, 2021.

[133] Z. Chen, S. Cao, X. Wu, and C. H. Davies, "Surface roughness and fatigue properties of selective laser melted Ti–6Al–4V alloy," in *Additive manufacturing for the aerospace industry*: Elsevier, 2019, pp. 283-299.

[134] Z. Yuan and X. Chen, "Novel approach for fabricating horizontal overhanging structures in selective laser melting," *Journal of Manufacturing Processes,* vol. 85, pp. 793-801, 2023.

[135] H. Yeung, B. Lane, and J. Fox, "Part geometry and conduction-based laser power control for powder bed fusion additive manufacturing," *Additive manufacturing,* vol. 30, p. 100844, 2019.

[136] B. Cheng and K. Chou, "A numerical investigation of support structure designs for overhangs in powder bed electron beam additive manufacturing," *Journal of Manufacturing Processes,* vol. 49, pp. 187-195, 2020.

[137] B. Cheng and K. Chou, "Geometric consideration of support structures in part overhang fabrications by electron beam additive manufacturing," *Computer-Aided Design,* vol. 69, pp. 102-111, 2015.

[138] W. Ameen, A. Al-Ahmari, and M. K. Mohammed, "Self-supporting overhang structures produced by additive manufacturing through electron beam melting," *The International Journal of Advanced Manufacturing Technology,* vol. 104, pp. 2215-2232, 2019.

[139] M. Y. Kayacan, K. Özsoy, B. Duman, N. Yilmaz, and M. C. Kayacan, "A study on elimination of failures resulting from layering and internal stresses in Powder Bed Fusion (PBF) additive manufacturing," *Materials and Manufacturing Processes,* vol. 34, no. 13, pp. 1467-1475, 2019.

[140] T. Liu, E. C. Kinzel, and M. C. Leu, "In-situ lock-in thermographic measurement of powder layer thermal diffusivity and thickness in laser powder bed fusion," *Additive Manufacturing,* vol. 74, p. 103726, 2023.

[141] T. Liu *et al.*, "In-situ infrared thermographic inspection for local powder layer thickness measurement in laser powder bed fusion," *Additive Manufacturing,* vol. 55, p. 102873, 2022.

[142] L. Scime and J. Beuth, "Anomaly detection and classification in a laser powder bed additive manufacturing process using a trained computer vision algorithm," *Additive Manufacturing,* vol. 19, pp. 114-126, 2018.

[143] F. G. Fischer, M. G. Zimmermann, N. Praetzsch, and C. Knaak, "Monitoring of the powder bed quality in metal additive manufacturing using deep transfer learning," *Materials & Design,* vol. 222, p. 111029, 2022.

[144] J. zur Jacobsmühlen, S. Kleszczynski, G. Witt, and D. Merhof, "Detection of elevated regions in surface images from laser beam melting processes," in *IECON 2015-41st Annual Conference of the IEEE Industrial Electronics Society*, 2015: IEEE, pp. 001270-001275.

[145] N. Peter, Z. Pitts, S. Thompson, and A. Saharan, "Benchmarking build simulation software for laser powder bed fusion of metals," *Additive Manufacturing,* vol. 36, p. 101531, 2020.

[146] X. Lu, M. Chiumenti, M. Cervera, M. Slimani, and I. Gonzalez, "Recoater-Induced Distortions and Build Failures in Selective Laser Melting of Thin-Walled Ti6Al4V Parts," *Journal of Manufacturing and Materials Processing*, vol. 7, no. 2, p. 64, 2023.

[147] A. M. Kamat and Y. Pei, "An analytical method to predict and compensate for residual stress-induced deformation in overhanging regions of internal channels fabricated using powder bed fusion," *Additive Manufacturing*, vol. 29, p. 100796, 2019.

[148] M. H. Kobir *et al.*, "Prediction of recoater crash in laser powder bed fusion additive manufacturing using graph theory thermomechanical modeling," *Progress in Additive Manufacturing*, vol. 8, no. 3, pp. 355-380, 2023.

[149] M. H. Kobir, "Thermomechanical Modeling in Laser Powder Bed Fusion Additive Manufacturing using Graph Theory: Application to Prediction of Recoater Crash," M.S., University of Nebraska-Lincoln, 2021.

[150] FARO Technologies Inc. "Quantum Max FaroArm Series." https://www.faro.com/en/Products/Hardware/Quantum-FaroArms (accessed December 11, 2023.

[151] P. Bidare, R. R. J. Maier, R. J. Beck, J. D. Shephard, and A. J. Moore, "An open-architecture metal powder bed fusion system for in-situ process measurements," *Additive Manufacturing*, vol. 16, pp. 177-185, 2017.

[152] Y. Mahmoodkhani *et al.*, "On the measurement of effective powder layer thickness in laser powder-bed fusion additive manufacturing of metals," *Progress in Additive Manufacturing*, vol. 4, pp. 109-116, 2019.

[153] T. M. Wischeropp, C. Emmelmann, M. Brandt, and A. Pateras, "Measurement of actual powder layer height and packing density in a single layer in selective laser melting," *Additive Manufacturing*, vol. 28, pp. 176-183, 2019.

[154] H. Chen, T. Cheng, Z. Li, Q. Wei, and W. Yan, "Is high-speed powder spreading really unfavourable for the part quality of laser powder bed fusion additive manufacturing?," *Acta materialia*, vol. 231, p. 117901, 2022.

[155] S. Soudarissanane, R. Lindenbergh, M. Menenti, and P. Teunissen, "Scanning geometry: Influencing factor on the quality of terrestrial laser scanning points," *ISPRS journal of photogrammetry and remote sensing*, vol. 66, no. 4, pp. 389-399, 2011.

[156] J. Pakkanen *et al.*, "Study of internal channel surface roughnesses manufactured by selective laser melting in aluminum and titanium alloys," *Metallurgical and Materials Transactions A,* vol. 47, pp. 3837-3844, 2016.

[157] K. Kadirgama *et al.*, "Statistical and optimize of lattice structures with selective laser melting (SLM) of Ti6AL4V material," *The International Journal of Advanced Manufacturing Technology,* vol. 97, pp. 495-510, 2018.

[158] C. Hartmann, P. Lechner, B. Himmel, Y. Krieger, T. C. Lueth, and W. Volk, "Compensation for geometrical deviations in additive manufacturing," *Technologies,* vol. 7, no. 4, p. 83, 2019.

[159] S. Afazov *et al.*, "A methodology for precision additive manufacturing through compensation," *Precision Engineering,* vol. 50, pp. 269-274, 2017.

[160] S. Afazov, E. Semerdzhieva, D. Scrimieri, A. Serjouei, B. Kairoshev, and F. Derguti, "An improved distortion compensation approach for additive manufacturing using optically scanned data," *Virtual and Physical Prototyping,* vol. 16, no. 1, pp. 1-13, 2021.

[161] K. Xu, T.-H. Kwok, Z. Zhao, and Y. Chen, "A reverse compensation framework for shape deformation control in additive manufacturing," *Journal of Computing and Information Science in Engineering,* vol. 17, no. 2, p. 021012, 2017.

[162] C. Wang, S. Li, D. Zeng, and X. Zhu, "Quantification and compensation of thermal distortion in additive manufacturing: A computational statistics approach," *Computer Methods in Applied Mechanics and Engineering,* vol. 375, p. 113611, 2021.

[163] Y. Xie, B. Li, C. Wang, K. Zhou, C. Wu, and S. Li, "A Bayesian regularization network approach to thermal distortion control in 3D printing," *Computational Mechanics,* pp. 1-18, 2023.

[164] Y. Xie, S. Li, C. Wu, D. Lyu, C. Wang, and D. Zeng, "A generalized Bayesian regularization network approach on characterization of geometric defects in lattice structures for topology optimization in preliminary design of 3D printing," *Computational Mechanics,* vol. 69, no. 5, pp. 1191-1212, 2022.

[165] S. Afazov, W. A. Denmark, B. L. Toralles, A. Holloway, and A. Yaghi, "Distortion prediction and compensation in selective laser melting," *Additive Manufacturing,* vol. 17, pp. 15-22, 2017.

[166] A. Yaghi, S. Ayvar-Soberanis, S. Moturu, R. Bilkhu, and S. Afazov, "Design against distortion for additive manufacturing," *Additive manufacturing,* vol. 27, pp. 224-235, 2019.

[167] V. Stiuso, P. Minetola, F. Calignano, M. Galati, M. Khandpur, and L. Fontana, "Experimental assessment of compensated distortion in selective laser melting of Ti6Al4V parts," in *IOP Conference Series: Materials Science and Engineering*, 2021, vol. 1136, no. 1: IOP Publishing, p. 012048.

[168] M. Biegler, B. A. Elsner, B. Graf, and M. Rethmeier, "Geometric distortion-compensation via transient numerical simulation for directed energy deposition additive manufacturing," *Science and Technology of Welding and Joining,* vol. 25, no. 6, pp. 468-475, 2020.

[169] Ansys Inc., "Advanced Analysis Guide Chapter 7: Element Birth and Death," *Mechanical APDL 2021 R1* 2021.

[170] Autodesk Inc. "Working with Distortion Compensation." https://help.autodesk.com/view/NETF/2023/ENU/?guid=GUID-E3684262-8AF9-4899-9287-D79A929F6D98 (accessed July 19, 2023.

[171] M. Valizadeh and S. J. Wolff, "Convolutional Neural Network applications in additive manufacturing: A review," *Advances in Industrial and Manufacturing Engineering,* vol. 4, p. 100072, 2022/05/01/ 2022, doi: https://doi.org/10.1016/j.aime.2022.100072.

[172] S. Chowdhury and S. Anand, "Artificial neural network based geometric compensation for thermal deformation in additive manufacturing processes," in *International Manufacturing Science and Engineering Conference*, 2016, vol. 49910: American Society of Mechanical Engineers, p. V003T08A006.

[173] R. Hong *et al.*, "Artificial neural network-based geometry compensation to improve the printing accuracy of selective laser melting fabricated sub-millimetre overhang trusses," *Additive Manufacturing,* vol. 37, p. 101594, 2021.

[174] B. J. Paudel, H. Deng, and A. C. To, "A physics-based data-driven distortion compensation model for sintered binder jet parts considering size effects," *Additive Manufacturing,* vol. 68, 2023, doi: 10.1016/j.addma.2023.103517.

[175] Ansys® optiSLang Release 22.2 Help System, "Methods for Multi-Disciplinary Optimization and Robustness," ANSYS, Inc.

[176] C. K. Williams and C. E. Rasmussen, *Gaussian processes for machine learning* (no. 3). MIT press Cambridge, MA, 2006.

[177] J. Wang, "An intuitive tutorial to Gaussian processes regression," *arXiv preprint arXiv:2009.10862*, 2020.

[178] The MathWorks Inc. "Kernel (Covariance) Function Options." https://www.mathworks.com/help/stats/kernel-covariance-function-options.html (accessed June 22, 2023.

[179] I. T. Jolliffe and J. Cadima, "Principal component analysis: a review and recent developments," *Philos Trans A Math Phys Eng Sci*, vol. 374, no. 2065, p. 20150202, Apr 13 2016, doi: 10.1098/rsta.2015.0202.

[180] A. Maćkiewicz and W. Ratajczak, "Principal components analysis (PCA)," *Computers & Geosciences*, vol. 19, no. 3, pp. 303-342, 1993/03/01/ 1993, doi: https://doi.org/10.1016/0098-3004(93)90090-R.

[181] The MathWorks Inc. "pca principal component analysis of raw data." https://www.mathworks.com/help/stats/pca.html#responsive_offcanvas (accessed June 28, 2023.

[182] X. Liang, D. Hayduke, and A. C. To, "An enhanced layer lumping method for accelerating simulation of metal components produced by laser powder bed fusion," *Additive Manufacturing*, vol. 39, 2021, doi: 10.1016/j.addma.2021.101881.

[183] W. Mitchell, D. Lang, T. Merdes, E. Reutzel, and G. Welsh, "Dimensional accuracy of titanium direct metal laser sintered parts," in *2016 International Solid Freeform Fabrication Symposium*, 2016: University of Texas at Austin.

[184] E. Verna, G. Genta, M. Galetto, and F. Franceschini, "Designing offline inspection strategies for selective laser melting additive manufacturing processes," in *Titolo volume non avvalorato*: Associazione Italiana Tecnologie Manifatturiere, 2019.

[185] W. Dong, X. A. Jimenez, and A. C. To, "Temperature-dependent modified inherent strain method for predicting residual stress and distortion of Ti6Al4V walls manufactured by wire-arc directed energy deposition," *Additive Manufacturing*, vol. 62, 2023, doi: 10.1016/j.addma.2022.103386.

[186] Z. Chen, X. Wu, D. Tomus, and C. H. Davies, "Surface roughness of selective laser melted Ti-6Al-4V alloy components," *Additive Manufacturing*, vol. 21, pp. 91-103, 2018.

[187] The MathWorks Inc. "Two-Way ANOVA." https://www.mathworks.com/help/stats/two-way-anova.html (accessed June 22, 2023.

[188] H. Babaee, P. Perdikaris, C. Chryssostomidis, and G. Karniadakis, "Multi-fidelity modelling of mixed convection based on experimental correlations and numerical simulations," *Journal of Fluid Mechanics*, vol. 809, pp. 895-917, 2016.

[189] X. Meng, H. Babaee, and G. E. Karniadakis, "Multi-fidelity Bayesian neural networks: Algorithms and applications," *Journal of Computational Physics*, vol. 438, p. 110361, 2021.